DIGITAL ACCESS TO SCHOLARSHIP AT HARVARD
DASH.HARVARD.EDU

HARVARD LIBRARY
Office for Scholarly Communication

Large-Scale Mantle Structure Observed Through the Lens of Geodynamical Processes

Permanent link
http://nrs.harvard.edu/urn-3:HUL.InstRepos:40046424

Terms of Use
This article was downloaded from Harvard University's DASH repository, and is made available under the terms and conditions applicable to Other Posted Material, as set forth at http://nrs.harvard.edu/urn-3:HUL.InstRepos:dash.current.terms-of-use#LAA

Share Your Story

The Harvard community has made this article openly available.
Please share how this access benefits you. Submit a story .

Accessibility

Large-scale Mantle Structure Observed Through the Lens of Geodynamical Processes

A DISSERTATION PRESENTED
BY
HARRIET C.P. LAU
TO
THE DEPARTMENT OF EARTH AND PLANETARY SCIENCES

IN PARTIAL FULFILLMENT OF THE REQUIREMENTS
FOR THE DEGREE OF
DOCTOR OF PHILOSOPHY
IN THE SUBJECT OF
EARTH AND PLANETARY SCIENCES

HARVARD UNIVERSITY
CAMBRIDGE, MASSACHUSETTS
APRIL 2017

©2017 – Harriet C.P. Lau
all rights reserved.

Dissertation Advisor: Professor Jerry X. Mitrovica Harriet C.P. Lau

Large-scale Mantle Structure Observed Through the Lens of Geodynamical Processes

Abstract

This thesis aims to further our understanding of mantle dynamics by investigating two fundamental parameters that govern such motion: density and viscosity. The variation of mantle density and viscosity dictates the direction, length-scale and time-scale of flow and thus improving our knowledge of these fields represents an important preoccupation of global geophysics. My contributions to these efforts are partitioned between Chapters 2-4 where attention is turned to the development and application of a technique called "tidal tomography" with the goal of determining deep mantle density structure; and Chapter 5 which applies nonlinear Bayesian inversion techniques to observations related to glacial isostatic adjustment in order to infer the radial viscosity profile of the mantle.

Normal mode treatments of the Earth's body tide response were developed in the 1980s to account for the effects of Earth rotation, ellipticity, anelasticity and resonant excitation within the diurnal band. Recent space-geodetic measurements of the Earth's crustal displacement in response to luni-solar tidal forcings have revealed geographical variations that are indicative of aspherical deep mantle structure, and they thus provide a novel data set for constraining deep mantle elastic and density structure. In light of this, in Chapter 2, we make use of advances in seismic free oscillation literature to develop a new, generalized normal mode theory for the body tidal response within the semi-diurnal and long-period tidal band. Our theory involves a perturbation method that permits an efficient calculation of the impact of aspherical structure on the tidal response. In addition, we introduce a normal mode treatment of anelasticity that is distinct from both earlier work in body tides and the approach adopted in free oscillation seismology. We present several simple numerical applications of the new theory and benchmark these applications against independent finite-volume numerical calculations to confirm the accuracy of the theory.

In Chapter 3 we focus on the treatment of anelasticity in the new theory. To date, the widely adopted approach uses a pseudo-normal mode framework for predicting the impact of anelastic effects on the Earth's body tides. There are two noteworthy differences between the traditional and new theories: (1) the traditional theory only considers perturbations to the eigenmodes of an elastic Earth, whereas the new theory augments this set of modes to include the relaxation modes that arise in anelastic behaviour; and (2) the traditional theory approximates the complex perturbation to the tidal Love number as a scaled version of the complex perturbation to the elastic moduli, whereas the new theory computes the full complex perturbation to each eigenmode. We highlight the above differences using a series of synthetic calculations, and demonstrate that the traditional theory can introduce significant error in predictions of the complex perturbation to the Love numbers, and the related predictions of tidal lag angles, due to anelasticity. For the simplified Earth models we test, the computed lag angles differ by $\sim$ 20 per cent. The assumptions adopted in the traditional theory have important implications for previous studies that use model predictions to correct observables for body tide signals or that analyze observations of body tide deformation to infer mantle anelastic structure. Finally, we also highlight the fundamental difference between apparent attenuation (i.e. attenuation inferred from observations or predicted using the above theories) and intrinsic attenuation (i.e. the material property investigated through experiments), where both are often expressed in terms of lag angles or Q^{-1}. In particular, we demonstrate the potentially significant (factor of two or more) bias introduced in estimates of Q^{-1} and its frequency dependence in studies that have treated Q^{-1} determined from tidal phase lags or measured experimentally as being equal. The observed or theoretically predicted lag angle (or apparent Q^{-1}) differs from the intrinsic, material property due to inertia, self-gravity and effects associated with the energy budget. By accounting for these differences we derive, for a special case, an expression that accurately maps apparent attenuation predicted using the extended normal mode formalism derived in Chapter 2 into intrinsic attenuation. The theory allows for more generalized mappings which may be used to robustly connect observations and predictions of tidal lag angles to results from laboratory experiments of mantle materials.

In Chapter 4, we present a new bound on buoyancy structure within Earth's deep mantle derived by applying a tidal tomographic procedure to a global data set of GPS-based body tide deformations in the semi-diurnal band. Earth's body tide response is uniquely sensitive to the density within two massive regions—beneath Africa and the Pacific—extending $\sim$ 1000 km upward from the base of the mantle, known as Large Low Shear Velocity Provinces (LLSVPs). Their integrated buoyancy remains a source of debate within the geophysical literature. Using a probabilistic approach, we bound excess density within the base and middle section of the LLSVPs to interquartile ranges of (0.61–0.74)% and (0.44–0.64)%, respectively. We conclude that the buoyancy of these structures is dominated by the enrichment of high-density chemical components, likely related to subducted oceanic plates and/or primordial material associated with Earth's formation. Our result has important implications for the stability of these structures and, more broadly, the long-term evolution of the Earth system.

Turning our attention to viscosity in the mantle, in Chapter 5 we perform joint nonlinear inversions of GIA data, including: postglacial decay times in Canada and Scandinavia, the Fennoscandian relaxation spectrum (FRS), late-Holocene differential sea level (DSL) highstands (based on recent compilations of Australian sea level histories), and the rate of change of the degree 2 zonal harmonic of the geopotential, J_2. Our resolving power analyses demonstrate that: (1) the FRS constrains mean upper mantle viscosity to be $\sim 3 \times 10^{20}$ Pa s, (2) postglacial decay time data require the average viscosity in the top $\sim$ 1500 km of the mantle to be 10^{21} Pa s, and (3) the J_2 datum constrains mean lower mantle viscosity to be $\sim 5 \times 10^{21}$ Pa s. To reconcile (2) and (3), viscosity must increase to values of $10^{22} - 10^{23}$ Pa s in the deep mantle. Our analysis highlights the importance of accurately correcting the J_2 observation for modern glacier melting in order to robustly infer deep mantle viscosity. We also perform a large series of forward calculations to investigate the compatibility of the GIA data sets with a viscosity jump within the lower mantle, as suggested by geodynamic and seismic studies, and conclude that the GIA data may accommodate a sharp jump of 1–2 orders of magnitude in viscosity across a boundary placed in a depth range of 1000–1700 km, but these data do not require such a feature. Finally, we find that no 1-D viscosity profile appears capable of simultaneously reconciling the DSL highstand data and suggest that this discord is likely due to laterally heterogeneous mantle viscosity.

Taken together, this thesis attempts to deepen our understanding of the nature of mantle dynamics. The major accomplishments include tightly bounding deep mantle density structure and confirming some previous arguments for the significant increase in viscosity from the shallow upper mantle to the base of the mantle. Chapter 6 discusses future research directions that will further the efforts described herein.

Contents

ABSTRACT iii

ACKNOWLEDGEMENTS x

1 INTRODUCTION 1

2 A NORMAL MODE TREATMENT OF SEMI-DIURNAL BODY TIDES ON AN ASPHERICAL, ROTATING AND ANELASTIC EARTH 5
- 2.1 Introduction 5
- 2.2 General Theory 8
  - 2.2.1 The Tidal Potential 8
  - 2.2.2 Non-Hermitian Operator 9
  - 2.2.3 Duality & Biorthogonality 11
  - 2.2.4 Anelasticity over the Tidal Time-scale 13
  - 2.2.5 Perturbation Theory for an Aspherical Earth 19
  - 2.2.6 Semi-Diurnal or Long-Period Body Tide Response 24
- 2.3 Some Illustrative Case Studies 26
  - 2.3.1 Spherical Earth 26
  - 2.3.2 Aspherical Earth 35
- 2.4 Summary 44

3 ANELASTICITY ACROSS SEISMIC TO TIDAL TIME-SCALES: A SELF-CONSISTENT APPROACH 46
- 3.1 Introduction 46
- 3.2 Theoretical Background 49
  - 3.2.1 Parameterizing Anelasticity 50
  - 3.2.2 An Extended Normal Mode (ENM) Theory 52
  - 3.2.3 Love Numbers 63
  - 3.2.4 The Traditional Normal Mode (TNM) Theory 64
- 3.3 Comparison of Predictions Using the TNM and DS Theories 67
  - 3.3.1 Numerical Predictions 67
  - 3.3.2 Is Intrinsic Q the Same as 'Observed Q'? 70
  - 3.3.3 Inertia 74
  - 3.3.4 Self-Gravity 75
  - 3.3.5 Energy Considerations 76

3.4 Summary 78

4 TIDAL TOMOGRAPHY CONSTRAINS EARTH'S DEEP MANTLE BUOYANCY STRUCTURE 80
4.1 Introduction 80
4.2 Procedure 83
4.3 Results and Discussion 90
4.4 Methodological Details 93
4.4.1 Forward Modeling of Body Tides 93
4.4.2 Data Processing 95
4.4.3 Ocean Tidal Loading 96

5 INFERENCES OF MANTLE VISCOSITY BASED ON ICE AGE DATA SETS: RADIAL STRUCTURE 100
5.1 Introduction 100
5.2 Methodology 104
5.2.1 The Forward Problem 104
5.2.2 The Inverse Problem 107
5.3 Data 110
5.3.1 Fennoscandian Relaxation Spectrum 110
5.3.2 Post-Glacial Decay Times 112
5.3.3 $\dot{J}_2$ 113
5.3.4 Differential Sea-Level Highstands 115
5.4 Results and Discussion 116
5.4.1 Fréchet Kernels 116
5.4.2 Bayesian Inversion for Mantle Viscosity 119
5.5 Summary 137

6 CONCLUSIONS AND FUTURE WORK 141
6.1 Tidal Tomography 142
6.2 The Frequency Dependence of Viscosity 143
6.3 Laterally Heterogeneous Viscosity 144

APPENDIX A MODE EXCITATION BY A TIDAL POTENTIAL 147

APPENDIX B EXTRACTING Q^{-1} FROM $h(\omega)$ 151

REFERENCES 168

To the strong and selfless women in my family,

my mother and grandmothers.

Acknowledgments

My Ph.D. journey, now complete, owes much to the many relationships I have had the deep pleasure to forge over my five wonderful years here in Cambridge, MA. Indeed, without even the briefest of interactions, significant parts of this work would have never materialized.

I begin by thanking my Ph.D. comittee, the make up of which has evolved through this process. I thank Prof. Miaki Ishii for early conversations that guided me through the maze of seismic free oscillation theory. Prof. Rick O'Connell who, for those fortunate enough to have known him, will be remembered for his steadfast scholarship and enduring wisdom; his razor-sharp wit and endless quantity of books on all subjects—a small and tasteful portion of which I have gladly inherited. His influence on my approach to science has indeed left its mark, as has his taste for great music and raw oysters. Each time I leave Prof. Brendan Meade's office, I leave it with renewed energy and an alternative perspective on many scientific issues; benefitting enormously from his rigor, precision and unique nuance when discussing topics across geophysics. Towards the end of my Ph.D. I have had the great joy of Prof. Marine Denolle's presence on my committee. Despite overlapping for only one year, her advice on both scientific and career-related aspects of academic life have been invaluable and deeply appreciated. Finally, with much gratefulness, I thank Prof. David Johnston, who acts as the Graduate Student Council representative on my committee. His expertise lies in a field far from topics contained within this thesis and yet he has shown a remarkable amount of enthusiasm, encouragement and insight in regard to my work. My committee members—who all are leading experts in their respective fields—are great scientific mentors, with accomplishments and ambitions that I aspire to mirror in my own work. Above all, my collective interactions with them have never failed to improve the quality and integrity of my science.

Those of us working in Earth science are aware that it is impossible to work alone. This thesis contains the fingerprints of a small and distinguished team of collaborators to whom I am in great debt. I thank Prof. Jeroen Tromp (Princeton University) for his patience and unwavering support throughout my Ph.D. He has offered not only theoretical insight on many of the derivations outlined in this work but has always been within reach during times of scientific confusion, providing the injection of fresh clarity required to move forward in such moments. Prof. James Davis (Lamont-Doherty Earth Observatory, Columbia University) has taught me the rigor and level of detail required to probe noisy data, with diligence and generosity. He has taken time to show me the sights of the Palisades, NY, while allowing me to share many a meal with his delightful family; Jean, his wife, and Nathan, his remarkably bright and energetic son. Dr Hsin-Ying Yang (Prof. Tromp's post-doctoral researcher, Princeton University) and I developed the mode coupling code utilized in Chapters 2–4 and the whole process, though difficult, was facilitated by her kindness, willingness to explain, and expertise in free oscillation theory. We continue to be good friends even though she now resides in China. The numerical codes developed throughout this process required benchmarking to provide confidence in the accuracy of our results. Dr Konstantin Latychev, who maintains and develops an independent, finite volume code for work within our research group, has worked endlessly to meet this end. I am grateful for his detailed emails received in the early hours of the morning, his trips to Boston away from his family, and the many lengthy adjustments of his codes; all efforts made to ensure the validity of results within this thesis. I have had the opportunity to spend time at the University of Cambridge hosted, generously, by Dr David Al-Attar, a leading theoretical geophysicist, whose invaluable input is evident throughout this thesis. I thank Drs Ulrich Faul (Massachusetts Institute Technology) and Ben Holtzman (Lamont-Doherty Earth Observatory, Columbia University), collaborators who perform rock deformation experiments, for providing me with a much deeper appreciation for the vast range of physical conditions present here on Earth and the painstaking efforts made to reproduce such states in the laboratory. Finally, I thank the late Prof. John Wahr who, through brief but impressionable interactions, demonstrated immense generosity and profound insight in aid of my work. The published version of the work discussed in Chapter 3 is dedicated in his memory.

My time at Harvard was financially supported under the auspices of several sources, including Harvard University, Harvard University Graduate School of Arts and Sciences, and the National Science Foundation. The administering of such funds, and moreover, all aspects of the logistical issues faced by graduate students, could not have been navigated without the diligence of staff in the Department of Earth and Planetary Sciences. I thank Marisa Reily, Sarah Colgan, Maryorie Grande, Noreen Morrissey, Chenoweth Moffatt, Kathleen McClosky, Paul Kelley, and department chair Prof. John Shaw for their unrelenting commitment to meeting the needs of EPS graduate students.

I have had the immense privalege to be part of a research group that continues to produce innovative science of the highest caliber; bringing together the fields of geophysics, modern- and paleoclimate, archeology, paleontology, ice dynamics, geomorphology, geochemistry, planetary science, applied mathematics and statistics; the possibilities of these intersections seem boundless. Never failing to provide support in an environment of fun, I thank these colleagues whom I also call friends: Dr Eric Morrow, Prof. Natalya Gomez, Dr Erik Chan, Dr Carling Hay, Prof. Ken Ferrier, Prof. Jessica Creveling, Dr Konstantin Latychev, Kimee Moore, Evelyn Powell and Sophie Coulson. In particular, I highlight three members: Tamara Pico whose smile and generosity of time have never failed to lift my days; Dr Jacqueline Austermann, in whom I have found a career-long collaborator and life-long friend; and Jocelyn Fuentes, my dear friend of nearly seven years, with whom I have shared the many struggles and joys of figuring life out. We continue to do so, still.

Beyond this research group lies a larger Earth science community and I thank Sunny Park, Simon Lock, Rita Parai, Kristian Bergen, Athena Eyster, Ophelia Crawford, Jennifer Middleton, Rachel

Silvern, and Taylor Jones for continued support and friendship. My office has been a source of fun at all hours of the day (and, on the occasion, night) and so my thanks turn to Meredith Langstaff, Phoebe DeVries, Ben Thompson, Blake Hodgin, Camille Dwyer, Tim Clements, Judy Pu and Jiuxun Yin. Within this community, I deeply thank Alex Turner—the brother I never had—with whom I have shared in close camaraderie the lows and highs of the past few years; and everything in between. The EPS family as a whole is a marvelous community and to play a part in its mission in both deepening our understanding of the Earth system and sharing such knowledge through its educational goals has been a complete honor and privilege.

I thank my dear friends beyond the Harvard community for widening my experiences and reminding me of the great joys in life: Nick, Herb, Kit, Kim, Colin, Naai, JP, Steve, Andrew, Carolyn, Autumn, and Lynette. I will forever be grateful for the unwavering love and support from my family back home: my father, who is responsible for seeding my passion for science, my mother, my three talented sisters: Jessica, Charlotte and Emma and my recent brother-in-law, Tom; as well as my family here in the states: my uncle, my aunt, my cousins Lawrence, Judy, Georgina and Mario, and my four delightful nephews: Ethan, Noah, Daniel and Joshua; all born after I embarked on my Ph.D.

Above all, I consider myself more than blessed to have been advised by Prof. Jerry Mitrovica. His scientific creativity coupled with his faith in my ability has, on many occasions, saved projects from the brink of my own self-perceived disaster. His generosity extends beyond the realm of academic expectations placed upon him as my Ph.D. advisor demonstrating nothing but unfailing commitment to my development as a researcher, my career and also my personal well-being; doing all this with great humility and a unique sense of humor. Jerry's commitment to my mentorship has and continues to evolve, but never has it waned. In him I have found a life-long mentor and friend.

1

Introduction

The Strange Loop phenomenon occurs whenever, by moving upwards (or downwards) through levels of some hierarchial system, we unexpectedly find ourselves right back where we started.
–D. Hofstadter

The integral role of the mantle in the Earth's complex evolutionary history is unquestioned: the circulation of solid rock that comprises the mantle sets the tempo that governs the motion of the plates on which we stand. The recycling of these plates not only produces quasi-periodic cycles in which continents amalgamate and disaggregate (see, e.g., Burke, 2011, known as Wilson cycles), it controls the storage and release of volatiles that make up our atmosphere and oceans (e.g., Kump et al., 2001). Large upwellings rising through the mantle as part of this circulation are capable of dramatically changing the state of Earth's rotation and, in turn, the climatic conditions on the surface (e.g., Kirschvink et al., 1997); and furthermore, upon reaching the base of a plate, they are capable of producing copious amounts of volcanism linked with great exctinction events throughout Earth's history (e.g., Ganino & Arndt, 2009). In more recent times, mantle flow in response to the cyclic growth and retreat of the great Pleistocene ice sheets produces distinct geographical patterns in the change of sea level as water is exchanged in and out of Earth's ocean basins (e.g. Lambeck & Chappell, 2001).

In order to characterize this convective flow, two parameters are required: the density and the viscosity fields of the mantle. These fields, together, dictate the direction, time-scale and length-scale of mantle flow; and because of this importance, the level of uncertainty associated with these parameters must be significantly improved to make accurate statements concerning any of the processes highlighted in the opening paragraph. The ultimate motivation behind this thesis is to better characterize both the large-scale density and viscosity structure of the mantle.

Chapters 2-4 of this thesis are concerned with the first of these parameters—mantle density—via the development of an entirely new technique called "tidal tomography". Body tides, a classic but much-neglected field of geophysics, offer a novel avenue to address the question of mantle density. The story of deep mantle density is one of much debate and ambiguity, that reaches back to as early as the 1970s where evidence of compositionally distinct reservoirs preserved over age-of-Earth time-scales called for stable regions in the mantle undisturbed by the convective vigor of mantle circulation (Hofmann, 1997). Geodynamical evidence derived from data sets associated with mantle convection, however, imply a very different picture of mantle dynamics: one of high Rayleigh number flow and thermally buoyant upwellings (consistent with long-wavelength geoid highs above Africa and the Pacific (Hager et al., 1985); core-mantle boundary excess ellipticity (Forte & Mitrovica, 2001); and the long-term uplift of the African continent driven by dynamic topography (Gurnis et al., 2000)).

Our understanding of the spatial distribution of mantle heterogeneity owes much to the field of seismic tomography, providing the community with ever-improving images of the variations in seismic wave speed within the Earth's interior (e.g., Su & Dziewonski, 1997; Masters et al., 2000;

Ritsema et al., 2011). However, the interpretation of such images and how to extract the density field from wave speed variations remains a highly non-unique exercise, particularly in the deep mantle (Karato & Karki, 2001). As such, placing these images in the context of the conflicting views of mantle convection from arguments based on geochemistry and geodynamics faces a fundamental complication. In contrast, our implementation of tidal tomography couples knowledge provided by seismic tomography to produce an image of density variations in the deep mantle, the result of an inversion of GPS measurements of crustal displacement associated with the Earth's semi-diurnal body tide.

In order to implement such a methodology, we first derive a forward theory which involves significant extensions to the theoretical treatment of body tides developed by John Wahr and colleagues in the 1980s. In Chapter 2 we outline a theory to predict semi-diurnal body tides on an aspherical, rotating and anelastic Earth based on a normal mode methodology originally developed to predict the Earth's long-period response to an earthquake. During the development of this theory, it became clear that the treatment of anelasticity in the established body tide theory made several assumptions that not only affect the accuracy of body tide predictions but also the interpretation of body tide observations. The latter has implications for inferences on the frequency dependence of dissipation in the mantle. In Chapter 3 we focus on this aspect of the theory.

In Chapter 4 we apply the theory derived in Chapter 2 to a global GPS data set (Yuan et al., 2013) which comprises measurements of crustal displacement associated with the so-called 'M2' body tide (a lunar, semi-diurnal body tide). We take a probabilistic inversion approach where we test a large suite of models against their fit to the GPS data, resulting in a tight constraint on deep mantle buoyancy structure. We find regions of excess density at the base of the mantle beneath Africa and the Pacific and surrounding regions at this depth to be of small and positive buoyancy (or negative excess density). Our results are consistent with these regions of excess density representing compositionally distinct parts of the mantle enriched in relatively dense elements (e.g., iron). And thus Chapters 2-4 are a culmination of our efforts to address the issue of deep mantle buoyancy.

In Chapter 5 we turn our attention to the steady-state viscosity structure of the mantle by exploring the deformation of the solid Earth in response to the retreat of ice sheets, a process known as glacial isostatic adjustment (or 'GIA'). During the peak of the last ice age ($\sim$ 21,000 years ago, a time known as the Last Glacial Maximum or 'LGM'; Clark et al., 2009) large ice sheets extended across the North American and Eurasian continents. As Earth moved from this glacial phase to its present state, the melting of these great ice sheets have left distinct sea-level markers that record the Earth's deformation over this timespan. These sea-level records have been used to make estimates of the mantle viscosity structure (e.g., Nakada & Lambeck, 1989; Peltier, 2004; Mitrovica & Forte, 2004; Kaufmann & Lambeck, 2002) but, like the density field of the mantle, there has been much debate as to the accuracy and uniqueness of these inferences over the past few decades. Much of the debate is centered on whether the mantle is isoviscous (or nearly isoviscous, involving a nominal increase in viscosity with depth) (e.g., Cathles, 1975; Peltier, 1976, 2004); or characterized by an increase in viscosity by a factor of 10–100 with depth (e.g., O'Connell, 1971; Richards & Hager, 1984; Nakada & Lambeck, 1989; Mitrovica & Forte, 2004). We revisit this classical problem by applying updated sea-level records and long-wavelength gravity data associated with the GIA process to a nonlinear Bayesian inversion, and rigorously consider the information content of each datum.

Finally, in Chapter 6, we conclude our findings and synthesize the results concerning the density and viscosity structure of the mantle. Looking beyond this thesis, we consider the next steps to further our understanding of mantle dynamics.

2

A Normal Mode Treatment of Semi-Diurnal Body Tides on an Aspherical, Rotating and Anelastic Earth

> *Moon, Turn the Tides... Gently Gently Away*
> –J. Hendrix

2.1 INTRODUCTION

Predicting deformation of the solid Earth in response to periodic luni-solar forcings, the so-called body tides, has a rich history in classical geophysics. Early theoretical studies considered the response

---

A version of this chapter was published with Hsin-Ying Yang, Jeroen Tromp, Jerry X. Mitrovica, Konstantin Latychev, and David Al-Attar in *Geophysical Journal International*, vol. 202, p. 1392-1406, 2015.

of a homogeneous, incompressible, elastic sphere (Thomson, 1863), and also derived a set of dimensionless numbers, the so-called Love and/or Shida numbers, that map the tidal forcing into radial and horizontal crustal displacements and perturbations in the geopotential (Love, 1911; Shida, 1912). Later studies in the second half of the 20th century incorporated spherically-symmetric elastic and density structure, including an inviscid core, into the theoretical and numerical treatment of Love numbers (Takeuchi, 1950; Alterman et al., 1959; Farrell, 1972) and also accounted for the effects of rotation and ellipticity (Wahr, 1981a,b), anelasticity and resonances in the diurnal band associated with the free-core nutation (Wahr & Bergen, 1986), and excess-ellipticity (Dehant et al., 1999). Most recently, finite element/volume numerical schemes have been described that compute the body tide response of Earth models with 3-D variations in elastic and density structure (Métivier & Conrad, 2008; Latychev et al., 2009).

Initially, body tide research was largely dedicated to making predictions with sufficient accuracy that their effect on observations of Earth's solid surface and gravitational field could be removed, thus isolating other signals for investigation. Indeed, corrections of this kind are now routinely incorporated into most GPS analysis standards (e.g., Petit & Luzum, 2010). To this end, the series of canonical papers by Wahr and colleagues (Wahr, 1981a,b; Wahr & Bergen, 1986) directly linked the Earth's body tides to an eigenfunction expansion developed within normal mode (or free oscillation) seismology. In this paper, we revisit the normal mode treatment of the tidal problem for three reasons: (i) to update the theory by taking advantage of important advances in free oscillation theory, namely a perturbation approach for incorporating aspherical (i.e., 3-D or laterally heterogeneous) Earth structure; (ii) to include a rigorous method for dealing with the non-Hermitian operator that arises when considering rotating and anelastic Earth models (Lognonné, 1991); and (iii) to introduce a treatment of anelasticity that is more general than the approach introduced in previous work (Wahr & Bergen, 1986).

Our effort is motivated by progressive improvements in the accuracy of space-geodetic measurements, which has now reached a level where these additional complexities have become relevant to the analysis of the body tide response (e.g., Mitrovica et al., 1994; Herring & Dong, 1994; Yuan & Chao, 2012; Krásná et al., 2013). Moreover, such improvements provide a novel means to investigate the internal structure of the Earth. Of particular relevance in this regard are the three recent studies of Ito & Simons (2011), Yuan et al. (2013) and Qin et al. (2014). Ito & Simons (2011) used regional variability in the ocean tidal loading displacement across the western USA, as measured by GPS using the Plate Boundary Observatory network, to estimate subsurface elastic and density structure. Furthermore, motivated by the GRAIL satellite gravity mission, Qin et al. (2014) derived a normal mode perturbation theory to predict the impact of laterally heterogeneous elastic structure on lunar body tides and (ultimately) to infer long-wavelength internal structure of the Moon, which is thought to be dominated by nearside-farside heterogeneity. Finally, Yuan et al. (2013) used a global GPS network to estimate geographical variations of the Earth's semi-diurnal and diurnal body tide displacements with sub-mm precision. These variations are likely indicative of aspherical Earth structure.

Our aim here is to derive a complete theory for predicting semi-diurnal body tides on an aspherical, rotating and anelastic Earth, and to describe a practical framework for accurately implementing the theory. The theory can accommodate long-period tides but it does not extend to the prediction of the Chandler Wobble, a free oscillation with a period of 435 days (Smith & Dahlen, 1981), or to diurnal body tides, which are impacted by resonant forcing associated with processes in the core and at the core-mantle boundary. The ultimate goal of our analysis is to provide a theoretical framework for using observations of the semi-diurnal and long-period body tide response — whether they are based on satellite-geodetic measurements or long-period seismic recordings — in a tomographic inversion procedure to constrain long-wavelength elastic, anelastic and/or density structure. Since the normal mode formalism we apply is semi-analytic, solving the forward problem is computationally inexpensive. This represents a significant advantage over numerical, finite-element approaches for predicting the body tide response (Métivier & Conrad, 2008; Latychev et al., 2009).

We begin by briefly describing the harmonic representation of the luni-solar tidal forcing. We then describe our generalized normal mode treatment of the body tide response with emphasis on our adoption of advances in free-oscillation seismology that post-date studies in the 1980s and our treatment of anelastic effects through the inclusion of relaxation modes. Next, we present some simple calculations for the case of a spherically-symmetric, elastic Earth and compare these to results based on the traditional Love number theory (Farrell, 1972); a comparison that highlights the link between the tidal problem and the long-period seismology problem. We then extend this test to calculate the frequency dependence of the Love numbers in the case of an anelastic Earth model. We also present body tide predictions for an Earth with aspherical mantle structure, and compare these with calculations based on a finite volume simulation (Latychev et al., 2009). Finally, we explore the effects of rotation on the body tide response.

2.2 GENERAL THEORY

2.2.1 THE TIDAL POTENTIAL

The tidal potential for an observer whose origin is at the center of mass of the Earth, $\Psi(\mathbf{r};t)$, can be expressed using the following harmonic representation (Cartwright & Edden, 1973; Agnew, 2007):

$$\Psi(\mathbf{r};t) = \sum_{\ell=2}^{\infty} \sum_{m=-\ell}^{\ell} \left(\frac{r}{a}\right)^{\ell} c_{\ell m}(t) Y_{\ell m}(\theta,\lambda) \ , \tag{2.1}$$

where $Y_{\ell m}(\theta,\lambda)$ is the fully-normalized spherical harmonic of degree ℓ and order m (Edmonds, 1960), and t is time. The position vector $\mathbf{r}$ is specified by a radius $r = |\mathbf{r}|$, colatitude θ, and longitude λ. The Earth's radius is denoted by a. The amplitude of the tidal potential decreases by a factor of $\approx 1/60$ with each increasing degree ℓ and so summation is often truncated at $\ell = 4$ or lower.

The coefficients $c_{\ell m}$ are represented as the sum of complex exponentials of various (real) frequencies and phases, as specified in tidal tables (Cartwright & Edden, 1973):

$$c_{\ell m}(t) = \sum_j \mathcal{C}^j_{\ell m} \exp[i(\omega_j t + \eta_j)] \ , \tag{2.2}$$

where $\mathcal{C}^j$, ω_j and η_j are the amplitude, frequency and phase of the j-th harmonic, respectively. We can furthermore consider the tidal potential $\Psi(\mathbf{r}; t)$ in the frequency domain, which we write as $\tilde{\Psi}(\mathbf{r}; \omega)$ (and equivalently for $c_{\ell m}(t)$, $\tilde{c}_{\ell m}(\omega)$).

The most significant tides are the 'degree-2' tides, which naturally partition into three temporal bands: the semi-diurnal or sectorial band ($[\ell, m] = [2, \pm 2]$), the diurnal or tesseral band ($[\ell, m] = [2, \pm 1]$) and the long-period or zonal band ($[\ell, m] = [2, 0]$). The first descriptor in each case specifies the time dependence while the second refers to the spatial geometry of the forcing. The diurnal response is also impacted by resonant excitation due to the free-core nutation/nearly-diurnal free wobble and involves additional rotational modes (Wahr & Bergen, 1986). In the following discussion we avoid this complexity and focus on the semi-diurnal and long-period body tide response.

2.2.2 Non-Hermitian Operator

Over the last few decades, advances in seismology have yielded a perturbation theory that allows for the prediction of the long-period response on an aspherical, anelastic, rotating Earth due to earthquake sources (see Dahlen & Tromp, 1998, for a review). Important contributions have been made by, e.g., Dahlen (1968), Gilbert (1970), Woodhouse & Dahlen (1978), Woodhouse (1980), Park & Gilbert (1986) and Lognonné (1991); and more recently, Deuss & Woodhouse (2001) and Deuss & Woodhouse (2004). The derivation outlined below makes full use of the present state of this theory, though we highlight the unique issues that arise in considering the response to a tidal potential forcing. The frequency domain governing equation of motion for a rotating, anelastic Earth due to a tidal forcing is

$$\mathcal{H}(\mathbf{r};\nu)\mathbf{s}(\mathbf{r}) - \nu^2\,\mathbf{s}(\mathbf{r}) + 2i\nu\,\mathbf{\Omega}\times\mathbf{s}(\mathbf{r}) = -\nabla\tilde{\Psi}(\mathbf{r};\nu), \qquad \mathbf{r}\in V\ , \tag{2.3}$$

where V denotes the Earth's volume, $\mathbf{s}$ the displacement, ν the complex frequency, $\mathbf{\Omega}$ the angular rotation vector, and $i=\sqrt{-1}$. In practice, ν is dominated by the (real) forcing frequency, ω_T. The operator $\mathcal{H}$ is defined by

$$\rho(\mathbf{r})\,\mathcal{H}(\mathbf{r};\nu)\mathbf{s}(\mathbf{r}) = \rho(\mathbf{r})\,\nabla\phi(\mathbf{r}) + \rho(\mathbf{r})\,\mathbf{s}(\mathbf{r})\cdot\nabla\nabla(\Phi(\mathbf{r})+\psi(\mathbf{r})) - \nabla\cdot[\mathbf{\Lambda}(\mathbf{r};\nu):\nabla\mathbf{s}(\mathbf{r})]\ , \tag{2.4}$$

where ρ is the mass density, and the equilibrium gravitational potential, centrifugal potential and incremental gravitational potential, Φ, ψ and ϕ, respectively, are given by

$$\Phi(\mathbf{r}) = -G\int_V \frac{\rho(\mathbf{r}')}{||\mathbf{r}-\mathbf{r}'||}\,\mathrm{d}V'\ , \tag{2.5}$$

$$\psi(\mathbf{r}) = -\frac{1}{2}\left[\Omega^2 r^2 - (\mathbf{\Omega}\cdot\mathbf{r})^2\right]\ , \tag{2.6}$$

$$\phi(\mathbf{r}) = -G\int_V \frac{\rho(\mathbf{r}')\,\mathbf{s}(\mathbf{r}')\cdot(\mathbf{r}-\mathbf{r}')}{||\mathbf{r}-\mathbf{r}'||^3}\,\mathrm{d}V'\ . \tag{2.7}$$

In these expressions G is the universal gravitational constant and $\mathbf{\Lambda}$ is a fourth-order elastic tensor that defines the first Piola-Kirchhoff stress tensor. Eq. (2.3) is solved along with the following boundary condition:

$$\hat{\mathbf{n}}(\mathbf{r})\cdot[\mathbf{\Lambda}(\mathbf{r};\nu):\nabla\mathbf{s}(\mathbf{r})] = \mathbf{0}\ ,\ \ \mathbf{r}\in\partial V\ , \tag{2.8}$$

where ∂V is the surface of the Earth with unit outward normal $\hat{\mathbf{n}}$.

We note two important characteristics of this boundary value problem: the first is its nonlinearity in the eigenvalue parameter as a result of the frequency-dependence of $\mathcal{H}$ and the second is its non-Hermitian nature due to the complex parameterization of $\mathbf{\Lambda}$. These characteristics reflect the presence of dispersion and attenuation, both of which are a consequence of considering an anelastic Earth. $\boldsymbol{\Lambda}$ must satisfy the relation $\boldsymbol{\Lambda}^*(\nu) = \boldsymbol{\Lambda}(-\nu^*)$ (where the asterisk denotes complex conjugation) and must be analytic in the upper half of the complex ν plane to ensure reality and causality of the time-domain response (Nowick & Berry, 1972). Our treatment of $\boldsymbol{\Lambda}$ will be different from the commonly adopted approach in seismology, as will be discussed in Section 2.2.4.

Eqs (2.3) and (2.8) describe the forced motion of a conservative physical system, and in such systems the solution may be represented as a sum of the normal modes of the system (Gilbert, 1970). Lognonné (1991) derived a theory to deal with the non-Hermitian nature of the boundary value problem in the seismic case. We apply his results next.

2.2.3 DUALITY & BIORTHOGONALITY

Lognonné (1991) considered the eigenmodes of an Earth with the reversed sense of rotation, the so-called anti-Earth. In particular, he defined a dual space of adjoint eigenfunctions using a biorthogonality product. While this is the approach we will proceed with, other methodologies have been developed, e.g., methods based on residue theory (Deuss & Woodhouse, 2004). Following the notation in Section 6.3 of Dahlen & Tromp (1998), if $\mathbf{s}_k$ are the eigenmodes for a rotating Earth and $\overline{\mathbf{s}}_k$ are the eigenmodes for an Earth rotating in the reversed sense, then there are two eigenvalue problems to be solved:

$$\mathcal{H}(\nu_k)\mathbf{s}_k + 2i\nu_k\boldsymbol{\Omega} \times \mathbf{s}_k - \nu_k^2\mathbf{s}_k = \mathbf{0} \ , \tag{2.9}$$

$$\mathcal{H}(\nu_k)\overline{\mathbf{s}}_k - 2i\nu_k\boldsymbol{\Omega} \times \overline{\mathbf{s}}_k - \nu_k^2\overline{\mathbf{s}}_k = \mathbf{0} \ . \tag{2.10}$$

Note, we have dropped the dependency on $\mathbf{r}$ from the relevant variables to avoid notational clutter. Lognonné (1991) showed that the eigenfrequency spectrum ν_k is the same regardless of the sense of rotation, though the eigenfunctions $\mathbf{s}_k$ and $\overline{\mathbf{s}}_k$ are different (with each mode k associated with a non-degenerate ν_k due to the presence of rotation). Let us define the duality product by

$$[\overline{\mathbf{s}}_k, \mathbf{s}_{k'}] = \int_V \rho\, \overline{\mathbf{s}}_k \cdot \mathbf{s}_{k'} \mathrm{d}V \ . \tag{2.11}$$

Using this duality product, the operator $\mathcal{H}$ is symmetric with respect to the following operations:

$$[\overline{\mathbf{s}}_k, \mathcal{H}(\nu_k)\mathbf{s}_{k'}] = [\mathcal{H}(\nu_k)\overline{\mathbf{s}}_k, \mathbf{s}_{k'}] = [\mathbf{s}_{k'}, \mathcal{H}(\nu_k)\overline{\mathbf{s}}_k] \ , \tag{2.12}$$

while the Coriolis operator is anti-symmetric:

$$[\overline{\mathbf{s}}_k, i\mathbf{\Omega} \times \mathbf{s}_{k'}] = \ - [i\mathbf{\Omega} \times \overline{\mathbf{s}}_k, \mathbf{s}_{k'}] = \ - [\mathbf{s}_{k'}, i\mathbf{\Omega} \times \overline{\mathbf{s}}_k] \ . \tag{2.13}$$

The anti-symmetry of the Coriolis operator is dealt with by introducing the anti-Earth, with rotation vector $-\mathbf{\Omega}$. Taking the duality product of $\mathcal{H}(\nu_k)\overline{\mathbf{s}}_k - 2i\nu_k\mathbf{\Omega} \times \overline{\mathbf{s}}_k = \nu_k^2\overline{\mathbf{s}}_k$ with $\mathbf{s}_{k'}$ yields

$$\nu_k^2[\mathbf{s}_{k'}, \overline{\mathbf{s}}_k] + 2\nu_k[\mathbf{s}_{k'}, i\mathbf{\Omega} \times \overline{\mathbf{s}}_k] - [\mathbf{s}_{k'}, \mathcal{H}(\nu_k)\overline{\mathbf{s}}_k] = 0 \ , \tag{2.14}$$

and the duality product of $\mathcal{H}(\nu_{k'})\mathbf{s}_{k'} - 2i\nu_{k'}\mathbf{\Omega} \times \mathbf{s}_{k'} = \nu_{k'}^2\mathbf{s}_{k'}$ with $\overline{\mathbf{s}}_k$ gives

$$\nu_{k'}^2[\overline{\mathbf{s}}_k, \mathbf{s}_{k'}] - 2\nu_{k'}[\overline{\mathbf{s}}_k, i\mathbf{\Omega} \times \mathbf{s}_{k'}] - [\overline{\mathbf{s}}_k, \mathcal{H}(\nu_{k'})\mathbf{s}_{k'}] = 0 \ . \tag{2.15}$$

Subtracting eq. (2.15) from (2.14) and dividing by $(\nu_k^2 - \nu_{k'}^2)$ provides the following biorthogonal relation between eigenmodes $\mathbf{s}_{k'}$ and $\overline{\mathbf{s}}_k$:

$$[\overline{\mathbf{s}}_k, \mathbf{s}_{k'}] - \frac{2}{\nu_k + \nu_{k'}}[\overline{\mathbf{s}}_k, i\mathbf{\Omega} \times \mathbf{s}_{k'}] - \frac{[\overline{\mathbf{s}}_k, \{\mathcal{H}(\nu_k) - \mathcal{H}(\nu_{k'})\}\mathbf{s}_{k'}]}{\nu_k^2 - \nu_{k'}^2} = 0 \ , \tag{2.16}$$

where $\nu_k \neq \nu_k$, along with the following normalization for the case $\nu_{k'} = \nu_k$:

$$[\overline{\mathbf{s}}_k, \mathbf{s}_k] - \frac{1}{\nu_k}[\overline{\mathbf{s}}_k, i\mathbf{\Omega} \times \mathbf{s}_k] - \frac{1}{2\nu_k}[\overline{\mathbf{s}}_k, \partial_\nu \mathcal{H}(\nu_k)\mathbf{s}_k] = 1 \ . \tag{2.17}$$

2.2.4 Anelasticity over the Tidal Time-scale

Anelasticity causes both dispersion and attenuation of the response, and manifests itself differently in body tides and the response to earthquakes. In particular, attenuation gives rise to decaying sinusoids for the earthquake response and to a phase lag in the tidal response. Wahr & Bergen (1986) were the first to perform theoretical studies of the body tide on an anelastic Earth and concluded that anelastic effects perturbed the response at the percent level relative to the elastic case. Their approach, however, did not describe precisely how attenuation affects each mode. As we demonstrate in this section, such a description is possible within the theoretical framework outlined in Sections 2.2.2 and 2.2.3. Nevertheless, in deriving our approach we will highlight significant differences in our treatment of anelasticity for the tidal application relative to the approach commonly adopted in the seismic free oscillation literature.

The effect of anelasticity is captured within the term $\mathbf{\Lambda}(\nu)$, where for an isotropic medium

$$\begin{aligned}\Lambda_{ijkl}(\nu) =& [\kappa(\nu) - \tfrac{2}{3}\mu(\nu)]\delta_{ij}\delta_{kl} + \mu(\nu)[\delta_{ik}\delta_{jl} + \delta_{il}\delta_{jk}] + \\ & \tfrac{1}{2}(T^0_{ij}\delta_{kl} + T^0_{kl}\delta_{ij} + T^0_{ik}\delta_{jl} - T^0_{jk}\delta_{il} - T^0_{il}\delta_{jk} - T^0_{jl}\delta_{jk} - T^0_{jl}\delta_{ik}) \ . \end{aligned} \tag{2.18}$$

Here, μ is the shear modulus, κ is the bulk modulus and δ_{ij} is the Kronecker delta. $\mathbf{T}^0$ is the initial stress tensor. The moduli μ and κ are in general spatially-variable, though to avoid clutter we do not explicitly write this dependence. Three aspects related to the form of $\mathbf{\Lambda}(\nu)$ must be considered in solving for the tidal response. These are: anelastic (i) eigenfrequencies and (ii) eigenfunctions; and (iii) the presence of normal modes beyond the usual set considered in seismic applications. Across seismic time-scales $\mathbf{\Lambda}(\nu)$ is commonly built through a superposition of standard linear solids (or Zener solids) (Liu et al., 1976). The superposition is often dictated by measurements of Q_k, the quality-factor of a mode k, across the seismic frequency range. This parameter is related to, but not to be confused with, the intrinsic Q of an anelastic solid, defined formally by O'Connell & Budiansky (1978) as

$$Q_M(\omega) = \frac{\text{Re}\{M(\omega)\}}{\text{Im}\{M(\omega)\}} \ , \tag{2.19}$$

where M may be substituted for μ or κ, and ω is a real frequency. Examples of $\mathbf{\Lambda}(\nu)$ include the constant-Q absorption band model (Kanamori & Anderson, 1977), which is most widely-used in seismology, and the frequency-dependent Q model (Anderson & Minster, 1979). It has been shown, both experimentally (e.g., Jackson et al., 2002) and observationally (e.g., Benjamin et al., 2006; Lekić et al., 2009), that Q is frequency-dependent within and beyond the seismic band, and this is commonly described by a power-law dependency with frequency.

Expressions for the anelastic eigenfrequencies may be derived via a complex, first-order perturbation to the elastic eigenfrequency, ω_k^e, such that

$$\nu_k = \omega_k^e + \delta\omega_k + i\gamma_k \ , \tag{2.20}$$

where $\delta\omega_k$ and γ_k are real, and we define $\omega_k \equiv \text{Re}\{\nu_k\} = \omega_k^e + \delta\omega_k$. The dispersive perturbation, $\delta\omega_k$, is found by considering the real part of $\mu(\nu)$ and $\kappa(\nu)$ perturbed from some reference value:

$$\mu(\nu) \rightarrow \mu_R + \delta\mu(\nu) \ , \tag{2.21}$$

$$\kappa(\nu) \rightarrow \kappa_R + \delta\kappa(\nu) \ . \tag{2.22}$$

The attenuative perturbation, γ_k (the inverse decay time of a mode), is related to Q_k^{-1} by

$$Q_k^{-1} = \frac{2\gamma_k}{\omega_k} \tag{2.23}$$

and is dependent upon how that particular mode samples the Q_μ and Q_κ structure of the Earth. Q_k may be determined by taking the imaginary component of eq. (2.14) with eigenfunctions $\mathbf{s}_k$ and $\mathbf{s}_k^*$, along with the symmetry relation $\mathbf{\Lambda}_{ijkl} = \mathbf{\Lambda}_{klij}$, to yield the relation

$$\begin{aligned} 2\,\mathrm{Re}\{\nu_k\}\mathrm{Im}\{\nu_k\}\left(\int_V \rho\,\mathbf{s}_k^* \cdot \mathbf{s}_k \mathrm{d}V - \omega_k^{-1}\int_V \rho\,\mathbf{s}_k^* \cdot (i\mathbf{\Omega} \times \mathbf{s}_k)\mathrm{d}V\right) = \\ \int_V \nabla\mathbf{s}_k^* : \mathrm{Im}\{\mathbf{\Lambda}(\nu_k)\} : \nabla\mathbf{s}_k\,\mathrm{d}V\ ; \end{aligned} \tag{2.24}$$

and using eq. (2.23) one finds

$$Q_k^{-1} = \frac{\int_V \kappa(\omega_k)Q_\kappa^{-1}(\omega_k)(\nabla\cdot\mathbf{s}_k^*)(\nabla\cdot\mathbf{s}_k) + 2\mu(\omega_k)Q_\mu^{-1}(\omega_k)(\mathbf{d}_k^* : \mathbf{d}_k)\,\mathrm{d}V}{\omega_k^2\left[\int_V \rho\,\mathbf{s}_k^*\cdot\mathbf{s}_k\,\mathrm{d}V - \omega_k^{-1}\int_V \rho\,\mathbf{s}_k^*\cdot(i\mathbf{\Omega}\times\mathbf{s}_k)\mathrm{d}V\right]}\ . \tag{2.25}$$

Here, we have made no assumption about the form that the superposition of standard linear solids may take. Furthermore, Q_μ and Q_κ may or may not be frequency dependent. Over tidal time-scales it is reasonable to expect that Q would be frequency dependent.

In seismic applications for spherically-symmetric Earth models, the treatment of anelasticity would end with the expressions above for anelastic eigenfrequencies. However, anelastic Earth models will also be characterized by complex eigenfunctions. These may be similarly determined by a complex perturbation to the elastic eigenfunctions, thereby introducing a phase shift. The impact of complex eigenfunctions is thought to be negligible in the seismic normal mode problem (Tromp & Dahlen, 1990). However, since lower frequency processes are affected to a greater extent by anelasticity, this may not be the case in the tidal application.

Tromp & Dahlen (1990) derived a free oscillation treatment that precisely accounts for anelasticity on a non-rotating Earth by coupling the modes of an elastic, non-rotating Earth, $\mathbf{s}_k^e$, with associated eigenfrequencies, ω_k^e. We follow a similar procedure, though we will extend their approach to incorporate rotation. Let us expand the anelastic modes of the Earth, $\mathbf{s}_k$, as follows

$$\mathbf{s}_k = \sum_{k'} \chi_{kk'} \mathbf{s}_{k'}^e \ , \tag{2.26}$$

where $\chi_{kk'}$ is complex. Using this expression in eq. (2.9) and taking the inner product with $\mathbf{s}_k^{e*}$ leaves

$$[\omega^2 + \mathbf{V}(\nu) + 2\nu\mathbf{W} - \nu^2]\chi = \mathbf{0} \ , \tag{2.27}$$

where $\omega^2 \ = \ \mathrm{diag}\,\{[\omega_k^e]^2\}$ and $\nu^2 \ = \ \mathrm{diag}\,\{\nu_k^2\}$. Modes on a non-rotating and elastic Earth are normalized according to

$$\int_V \rho\, \mathbf{s}_k^{e\,*} \cdot \mathbf{s}_{k'}^e \, \mathrm{d}V = \delta_{kk'} \ . \tag{2.28}$$

Eq. (2.27) arises as we decompose $\mathcal{H}$ into its unperturbed (elastic) and perturbed parts: that is, $[\mathbf{s}_k^e, \mathcal{H}^e \mathbf{s}_k] = [\omega_k^e]^2$ and we define $V_{kk'} \equiv [\mathbf{s}_k^{e*}, \delta\mathcal{H}(\nu)\mathbf{s}_{k'}^e]$ whose matrix elements are

$$V_{kk'}(\nu) = \int_V \delta\kappa(\nu)(\nabla \cdot \mathbf{s}_k^{e\,*})(\nabla \cdot \mathbf{s}_{k'}^e)\, dV + 2\int_V \delta\mu(\nu)\, \mathbf{d}_k^{e\,*} : \mathbf{d}_{k'}^e \, dV \tag{2.29}$$

and elements of the matrix $\mathbf{W}$ are given by

$$W_{kk'} = \int_V \rho\, \mathbf{s}_k^{e*} \cdot (i\mathbf{\Omega} \times \mathbf{s}_{k'}^e)\mathrm{d}V \ . \tag{2.30}$$

As in Section 2.2.3, we must also consider the system of the anti-Earth where anelastic modes are denoted as

$$\bar{\mathbf{s}}_k = \sum_{k'} \overline{\chi}_{kk'} \mathbf{s}^{e\,*}_{k'} \ , \tag{2.31}$$

where the coefficients $\overline{\chi}$ are prescribed by the equation

$$[\omega^2 + \mathbf{V}(\nu) - 2\nu\mathbf{W} - \nu^2]\overline{\chi} = \mathbf{0} \ . \tag{2.32}$$

The normalization of the eigenvectors, χ and $\overline{\chi}$, is defined by

$$\sum_{k'} \overline{\chi}_{kk'}\,\chi_{k'k} - \frac{1}{\nu_k}\sum_{k',k''} \overline{\chi}_{k''k} W_{k''k'}\chi_{k'k} - \frac{1}{2\,\nu_k}\sum_{k',k''} \overline{\chi}_{k''k}\,\partial_\nu V_{k''k'}(\nu_k)\chi_{k'k} = 1 \ . \tag{2.33}$$

The matrix $\mathbf{V}$ governs how modes couple through anelasticity and performing the diagonalization of eq. (2.27) provides the expansion coefficients necessary in eq. (2.26) and similarly eqs (2.31) and (2.32). Thus far we have made no assumption about the aspherical structure of this Earth model. Aspherical structure and rotation cause coupling across modes of different degrees, together with coupling of non-degenerate orders of $2\ell + 1$ within each mode, as a result of the broken symmetry. In Section 2.2.5 we discuss this coupling. If we assume a non-rotating Earth with spherically-symmetric anelastic structure, only coupling between $(2\ell + 1)$-degenerate modes of same degree but different overtones occurs. It is unlikely that current uncertainties in geodetic measurements of body tides allow for constraints to be placed on aspherical dissipation (e.g., Kim & Shibuya, 2013).

The final issue to be addressed concerns an additional set of normal modes that become important at lower frequencies beyond the seismic band. Within the seismic band, anelastic eigenfrequencies are found in the complex plane just above the real frequency axis. As we have discussed, the set of ω_k are found using perturbation theory and their associated departure from the real axis, $i\gamma_k$, is determined by considering the Q structure at their real frequencies, ω_k. However, a set of modes also exists along the imaginary axis (Yuen & Peltier, 1982). These relaxation modes (referred to as 'quasi-static modes' in Yuen & Peltier, 1982) are purely decaying modes and they are analogous to normal modes treated in studies of glacial isostatic adjustment (e.g., Wu, 1978; Tromp & Mitrovica, 1999).

Fig. 2.1 is a schematic diagram illustrating the location of this complete set of modes on the complex plane. Al-Attar (2007) demonstrated that summation of the signal associated with this set of modes to form a time-domain response (see Section 2.2.6) is equivalent to inverting the frequency-domain response by Cauchy's residue theorem (see also Wu, 1978). For such an inversion, the Bromwich line that runs along the real axis from $[-\infty, +\infty]$ is deformed to form a semicircle over the upper half of the complex plane in the case of $t > 0$. Singularities found along the imaginary axis may be modal (i.e., poles) or, more likely for the Earth, multi-valued, in which case the Bromwich line must be further deformed to consider branch cuts. To avoid confusion, we will use the term 'seismic modes' when discussing modes near the real axis, and 'relaxation modes' for those along the imaginary axis. In Section 2.3.1 we use a simple example to demonstrate that the inclusion of the relaxation modes is necessary for the accurate incorporation of anelastic effects within our normal mode formalism for computing the tidal response.

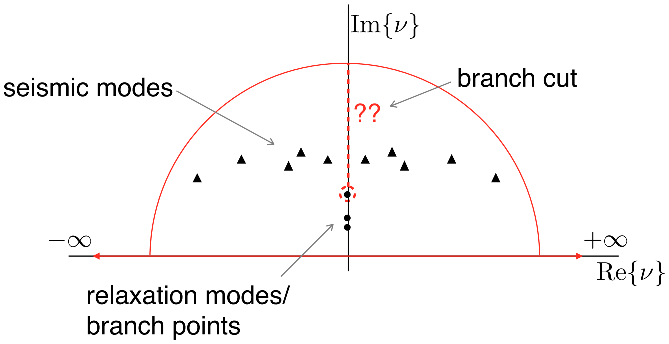

FIGURE 2.1: A schematic illustration of the location of eigenfrequencies relevant to the tidal problem on the complex plane. The red line indicates how the Bromwich contour may be deformed in applying Cauchy residue theory to determine the time-domain response.

2.2.5 Perturbation Theory for an Aspherical Earth

In this section we specify how to use the framework described above to consider an Earth with aspherical mantle structure. We note that Qin et al. (2014) have recently derived a semi-analytical perturbation theory to predict the impact of aspherical elastic structure on lunar body tides. In contrast to the normal mode approach described herein, their perturbation theory is applied directly to the differential equations of motion and perturbed gravity. Moreover, the Qin et al. (2014) approach treats the underlying coupling between modes of deformation in stages, whereas our normal mode approach treats the full coupling in one step, and their study does not include the consideration of rotational effects, which is a significantly smaller effect on tidal deformation of the Moon.

Following Dahlen & Tromp (1998), we restate the deformation problem in the form of a variational principle (Rayleigh's principle) where the action, $\mathcal{I}$, is defined as

$$\mathcal{I} = \tfrac{1}{2}\nu^2[\overline{\mathbf{s}}, \mathbf{s}] - \nu[\overline{\mathbf{s}}, i\boldsymbol{\Omega} \times \mathbf{s}] - \tfrac{1}{2}[\overline{\mathbf{s}}, \mathcal{H}(\nu)\mathbf{s}] \ . \tag{2.34}$$

Note that eq. (2.34) holds for both a spherically-symmetric and aspherical Earth. To first order, the variation in this expression is given by

$$\delta\mathcal{I} = \tfrac{1}{2}[\delta\overline{\mathbf{s}}, \nu^2\mathbf{s} - 2i\nu\boldsymbol{\Omega} \times \mathbf{s} - \mathcal{H}(\nu)\mathbf{s}] + \tfrac{1}{2}[\delta\mathbf{s}, \nu^2\overline{\mathbf{s}} + 2i\nu\boldsymbol{\Omega} \times \overline{\mathbf{s}} - \mathcal{H}(\nu)\overline{\mathbf{s}}] \ , \tag{2.35}$$

where we have made use of the duality product (eqs 2.11, 2.12 and 2.13). If, and only if, $\mathbf{s}$ and $\overline{\mathbf{s}}$ are the eigenfunctions for the Earth and anti-Earth, respectively, and have the associated eigenfrequencies ν_k, then $\delta\mathcal{I} \to 0$ for arbitrary and independent variations of $\delta\overline{\mathbf{s}}$ and $\delta\mathbf{s}$.

We next introduce an Earth model with small lateral variations in structure:

$$\rho(\mathbf{r}) = \rho^0(r) + \delta\rho(\mathbf{r}) \ , \tag{2.36}$$

$$\mu(\mathbf{r}) = \mu^0(r) + \delta\mu(\mathbf{r}) \ , \tag{2.37}$$

$$\kappa(\mathbf{r}) = \kappa^0(r) + \delta\kappa(\mathbf{r}) \ , \tag{2.38}$$

where hereafter the superscript '0' denotes spherically-symmetric quantities. We note that the introduction of aspherical structure implies the existence of deviatoric pre-stress. Woodhouse & Dahlen (1978) derived a general form of the seismic normal mode problem that included deviatoric pre-stresses. However, Dahlen (1972) investigated the contribution of this stress field on the wave propagation problem and found that it could be neglected since the ratio of non-hydrostatic stresses over the isotropic stress is small. The ratio is also small for the tidal problem, and so in the following derivation we neglect any deviatoric pre-stress.

To continue, we expand the eigenfunctions of the aspherical Earth and anti-Earth, $\mathbf{s}$ and $\overline{\mathbf{s}}$, using the unperturbed, $(2\ell + 1)$-degenerate, singlet basis functions $\mathbf{s}_k^0$ as follows

$$\mathbf{s} = \sum_k q_k \mathbf{s}_k^0 \ , \tag{2.39}$$

$$\overline{\mathbf{s}} = \sum_k \overline{q}_k \mathbf{s}_k^{0*} \ , \tag{2.40}$$

where the expansion depends on weights $\overline{q}_k$ and q_k. These unperturbed eigenfunctions are those associated with a spherical, non-rotating, elastic and isotropic Earth (SNREI). Substituting these expansions into the action $\mathcal{I}$ (eq. 2.34), yields

$$\mathcal{I} = \tfrac{1}{2}\overline{\mathbf{q}}^T[\nu^2\mathbf{T} - 2\nu\mathbf{W} - \mathbf{V}'(\nu)]\mathbf{q} \ , \tag{2.41}$$

where elements of the kinetic energy matrix $\mathbf{T}$, the potential energy matrix $\mathbf{V}'$ and the Coriolis matrix $\mathbf{W}$ are given by

$$T_{kk'} = \int_V \rho\, \mathbf{s}_k^{0*} \cdot \mathbf{s}_{k'}^0 \mathrm{d}V \ , \tag{2.42}$$

$$V'_{kk'} = \int_V \rho\, \mathbf{s}_k^{0*} \cdot \mathcal{H}(\nu) \mathbf{s}_{k'}^0 \mathrm{d}V \ , \tag{2.43}$$

$$W_{kk'} = \int_V \rho\, \mathbf{s}_k^{0*} \cdot i\boldsymbol{\Omega} \times \mathbf{s}_{k'}^0 \mathrm{d}V \ . \tag{2.44}$$

We label the matrix $\mathbf{V}'$ to avoid confusion with the matrix $\mathbf{V}$ in Section 2.2.4, though they both act to perturb the potential energy. The variation of eq. (2.41) (i.e., eq. 2.35) may be written as

$$\delta\mathcal{I} = \tfrac{1}{2}\delta\overline{\mathbf{q}}^T[\nu^2\mathbf{T} - 2\nu\mathbf{W} - \mathbf{V}'(\nu)]\mathbf{q} + \tfrac{1}{2}\delta\mathbf{q}^T[\nu^2\mathbf{T} + 2\nu\mathbf{W} - \mathbf{V}'(\nu)]\overline{\mathbf{q}} \ , \tag{2.45}$$

where $\mathbf{T}^T = \mathbf{T}$, $\mathbf{V}'^T(\nu) = \mathbf{V}'(\nu)$ and $\mathbf{W}^T = -\mathbf{W}$. If, and only if, $\mathbf{q}$ and $\overline{\mathbf{q}}$ are the eigenvector and dual eigenvector with associated eigenfrequency ν, then for arbitrary and independent variations $\delta\mathbf{q}$ and $\delta\overline{\mathbf{q}}$, the variation $\delta\mathcal{I} \to 0$, leaving two quadratic eigenvalue problems:

$$[\mathbf{V}'(\nu) + 2\nu\mathbf{W} - \nu^2\mathbf{T}]\mathbf{q} = \mathbf{0} \tag{2.46}$$

$$[\mathbf{V}'(\nu) - 2\nu\mathbf{W} - \nu^2\mathbf{T}]\overline{\mathbf{q}} = \mathbf{0} \ . \tag{2.47}$$

To implement these perturbations in Earth structure, we express the density and elastic structure in terms of spherical harmonics:

$$\rho(r,\theta,\lambda) = \sum_{s=1}^{s_{max}} \sum_{t=-s}^{t=s} \delta\rho_{st}(r) Y_{st}(\theta,\lambda) \ , \tag{2.48}$$

$$\kappa(r,\theta,\lambda) = \sum_{s=1}^{s_{max}} \sum_{t=-s}^{t=s} \delta\kappa_{st}(r) Y_{st}(\theta,\lambda) \ , \tag{2.49}$$

$$\mu(r,\theta,\lambda) = \sum_{s=1}^{s_{max}} \sum_{t=-s}^{t=s} \delta\mu_{st}(r) Y_{st}(\theta,\lambda) \ , \tag{2.50}$$

where s and t are harmonic degree and order, respectively. The manner in which a pair of singlet (or reference) eigenmodes $\mathbf{s}_k$ and $\mathbf{s}_{k'}$ interact in the presence of structure $\{s,t\}$ is determined by order-independent Woodhouse kernels (Woodhouse, 1980), which were extended by Mochizuki (1986) to include the effects of transverse anisotropy. To illustrate how these kernels are used to populate the relevant matrices, consider the following simplified expressions:

$$T_{kk'} = \delta_{kk'} + \sum_{st} \zeta(\ell,m;\ell',m';s,t) \int_0^a \delta\rho_{st} T_\rho^{\ell s \ell'} r^2 \mathrm{d}r \ ; \tag{2.51}$$

$$V_{kk'} = [\nu_k^0]^2 \delta_{kk'} + \sum_{st} \zeta(\ell,m;\ell',m';s,t) \int_0^a \left(\delta\kappa_{st} V_\kappa^{\ell s \ell'} + \delta\mu_{st} V_\mu^{\ell s \ell'} + \delta\rho_{st} V_\rho^{\ell s \ell'} \right) r^2 \mathrm{d}r \ . \tag{2.52}$$

Here, ζ represents a pre-factor that dictates the modal interactions expressed via Wigner 3-j symbols. Note that we have replaced the index k used in previous sections to make explicit the dependence of each mode on spherical harmonic degree and order, ℓ and m, respectively, and the overtone number, n. ζ gives rise to what is commonly known as a 'selection rule' between modes and a given structure. Selection rules (i.e., whether two modes will couple) are governed by the geometry of the modes and the structure in question. $T_\rho^{\ell s \ell'}$, $V_\kappa^{\ell s \ell'}$, $V_\mu^{\ell s \ell'}$ and $V_\rho^{\ell s \ell'}$ are the Woodhouse kernels which are formed by combining the reference eigenfunctions of modes k and k'. Additional kernels

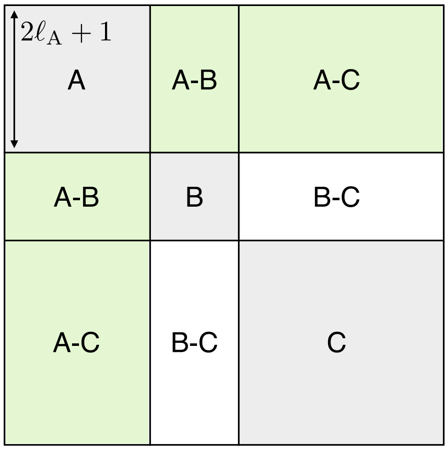

FIGURE 2.2: A schematic illustration of either matrix $\mathbf{T}$ or $\mathbf{V}'$ for the simple case of only 3 normal modes: A, B and C. The square, on-diagonal submatrices are self-coupling matrices. The dimensions of each self-coupling matrix are $(2\ell + 1) \times (2\ell + 1)$, and ℓ_{A} is the degree of mode A. The off-diagonal sub-matrices are cross-coupling matrices. If mode A is of the same degree and order as the forcing, the coupling of modes with A is termed 'direct coupling' (shown by green shaded sub-matrices). All other cross-coupling are termed 'indirect coupling' (shown by unshaded sub-matrices).

also exist for aspherical discontinuities. For the case of N modes, this results in a matrix of N^2 sub-matrices. Explicit expressions for the matrix elements may be found in Woodhouse (1980). (Note that the expressions in this paper assume real spherical harmonics, whereas those in Woodhouse (1980) assume complex spherical harmonics. The appropriate transformation from real to complex spherical harmonics can be found in Appendix D of Dahlen & Tromp (1998).)

Fig. 2.2 provides a schematic representation of either matrix $\mathbf{T}$ or $\mathbf{V}'$ in the case when only three modes, A, B and C, are considered. (In practice, many more modes are considered.) The square, on-diagonal sub-matrices (shaded gray), labeled 'A', 'B' and 'C', are sub-matrices associated with self-coupling within each mode. These sub-matrices are $(2\ell+1) \times (2\ell+1)$ in size, where ℓ is the degree of the mode in question. The off-diagonal matrices are cross-coupling matrices; i.e., they govern interactions between different modes. After diagonalizing this large matrix, the interactions of all the modes form the new eigenfunctions $\mathbf{s}$ (and $\overline{\mathbf{s}}$) in one step. In Section 2.3.2 we revisit this schematic illustration when considering how the selection rules play a role in the tidal response of an aspherical

Earth.

2.2.6 SEMI-DIURNAL OR LONG-PERIOD BODY TIDE RESPONSE

Eqs (2.9), (2.10), (2.16) and (2.17) provide a framework for predicting the semi-diurnal or long-period response of an aspherical, rotating and anelastic Earth to tidal forcing. Using these relations, the eigenmodes combine to form the rotating, anelastic Earth's Green's function, $\mathbf{G}$, given by (Lognonné, 1991):

$$\mathbf{G}(\mathbf{r},\mathbf{r}';t) = \sum_k (2i\nu_k)^{-1}\mathbf{s}_k(\mathbf{r})\bar{\mathbf{s}}_k(\mathbf{r}')\exp(i\nu_k t) \ . \tag{2.53}$$

When considering only the seismic modes, one notes that if ν_k and $\mathbf{s}_k$ are eigenfrequencies and eigenfunctions of the Earth, then, according to the relation stated in Section 2.2.2 (where $\boldsymbol{\Lambda}^*(\nu) = \boldsymbol{\Lambda}(-\nu^*)$ to satisfy causality in the time-domain), so too are $-\nu_k^*$ and $\mathbf{s}_k^*$. It follows that in seismological applications, where relaxation modes are ignored, the Green's function may be stated as

$$\mathbf{G}(\mathbf{r},\mathbf{r}';t) = \mathrm{Re}\sum_k (i\nu_k)^{-1}\mathbf{s}_k(\mathbf{r})\bar{\mathbf{s}}_k(\mathbf{r}')\exp(i\nu_k t) \ , \tag{2.54}$$

including only modes where $\mathrm{Re}\{\nu_k\} > 0$ in the summation. By using eq. (2.53) the displacement tidal response, $\mathbf{s}$, is then computed via a space-time convolution:

$$\begin{aligned}\mathbf{s}(\mathbf{r},t) = \ &-\int_{-\infty}^{t}\int_{V'}\rho(\mathbf{r}')\,\mathbf{G}(\mathbf{r},\mathbf{r}';t-t')\cdot\nabla\Psi(\mathbf{r}',t')\,\mathrm{d}V'\mathrm{d}t' \\ &-\int_{-\infty}^{t}\int_{V'}\rho(\mathbf{r}')\,\mathbf{B}(\mathbf{r},\mathbf{r}';t-t')\cdot\nabla\Psi(\mathbf{r}',t')\,\mathrm{d}V'\mathrm{d}t' \ .\end{aligned} \tag{2.55}$$

The term $\mathbf{B}$ is the contribution from any branch cuts. In general, the time-integration of the Green's function will yield a transient response upon initiation of the forcing. If we begin the forcing well before the observation time t, this transient response will be unimportant. Accordingly, we begin the time-integration at $t' = -\infty$ to isolate the steady-state solution.

The eigenmodes $\mathbf{s}_k$ and $\bar{\mathbf{s}}_k$ have two forms: spheroidal and toroidal (commonly labeled as ${}_n\mathcal{S}_{\ell m}$ and ${}_n\mathcal{T}_{\ell m}$, respectively). These can be highlighted by decomposing $\mathbf{s}$ (and $\bar{\mathbf{s}}$) into contributions from each eigenfunction $\mathcal{U}_k$, $\mathcal{V}_k$ and $\mathcal{W}_k$ (and $\overline{\mathcal{U}}_k$, $\overline{\mathcal{V}}_k$ and $\overline{\mathcal{W}}_k$):

$$\mathbf{s} = \sum_{n,\ell,m} {}_n\mathcal{U}_{\ell m}\mathbf{P}_{\ell m} + {}_n\mathcal{V}_{\ell m}\mathbf{B}_{\ell m} + {}_n\mathcal{W}_{\ell m}\mathbf{C}_{\ell m} \ , \tag{2.56}$$

$$\bar{\mathbf{s}} = \sum_{n,\ell,m} {}_n\overline{\mathcal{U}}_{\ell m}\mathbf{P}_{\ell m} + {}_n\overline{\mathcal{V}}_{\ell m}\mathbf{B}_{\ell m} + {}_n\overline{\mathcal{W}}_{\ell m}\mathbf{C}_{\ell m} \ . \tag{2.57}$$

The terms involving $\mathcal{U}_k$ and $\mathcal{V}_k$ constitute the spheroidal modes and the last term with $\mathcal{W}_k$ constitutes the toroidal modes. $\mathbf{P}_{\ell m}$, $\mathbf{B}_{\ell m}$ and $\mathbf{C}_{\ell m}$ are the vector spherical harmonics

$$\mathbf{P}_{\ell m} = Y_{\ell m}\hat{\mathbf{r}} \ , \tag{2.58}$$

$$\mathbf{B}_{\ell m} = \frac{1}{\sqrt{\ell(\ell+1)}}\nabla_1 Y_{\ell m} \ , \tag{2.59}$$

$$\mathbf{C}_{\ell m} = -\frac{1}{\sqrt{\ell(\ell+1)}}\hat{\mathbf{r}} \times \nabla_1 Y_{\ell m} \ , \tag{2.60}$$

and ${}_n\mathcal{U}_{\ell m}$, ${}_n\mathcal{V}_{\ell m}$, and ${}_n\mathcal{W}_{\ell m}$ (or, $\mathcal{U}_k$, $\mathcal{V}_k$, and $\mathcal{W}_k$, respectively) are the complex displacement eigenfunctions found by substituting eq. (2.56) into (2.26), which yields

$$\mathcal{U}_k = \sum_{k'} \chi_{kk'}\, U_{k'} \ , \tag{2.61}$$

$$\mathcal{V}_k = \sum_{k'} \chi_{kk'}\, V_{k'} \ , \tag{2.62}$$

$$\mathcal{W}_k = \sum_{k'} \chi_{kk'}\, W_{k'} \ , \tag{2.63}$$

where U_k, V_k and W_k are the real unperturbed eigenfunctions. We emphasize this distinction to highlight the effects discussed in Section 2.2.4. For spherically-symmetric seismic applications, χ would simply be approximated as the identity matrix. In any event, convolving the Green's function, $\mathbf{G}$, which involves the summation of modes defined by relations in Section 2.2.3, with the time-domain forcing, yields the tidal response.

2.3 Some Illustrative Case Studies

The calculations below have two purposes: first, to illustrate predictions based on the normal mode theory we have developed, and, second, to compare these predictions with either published results or results generated using an independent, finite volume numerical scheme. These case studies are divided into two parts: Section 2.3.1 considers only spherically-symmetric Earth models and Section 2.3.2 uses the perturbation theory described in Section 2.2.5 to consider aspherical Earth models. We note that the eigenfunctions and eigenfrequencies within the seismic band for any given spherically-symmetric Earth model were computed using the software MINEOS (Woodhouse, 1988; Masters et al., 2007).

2.3.1 Spherical Earth

Elastic Earth

In this subsection, we treat the simplest case of a SNREI Earth model. We introduce the basis functions for this Earth model, which in turn form the basis functions for the response of an anelastic Earth (see Section 2.2.4). In the SNREI case, two simplifications are made: $\mathbf{\Lambda}$ is purely real and $\mathbf{\Omega} = \mathbf{0}$. Thus, only one of the two eigenvalue problems (eqs 2.9 and 2.10) needs to be solved since the Coriolis operator vanishes.

For the present, elastic Earth model case, the Green's function approach outlined in Section 2.2.6 requires a minor modification. In particular, since there is no dissipation in the system, the extra, transient terms that appear at the onset of forcing do not disappear, in contrast to their decay in the anelastic case. So, in this subsection we solve the time-harmonic problem (with no initial conditions) given by the non-rotating, elastic version of eq. (2.3):

$$\mathcal{H}^e\mathbf{s} - [\omega_T]^2\mathbf{s} = -\nabla\tilde{\Psi}(\mathbf{r};\omega_T) \ , \tag{2.64}$$

where we expand the solution, $\mathbf{s}$ as

$$\mathbf{s} = \sum_k \beta_k \mathbf{s}_k \ . \tag{2.65}$$

The β_k are coefficients to be determined. Substituting this expansion into eq. (2.64) and using the relation

$$[\omega_k]^2\mathbf{s}_k = \mathcal{H}^e\mathbf{s}_k \ , \tag{2.66}$$

which is satisfied if $\mathbf{s}_k$ is an eigenfunction of $\mathcal{H}^e$, yields

$$([\omega_k^e]^2 - \omega_T^2)\sum_k \beta_k \mathbf{s}_k = -\nabla\tilde{\Psi} \ . \tag{2.67}$$

Taking the inner product of eq. (2.67) with $\mathbf{s}_k^*$ yields an expression for β_k:

$$\beta_k = \frac{1}{\omega_k^2 - \omega_T^2}\frac{[-\nabla\tilde{\Psi}, \mathbf{s}_k^*]}{[\mathbf{s}_k, \mathbf{s}_k^*]} \ . \tag{2.68}$$

Note that the normalization for a SNREI Earth model is $[\mathbf{s}_k, \mathbf{s}_{k'}^*] = 1$ when $k = k'$ and 0 otherwise. Using this normalization yields the time-domain response:

$$\mathbf{s}(\mathbf{r};t) = -\sum_k \frac{\mathbf{s}_k(\mathbf{r})}{\omega_k^2 - \omega_T^2} \int_{V'} \rho(\mathbf{r}')\mathbf{s}_k^*(\mathbf{r}') \cdot \nabla\tilde{\Psi}(\mathbf{r};\omega_T) \exp[i\omega_T t] \mathrm{d}V' \ . \tag{2.69}$$

Finally, using eq. (2.1), we have

$$\nabla\tilde{\Psi}(\mathbf{r};\omega_T) = -\sum_{\ell=0}^{\infty} \sum_{m=-\ell}^{m=\ell} \tilde{c}_{\ell m}(\omega_T) \frac{r^{\ell-1}}{a^{\ell}} \left[\ell \mathbf{P}_{\ell m}(\theta,\lambda) + \sqrt{\ell(\ell+1)}\mathbf{B}_{\ell m}(\theta,\lambda)\right] \ . \tag{2.70}$$

We will compare results generated using eqs (2.69)–(2.70) with Love numbers for a SNREI Earth computed using the formalism outlined by Farrell (1972). The radial- and degree-dependent dimensionless Love numbers are defined by the expressions

$$s_r(\mathbf{r};t) = \sum_{\ell} \frac{h_\ell(r)}{g} \Psi(\mathbf{r};t) \ , \tag{2.71}$$

$$\mathbf{s}_t(\mathbf{r};t) = \sum_{\ell} \frac{l_\ell(r)}{g} \nabla\Psi(\mathbf{r};t) \ . \tag{2.72}$$

Here, s_r and $\mathbf{s}_t$ are the radial and tangential displacement, respectively, and h and l are the Love numbers associated with these displacements. The Love number calculation ignores inertia and computing these numbers involves solving a coupled system of first order differential equations that are expressed in a general propagator form (Farrell, 1972). In the normal mode formalism, the static Love numbers are given by the following expressions once eq. (2.69) is calculated and assuming no inertia (i.e., $\omega_T \to 0$).

$$h_\ell(r) = -g \sum_{n=0}^{\infty} \frac{{}_nU_\ell(r)}{{}_n\omega_\ell^2} \int_0^a \rho \frac{r^{\ell+1}}{a_\ell} \left[\ell_n U_\ell + \sqrt{\ell(\ell+1)}_n V_\ell\right] \mathrm{d}r \ , \tag{2.73}$$

$$l_\ell(r) = -g \sum_{n=0}^{\infty} \frac{{}_nV_\ell(r)}{{}_n\omega_\ell^2} \int_0^a \rho \frac{r^{\ell+1}}{a_\ell} \left[\ell_n U_\ell + \sqrt{\ell(\ell+1)}_n V_\ell\right] \mathrm{d}r / \sqrt{\ell(\ell+1)} \ . \tag{2.74}$$

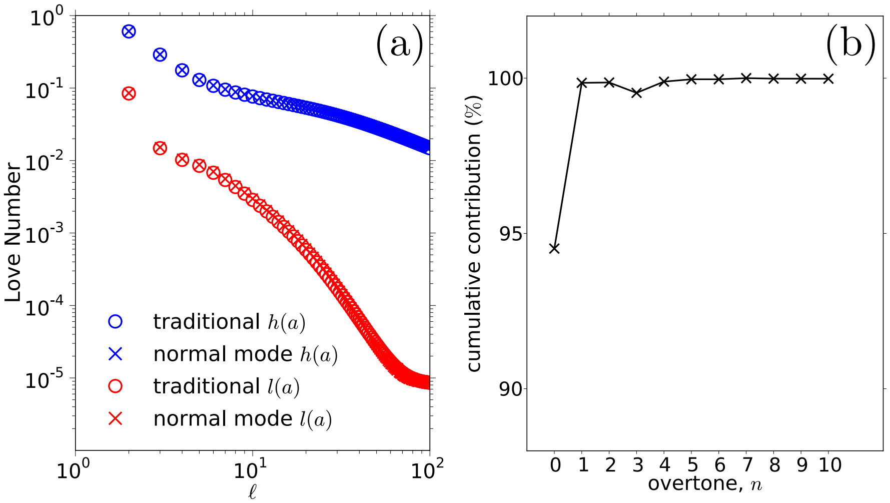

FIGURE 2.3: (a) Tidal Love numbers evaluated at $r = a$ for the SNREI version of PREM (Dziewonski & Anderson, 1981) using traditional Love number theory ($\circ$) and normal mode theory ($\times$). The h_ℓ Love number (blue) is associated with radial displacement and the l_ℓ Love number (red) relates to tangential displacement. (b) Contribution of each ${}_n\mathcal{S}_2$ mode towards the $h_2(a)$ Love number. See the summation in eq. (2.73).

Note that in the case of the $(2\ell + 1)$-degenerate SNREI model, we drop m when referring to modes (${}_n\mathcal{S}_\ell$) and eigenfunctions (${}_nU_\ell$ and ${}_nV_\ell$). Fig. 2.3(a) shows the calculation of static Love numbers at $r = a$ based on both our normal mode approach (eqs 2.73 and 2.74) and the formalism of Farrell (1972) as a function of spherical harmonic degree using the SNREI version of the model PREM (Dziewonski & Anderson, 1981). The agreement is excellent.

The advantage of the normal mode approach relative to classic Love number theory is that it allows examination of the contribution from each mode and this provides insight into the physics and sensitivity of the associated response. If we consider the semi-diurnal tide case, the forcing is limited to $\ell = 2$ and $m = 2$ and the response of a SNREI Earth involves the same degree and order. Fig. 2.3(b) partitions the h_2 Love number into contributions from each overtone n, demonstrating that the ${}_0\mathcal{S}_2$ mode contributes $\sim$ 95% of the response. It is worth noting that not all normal mode contributions to h_2 will have the same sign, since a given mode's contribution will depend upon both the degree of excitation and the manner in which the mode samples the Earth. This is evident

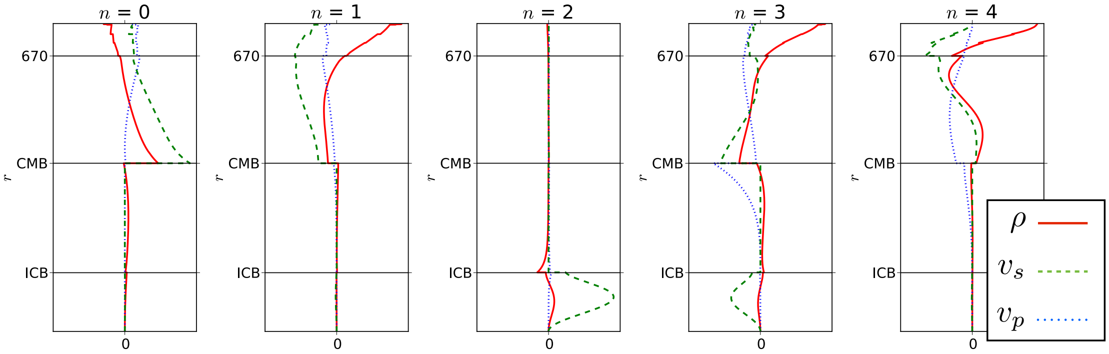

FIGURE 2.4: Depth-dependent sensitivity kernels for the ${}_n\mathcal{S}_2$ set of modes. Red solid line – density, ρ; green dashed line – shear velocity, v_{S}; blue dotted line – compressional velocity, v_{P}. All curves are normalized such that, in each panel, only relative values are of importance.

from the results for ${}_3\mathcal{S}_2$ (or $n = 3$) in Fig. 2.3(b), which has a contribution of opposite sign to the other modes. It is clear that, within the limits of observation, the summation in eq. (2.73) can safely be truncated by $n \sim 10$, making any tidal calculation computationally inexpensive.

Fig. 2.4 shows the depth sensitivity kernels for the relative shift in eigenfrequency of each mode (for n up to 4) for density and two seismic velocities, v_{P} and v_{S}, which are the three parameters most commonly discussed in the seismic problem (expressions for these kernels may be found in Dahlen & Tromp, 1998). For the most important parameter in the geodynamics problem, the mass density ρ, ${}_0\mathcal{S}_2$ has the most sensitivity in the lower mantle. Each overtone shown in Fig. 2.4 has differing depth sensitivities. Perhaps the most striking example is ${}_2\mathcal{S}_2$, which has no sensitivity in the mantle or most of the outer core; its main sensitivities are limited to inner core boundary and within the inner core. These simple examples illustrate the fundamental connection between the Earth's free oscillations, for the earthquake response, and forced oscillations, for the tidal response.

ANELASTIC EARTH

In the following, we present some numerical predictions using a simple anelastic Earth model designed to demonstrate the theory presented in Section 2.2.4. To simplify the discussion, we set

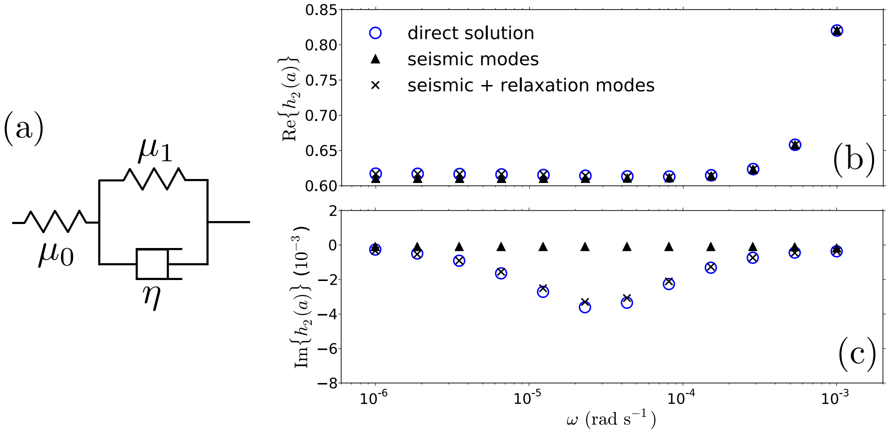

FIGURE 2.5: (a) A schematic illustration of a standard linear solid (or Zener solid; Zener, 1948) composed of two mechanical springs ($\mu_0,\ \mu_1$) and one dashpot (η). (b) The real part of the $h_2(r = a)$ Love number across different frequencies computed using two methods: the direct solution (blue) and the normal mode method (black). (c) The same as (b), except for the imaginary part of $h_2(r = a)$.

$\mathbf{\Omega} = \mathbf{0}$, which results in $\mathbf{W} = \mathbf{0}$ in eq. (2.27). (Thus, we need only solve for the real Earth. In this case, the normalizations change, and we substitute $\overline{\chi}$ for χ in eq. (2.33).) We also assume that the Earth's rheology may be modeled as a single standard linear solid using simple piecewise-constant depth dependence. Adopting such a simple Earth model avoids a contribution to the response from branch cuts, although our theory is fully capable of incorporating such complexity.

The 1-D mechanical analogue for this Earth model is shown in Fig. 2.5(a), where in calculations below we take the unrelaxed limit (μ_0) to be that of PREM, and μ_1 to be $20 \times \mu_0$ in the upper mantle and $50 \times \mu_0$ in the lower mantle. The viscosity, η, is $\tau\mu_1$ where we set τ, the characteristic time-scale, to be 10 hours. We choose τ to lie significantly beyond the seismic band to highlight the necessity of searching for relaxation modes outside this band. In general, the Earth model parameters have been chosen to yield a modulus reduction similar to that predicted by the PREM Q model across the seismic band. We assume no dissipation in κ.

Following Nowick & Berry (1972), the frequency dependence of μ becomes

$$\mu(\nu) = \mu_0 - \frac{\delta\mu}{1 + i\nu\tau_\epsilon} \ , \tag{2.75}$$

where

$$\delta\mu = \mu_0 \left(1 - \frac{\mu_1}{\mu_0 + \mu_1}\right) \ . \tag{2.76}$$

There are two characteristic time-scales, τ_ϵ and τ_σ, where

$$\tau_\epsilon = \frac{\eta}{\mu_0 + \mu_1} \ , \tag{2.77}$$

$$\tau_\sigma = \frac{\eta}{\mu_1} \ . \tag{2.78}$$

As described in Section 2.2.4 we expect the elastic eigenfrequency to be perturbed by $\delta\omega_k$ due to the reduction in the shear modulus (see eq. 2.75). The imaginary perturbation γ_k will be due to Q_k, where from eq. (2.19) the Q of a standard linear solid is given by

$$Q_\mu^{-1}(\omega) = \frac{\omega(\tau_\sigma - \tau_\epsilon)}{1 + \omega^2\tau_\sigma\tau_\epsilon} \ . \tag{2.79}$$

This form is a Debye peak centered around $\sqrt{\tau_\epsilon\tau_\sigma}$ (Zener, 1948).

In considering the anelastic eigenfunction in this numerical example, we apply one simplification relative to the theory described in Section 2.2.4; namely, we ignore anelastic cross-coupling and consider only self-coupling. For a spherically-symmetric Earth, modes are $(2\ell + 1)$-degenerate and only overtones of the same degree couple. In the body tide case, ignoring cross-coupling is an excellent assumption that avoids the necessity of solving the eigenvalue problem defined by eq. (2.27). To achieve this, we set all off-diagonal components for $\mathbf{V}$ to zero and in this case the matrix with elements $V_{kk'}$ reduces to a vector with elements V_k, where

$$V_k \approx 2i\omega_k \gamma_k \ . \tag{2.80}$$

Similarly, using eq. (2.33), $\chi_{kk'}$ reduces to χ_k, where

$$\chi_k^2 \approx [1 - \tfrac{1}{2\nu_k}\partial_\nu V_k(\nu)]^{-1} \ , \tag{2.81}$$

leaving the anelastic eigenfunction

$$\mathbf{s}_k = \chi_k \mathbf{s}_k^e \ . \tag{2.82}$$

Finally, we also search for modes along the imaginary axis, the so-called relaxation modes (see Fig. 2.1). Once the anelastic eigenfrequencies and eigenfunctions are found, we perform the convolution in eq. (2.55), where $\mathbf{B} = \mathbf{0}$, using the version of the Green's function given by eq. (2.53).

To investigate the importance of the relaxation modes in modeling the tidal response we use the normal mode theory described in Section 2.2.4 and above to calculate the Love number $h_2(a)$ over a frequency range spanning three orders of magnitude in period, from $\sim$ 2 hours to 100 days. In Figs 2.5(b,c) we compare results in the cases where the relaxation modes are included, or not included, in the normal mode summation. We also compare these results to predictions generated using a direct solution approach (Hara et al., 1993; Al-Attar, 2007). The direct solution method solves the forced equation (eq. 2.3) and does not involve a summation of the anelastic eigenfunctions and eigenfrequencies, and it thus serves as an independent check on our normal mode treatment of the tidal problem. The lowest frequency seismic mode, ${}_0\mathcal{S}_2$, has an eigenfrequency of approximately 1 hour^{-1}. Thus, the set of seismic modes will not capture any anelastic processes at periods greater than about 1 hour. Since our rheological (standard linear solid) model has an attenuation that peaks near 10 hours, the normal mode expansion that includes only the seismic modes is insufficient to

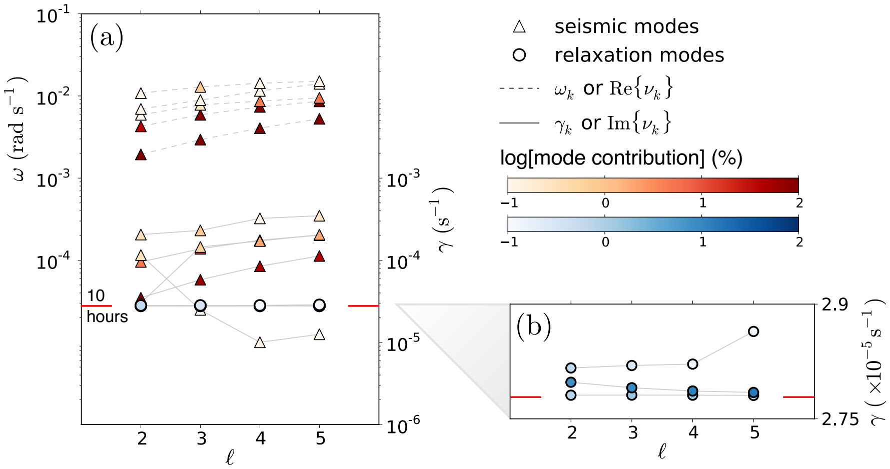

FIGURE 2.6: (a) The left vertical axis shows the real part of ν_k (oscillatory frequencies). The right vertical axis shows the imaginary part of ν_k (inverse decay times). The orange symbols denote seismic modes while the blue symbols are relaxation modes. The gray lines connect modes of equivalent overtone, n, where dashed (solid) lines are for the real (imaginary) part of eigenfrequencies. The color intensity indicates each mode's contribution to the long-term Love number. (b) An enlarged version of (a) focusing only on relaxation modes.

accurately predict the impact of anelasticity on the tidal response. In contrast, the calculation based on the full set of (seismic plus relaxation) modes accurately reproduces the response computed using the direct solution method.

In the seismic literature, mode catalogues are often displayed using so-called dispersion diagrams. Fig. 2.6 shows a dispersion diagram that includes low frequency seismic modes together with an analogue, for the case of the relaxation modes, that is often adopted in studies of glacial isostatic adjustment. Fig. 2.6(a) shows both Re$\{\nu_k\}$ and Im$\{\nu_k\}$ for the seismic modes (orange-scale triangles), where the former represent frequencies of oscillation and the latter are inverse decay times. Note that these two sets of orange-scale data points (dashed and solid lines) are from a single set of modes. The inverse decay times for the relaxation modes (blue-scale circles) are shown using a smaller frequency range in Fig. 2.6(b). As expected, given the adopted viscosity structure of the standard linear solid, the inverse decay times all cluster around 10 hours. The color scale indicates the contribution of each mode to the long-term h_2 Love number. As in Fig. 2.3(b), the contribution of the fundamental seismic mode to the tidal response is greatest in all cases.

2.3.2 ASPHERICAL EARTH

All tests described in this section are performed with elastic and isotropic Earth models. Our normal mode methodology and the finite volume scheme are hereafter referred to as NM and FV, respectively. The FV method computes the deformation of a non-rotating and self-gravitating Earth in response to a body force (Latychev et al., 2005, 2009). The governing equations are discretized on a tetrahedral grid within a spherical domain that incorporates arbitrary variability in crustal/mantle elastic and density structure. Latychev et al. (2009) used the FV scheme to predict the body tides on an aspherical Earth model, and we use it for the same purpose in several of the tests summarized below.

Since we only consider elastic models, we need only calculate the response to a single timestep of forcing. In all tests we apply a semi-diurnal tidal potential using the form given in eq. (2.1), where $c_{\ell m}$ is only nonzero for $\ell = 2$ and $m = \pm 2$. Recall that the $Y_{\ell m}$ spherical harmonic is complex and normalized as defined by Edmonds (1960), as discussed in Section 2.2.1. We set $c_{2\,\pm 2} = 5.5$, which leads to a maximum radial crustal displacement of 25 cm, typical for a semi-diurnal tide associated with a lunar potential forcing. If we denote the radial displacement response at the surface of the perturbed Earth model due to the tidal forcing by $s_r(\theta, \lambda)$, then a spherical harmonic decomposition of the response is given by:

$$s_r(\theta, \lambda) = \sum_{\ell=0}^{\infty} \sum_{m=-\ell}^{\ell} S_{\ell,m} Y_{\ell m}(\theta, \lambda) \ . \tag{2.83}$$

ASPHERICAL STRUCTURE

In the NM method, aspherical perturbations in Earth structure lead to mode coupling. As discussed in Section 2.2.5, the perturbations are expanded in spherical harmonics and they are incorporated into the perturbation matrices $\mathbf{T}$ and $\mathbf{V}'$ (Woodhouse, 1980). In this section, we focus only on spheroidal modes (and radial displacement) and we consider the modes listed in the right column of Table 2.2. We note that our theory is fully capable of considering toroidal-toroidal and toroidal-spheroidal coupling. Let us define a perturbation in structure of degree s and order t by the short-hand notation $\{s, t\}$.

Let us also consider a mode k of degree and order $\{\ell, m\}_k$ and overtone n and a mode k' of degree and order $\{\ell', m'\}_{k'}$ and overtone n'. For clarity, we include the subscripts k and k' in reference to these modes. The two modes will couple with the $\{s, t\}$ structure in a manner that satisfies the following selection rules:

$$m + m' + t = 0 \ , \tag{2.84}$$

$$|\ell - \ell'| \leq s \leq |\ell + \ell'| \ , \tag{2.85}$$

$$\ell' + \ell + s = \text{even} \ , \tag{2.86}$$

that are governed by the so-called 3-j triangle condition (in Section 2.2.5 we symbolically represented these conditions using the variable ζ). Note that the overtones n and n' do not play a role in these selection rules. Seismic normal mode perturbation theory accounts for both direct coupling and indirect coupling. That is to say, in the unperturbed problem, a body force of degree ℓ and order m will only excite a mode of the same ℓ and m. A perturbation of structure with the form $\{s, t\}$ will also allow this mode to couple to modes of different degree ℓ' and order m'. This coupling is illustrated by Fig. 2.2 where if mode 'A' has the same ℓ and m of the forcing, the off-diagonal matrices (shaded green) would be the result of direct coupling. These coupled modes will, in turn, indirectly couple, though weakly, to other modes in the presence of $\{s,t\}$ structure, under the same selection rules, so long as the modes are included in matrices $\mathbf{T}$ and $\mathbf{V}'$. In the terminology of Qin et al. (2014), direct coupling would be equivalent to first order coupling and indirect coupling includes all higher order couplings.

In this section, we describe two tests that involve idealized perturbations to the spherically-symmetric, non-rotating, elastic and isotropic (SNREI) version of the Earth model PREM (Dziewonski & Anderson, 1981). The perturbations are constant throughout the mantle. That is, an $\{s,t\}$ perturbation to the density field is applied to every layer in the mantle and has the following spatial dependence:

$$\rho(\theta,\lambda,r) = \rho^0(r)\left[1+\epsilon Y_{st}(\theta,\lambda)\right] \;, \tag{2.87}$$

where ϵ is an arbitrary scaling factor.

If $\epsilon = 0$ (i.e., a spherically-symmetric or reference Earth model), then the spherically-symmetric h_2^0 Love number is defined as

$$S^0_{2,2} = \frac{h^0_2}{g}\, c_{2\,2} \;. \tag{2.88}$$

In this special case, the Love number is independent of order.

In our first test, we impose a degree 2 and order 0 (i.e., $\{s,t\} = \{2,0\}$) lateral perturbation to the 1-D profile of ρ (as in eq. 2.87) for scaling factors ϵ ranging from 0.005 to 0.1. This range is equivalent to a maximum perturbation in the density of $(0.03\text{–}6.3)\%$. In this case, we generalize the above expression defining the Love number to be

$$S_{2,2} = \frac{h_{2,2}(\epsilon)}{g}\, c_{2\,2} \tag{2.89}$$

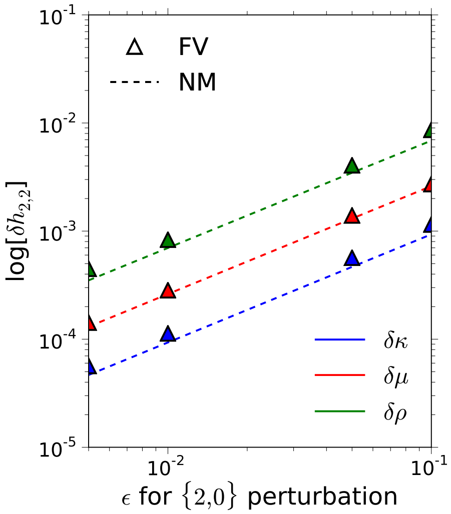

Figure 2.7: Benchmark comparison of results based on a finite volume ('FV') code (Latychev et al., 2009) and the normal mode perturbation theory ('NM') described in the text. A $c_{2\,2}$ body force is applied to an Earth model with imposed $\{2, 0\}$ structure of varying amplitude, where the latter is governed by the parameter ϵ (eq. 2.87). The figure shows the perturbation $\delta h_{2,2}$ (eq. 2.90) from results computed using SNREI PREM structure.

and the associated perturbation to the Love number as

$$\delta h_{2,2}(\epsilon) = h_{2,2}(\epsilon) - h_2^0 \; . \tag{2.90}$$

In Fig. 2.7 we show our normal mode calculation of $\delta h_{2,2}$ as a function of ϵ (green dashed line); the solid green triangles are calculations based on the FV scheme. We repeat all these calculations for independent perturbations in the shear and bulk moduli and the results are shown in red and blue, respectively. The results generated from the NM and FV calculations are in excellent agreement.

$\{s, t\}$	ϵ_{v_s}
$\{3, 1\}$	0.001
$\{2, 2\}$	0.01
$\{1, 1\}$	0.1

Table 2.1: The aspherical perturbation in Earth structure ($\{s, t\}$), and its amplitude, as prescribed by the parameter ϵ_{v_s}, for the second set of tests described in Section 2.3.2.

Next, we prescribe a perturbation in the shear velocity (v_s) structure of the mantle. We consider the three cases listed in Table 2.1. In the first, we adopt a scaling factor (which we denote by ϵ_{v_s}) of 0.001 and an aspherical perturbation from the spherically-symmetric structure of spherical harmonic degree 3 and order 1 ($\{3, 1\}$). The next case adopts $\epsilon_{v_\mathrm{s}} = 0.01$ and $\{2, 2\}$, and the final case has $\epsilon_{v_\mathrm{s}} = 0.1$ and $\{1, 1\}$. In each test, we use the following scaling relations to convert the shear velocity perturbation to perturbations in elastic moduli and density structure:

$$\frac{\partial \ln v_\mathrm{s}}{\partial \ln \rho} = 0.4 \ , \tag{2.91}$$

$$\frac{\partial \ln v_\mathrm{s}}{\partial \ln \mu} = 2.4 \ , \tag{2.92}$$

$$\frac{\partial \ln v_\mathrm{s}}{\partial \ln \kappa} = 0.5 \ . \tag{2.93}$$

These are plausible values in the simple case of constant mantle scaling (Bolton, 1996). Fig. 2.8 summarizes the results as a spherical harmonic decomposition of the total radial displacement response up to degree and order 6. We note that this figure provides no information in regard to the contributions of each overtone to the spatial signal $S_{\ell,m}$; the overtones we included in the calculation are listed in the right column of Table 2.2. The figures to the left were computed using the FV numerical scheme, while those on the right were computed using our NM approach. The match is excellent (note the log scale); discrepancies between predictions of displacement based on the NM and FV methods are significantly below the percent level. Benchmark tests in the case of the surface mass loading problem (Latychev et al., 2005) suggest numerical noise in the FV calculations on the order of several parts in $1,000$ and we conclude that the discrepancies that exist in Fig. 2.8 primarily reflect numerical error in the FV method.

The results in Fig. 2.8 largely reflect the selection rules described above. Consider, as an example, Fig. 2.8(f). The imposed perturbation in structure is $\{2, 2\}$ and, given the applied $c_{2,2}$ tidal poten-

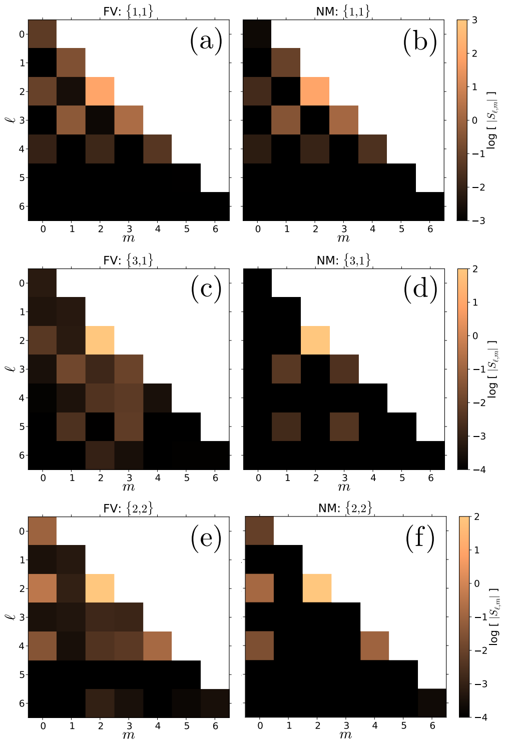

Figure 2.8: Benchmark comparison of results based on (left panels) a finite volume ('FV') code (Latychev et al., 2009) and (right panels) the normal mode perturbation theory ('NM') described in the text. A $c_{2\,2}$ body force is prescribed with three different idealized 3-D elastic mantle structures of form $\{s, t\}$ (see Section 2.3.2 for details). The predictions in each case are decomposed in terms of spherical harmonic coefficients $S_{\ell,m}$.

Group Coupling	Full Coupling
${}_0\mathcal{S}_2$	${}_0\mathcal{S}_2 - {}_2\mathcal{S}_1 - {}_0\mathcal{S}_3 - {}_0\mathcal{S}_4 - {}_1\mathcal{S}_2 -$
${}_0\mathcal{S}_4 - {}_1\mathcal{S}_2$	${}_0\mathcal{S}_0 - {}_0\mathcal{S}_5 - {}_1\mathcal{S}_3 - {}_2\mathcal{S}_2 - {}_3\mathcal{S}_1 -$
${}_2\mathcal{S}_2$	${}_0\mathcal{S}_6 - {}_3\mathcal{S}_2 - {}_1\mathcal{S}_4 - {}_2\mathcal{S}_3 - {}_1\mathcal{S}_5 -$
${}_3\mathcal{S}_2$	${}_2\mathcal{S}_4 - {}_4\mathcal{S}_1 - {}_4\mathcal{S}_1 - {}_3\mathcal{S}_3 - {}_2\mathcal{S}_5 -$
${}_5\mathcal{S}_1 - {}_4\mathcal{S}_2$	${}_1\mathcal{S}_6 - {}_1\mathcal{S}_0 - {}_2\mathcal{S}_6 - {}_5\mathcal{S}_1 - {}_4\mathcal{S}_2 -$
${}_5\mathcal{S}_2$	${}_3\mathcal{S}_4 - {}_6\mathcal{S}_1 - {}_4\mathcal{S}_3 - {}_2\mathcal{S}_5 - {}_3\mathcal{S}_5$

Table 2.2: Spheroidal mode coupling for the group and full coupling methods, capped at a maximum degree of 6, adopted in the test described in Section 2.3.2. The group coupling calculation considers 6 distinct groups whereas the full coupling calculation considers one single group with 30 modes.

tial, the geometry of the primary mode k to be excited is $\{2,2\}_k$. Substituting harmonics governing the aspherical structure and forcing into the 3-j triangle condition yield the selection rules:

$$\pm 2 + m' \pm 2 = 0 \;, \tag{2.94}$$

$$|2 - \ell'| \leq 2 \leq |2 + \ell'| \;, \tag{2.95}$$

$$\ell' + 2 + 2 = \text{even} \;. \tag{2.96}$$

Modes that satisfy all these conditions are $\{0,0\}_{k'}$, $\{2,0\}_{k'}$, $\{2,\pm 2\}_{k'}$, $\{4,0\}_{k'}$, $\{4,\pm 4\}_{k'}$; which are excited as a result of 'direct coupling'. These modes, in turn, couple to other modes, though this 'indirect coupling' tends to be weak. In the case of Fig. 2.8(f), this indirect coupling is evident in the excitation of $\{6,\pm 6\}_{k'}$. Substituting the harmonic $\{4,\pm 4\}_k$ as mode k in the 3-j triangle condition predicts that a $\{6,\pm 6\}_{k'}$ mode will be excited, though this excitation is weak (Fig. 2.8f). A similar discussion of the relevant selection rules recovers the response geometry evident in Figs 2.8(b) and 2.8(d).

We note that harmonics in the FV response on the left column of Fig. 2.8 show power at some degrees and orders that violate the above selection rules, and this supports our assertion that differences in the FV and NM largely reflect numerical errors in the former.

Group Coupling versus Full Coupling

To reduce computational complexity in studies of the Earth's seismic free oscillations, a method known as the quasi-degenerate or group coupling approximation may be employed (e.g., Resovsky & Ritzwoller, 1995). In this method, eigenmodes whose spherically-symmetric eigenfrequencies lie close together are grouped and assigned a fiducial frequency, ω_f, often taken to be the average of the eigenfrequencies. Then, rather than solving for all the eigenfrequencies of the system, as is required in the eigenvalue problems defined by eqs (2.46) and (2.47) (i.e., the full coupling calculation), first-order perturbations to the fiducial frequencies, $\delta\omega$, are found. This approach reduces the quadratic eigenvalue problem (eqs 2.46, 2.47), which involves one large, full coupling matrix, to an ordinary eigenvalue problem for each grouping of modes, and thus it involves matrices of much smaller dimension (Dahlen & Tromp, 1998). Solutions to the latter yield the perturbations $\delta\omega$.

The assumption inherent to group coupling is that within a group $\delta\omega \ll \omega_f$. Although group coupling has been used in seismic applications in the past, the accuracy of the method has been challenged (Deuss & Woodhouse, 2001). To consider the relative accuracy of these methods in the case of the body tide problem, we compare predictions generated using full and group coupling for an Earth model with aspherical structure. In particular, we impose density and elastic structure in the mantle by scaling shear wave velocity model S20RTS (Ritsema et al., 1999) using eqs (2.91)–(2.93). We calculate δs_r by applying the same tidal potential as in previous tests (see Section 2.3.2). Table 2.2 lists the 6 groups of modes adopted for the group coupling calculation and also the complete set of 30 modes in the full coupling case. There are clearly far fewer modes included in the former due to the restrictions on the frequency range of each group. Note that each of these groups must contain at least one ${}_n\mathcal{S}_2$ mode in order to be excited by the tidal force.

Figs 2.9(a,b) provide maps of the difference in radial displacement (δs_r) between the aspherical and reference (spherically-symmetric) cases for both group (left) and full (right) coupling applications of the NM methodology. The predictions are markedly different, with the group coupling case showing little excitation of modes for $\ell \neq 2$ (see Fig. 2.9c,d). In the full coupling calculation, the dominant coupling produces large $S_{4,4}$ and $S_{2,0}$ signals in the displacement response. All other signals associated with coupling are at least an order of magnitude lower (Fig. 2.9d).

There is a fundamental difference between the nature of an earthquake source, involving an impulse forcing with a variety of spatial and temporal harmonics exciting a wide range of eigenmodes, versus a tidal source, a body force that acts through the whole Earth within narrow frequency bands and a single spatial wavelength. This diffference has clear implications for mode coupling and we

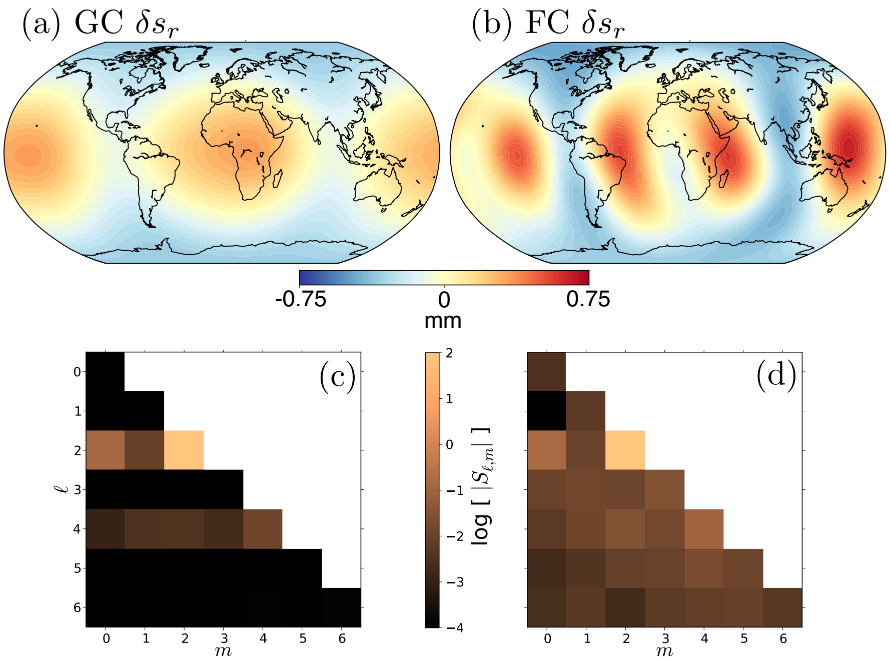

Figure 2.9: The radial displacement of an elastic, aspherical Earth with imposed S20RTS (Ritsema et al., 1999) structure (with scaling factors given by eqs 2.91–2.93) in response to a $c_{2\,2}$ body force. (a), (b): The residual field, δs_r, using the group and the full coupling method, respectively. (c), (d): The spherical harmonic decomposition of the total radial displacement response computed using the group and full coupling methods, respectively.

conclude, on the basis of Fig. 2.9, that full coupling must always be applied when a normal mode methodology is adopted to calculate the impact of aspherical Earth structure on the Earth's body tide response.

ROTATION

Earth rotation will perturb the body tide response relative to a non-rotating model, and lead to a response at degrees $\ell \neq 2$ (Wahr, 1981b; Dehant, 1987; Wang, 1994). Within the NM method, this perturbation arises through coupling of modes and is accounted for by two aspects of the underlying theory: first, by the presence of the Coriolis matrix, $\mathbf{W}$ (eq. 2.44); and second, by components of the matrices $\mathbf{T}$ and $\mathbf{V}'$ that account for both the ellipticity of the Earth, which is an aspherical perturbation in Earth structure of $\{2, 0\}$ geometry, and the centrifugal potential energy (Dahlen, 1968).

The impact of rotation is characterized by a specific splitting and coupling of modes. In the case of an elastic Earth with no aspherical structure other than a rotation-induced ellipticity, a mode k will couple with: (i) a mode of like ℓ and m; (ii) a mode k' where $m' = m$ and $\ell' = \ell \pm 2$; and (iii) a toroidal mode of $\ell' = \ell \pm 1$ (due to the Coriolis operator; this final coupling is very minor and we do not discuss it further). For a semi-diurnal forcing, this coupling would lead to a response, as expressed by the spherical harmonic expansion (eq. 2.83), that has only non-zero components of $S_{2,2}$ and $S_{4,2}$. We have found that the perturbations from the reference (non-rotating) case for components $S_{2,2}$ and $S_{4,2}$ are $+0.05\%$ and -0.01%, respectively, of the reference value, $S^0_{2,2}$.

2.4 SUMMARY

We have derived a theoretical framework for predicting the semi-diurnal and long-period body tides on an aspherical, rotating and anelastic Earth that is based on seismic free oscillation theory. As we have discussed, in the most general form the problem involves a non-Hermitian operator which can be solved by the introducing a dual space (Lognonné, 1991). We have also described a generalized normal mode treatment of the impact of anelasticity on the body tide response. While based on free oscillation theory, our treatment is distinct from the approach used in seismic applications. It is also distinct from the theory developed by Wahr & Bergen (1986) to incorporate anelastic effects. In the context of our theory, accurately capturing the impact of anelastic effects requires that relaxation modes outside the usual seismic band be included in the normal mode summation.

We have presented some simple numerical calculations that demonstrate that classical Love number results (Farrell, 1972) for a SNREI Earth can be reproduced using the normal mode framework. These calculations highlight the physics of the tidal response as well as its sensitivity to Earth structure, as reflected by sensitivity kernels.

We have also outlined a perturbation scheme, taken from the seismic free oscillation literature, to compute the impact on body tide displacements of lateral variations in Earth structure. We performed a series of tests using the NM methodology and benchmarked the results against calculations based on a fully numerical, finite-volume methodology (Latychev et al., 2009). Our main conclusion is that the impact of aspherical structure on the body tide response must be based on a full coupling of eigenmodes rather than group coupling, which is in agreement with previous normal mode studies (Deuss & Woodhouse, 2001). While full coupling is computationally expensive in the seismic problem, the limited spectral range of the tidal forcing and response makes it easily tractable for body tide calculations and thus the implementation of full coupling does not pose any practical difficulty. Differences between predictions based on the NM and FV methodologies were significantly below the percent level, and it is likely that these differences originate from numerical inaccuracies in the FV scheme.

In the next chapter, we will elaborate on our new normal mode treatment of anelasticity and discuss the implications of the method for interpreting measurements of anelastic effects on body tides (e.g., phase lags) and for inferring Earth structure. Ultimately, our goal is to combine our generalized treatment of semi-diurnal and long-period body tides on an aspherical, rotating and anelastic Earth, with space-geodetic and long-period seismic measurements, to perform the first global tomographic tidal analysis of the Earth's long-wavelength elastic and density structure. This is the subject of Chapter 4.

3

Anelasticity Across Seismic to Tidal Time-scales: a Self-Consistent Approach

> *You are off on a winding and difficult road, which you conceive to be wide and straight, an Autobahn you can travel at your ease.*
>
> –T. Pynchon

3.1 INTRODUCTION

The search for an accurate and complete understanding of the frequency domain response of the Earth to an applied forcing is of fundamental importance in efforts to model a wide range of dynamical processes, including seismic wave propagation, ocean (loading) and body tides, polar motion and glacial isostatic adjustment. Dissipation of energy varies with frequency and, from a macro-

---

A version of this chapter was published with Ulrich Faul, Jerry X. Mitrovica, David Al-Attar, Jeroen Tromp, and Gordana Garapić[5] in *Geophysical Journal International*, vol. 208(1), p. 368-384, 2016.

scopic viewpoint, this variability is largely a reflection of the frequency dependence of the viscosity of Earth's bulk materials. In this study, we focus on the anelastic (small strain) portion of Earth's rheological response from long-period seismic to tidal time-scales, and we treat this response as time dependent, but completely recoverable (i.e., we do not consider the possibility of a purely viscous component to the response).

Several approaches have been used to investigate how dissipation arises across these time-scales. For example, experimental studies recreate relevant stress and temperature conditions in samples across a specified frequency range and focus on grain-scale processes (see, e.g., Faul & Jackson, 2015). These studies indicate that Earth materials exhibit the so-called "high-temperature background" behavior, whereby attenuation (which is to be interpreted as synonymous with dissipation) may be characterized by a power-law frequency dependence. Materials that exhibit such behavior include metals (e.g., Rivière, 2001), ceramics (e.g., MgO, Barnhoorn et al., 2007) and silicates (e.g., Jackson, 1993; Gribb & Cooper, 1998). Microphysical models of grain-scale processes predict a grain-size dependence of dissipation due to elastically and diffusionally accommodated grain-boundary sliding (e.g., Raj & Ashby, 1971; Raj, 1975; Morris & Jackson, 2009; Lee et al., 2011). These models predict that with decreasing frequency the mildly frequency-dependent high temperature background or absorption band behaviour is followed seamlessly by a transition to viscous behavior. The frequency and grain-size dependence predicted by these models has been observed experimentally in olivine (Jackson et al., 2002; Jackson & Faul, 2010).

Direct observations of Earth's response to external forcings have also been used to constrain the frequency dependence of dissipation. For example, measurements of the Earth's response to earthquakes, including body waves, surface waves, and normal mode excitation, have all yielded estimates of the Earth's attenuation (or Q^{-1} where Q is the quality factor) structure, though these estimates are generally characterized by significant uncertainty (Resovsky et al., 2005). In regard to seismic frequencies, models adopted within the literature include an absorption band in which Q^{-1} is assumed to be either constant with respect to frequency (Kanamori & Anderson, 1977) or characterized by a power law dependence (Anderson & Minster, 1979; Shito et al., 2004; Lekić et al., 2009). Observations of geodynamic processes with longer periods, such as body tides and the Chandler Wobble, have extended existing constraints on dissipation to include time-scales of years and decades (e.g., Anderson & Minster, 1979; Ray et al., 2001; Benjamin et al., 2006), although these observations are also characterized by large uncertainty.

Taken together, existing observational constraints suggest that dissipation increases with the period of the forcing, though the exponent of the frequency dependence and the frequency of the onset of the absorption band remain poorly known. This is, in part, due to the large observational uncertainties noted above (Resovsky et al., 2005; Benjamin et al., 2006), but a more fundamental issue is also at play. In particular, a series of assumptions and approximations commonly adopted in analyses of anelastic behaviour at long (i.e., tidal and Chandler wobble) periods (Wahr & Bergen, 1986) are not consistent with the treatment of dissipation in the seismic band (Lau et al., 2015) and obscure differences between intrinsic (material) and apparent (observed) dissipation. A major goal of this chapter is to highlight these issues and explore, in detail, inaccuracies introduced by adopting the traditional theory for modeling the anelastic response of the Earth in the tidal band. As we will demonstrate, these inaccuracies include significant biases introduced in previous estimates of intrinsic dissipation across tidal time-scales and in extrapolating the frequency dependence of dissipation to longer periods.

A rigorous methodology for mapping between sample (i.e., laboratory) scale and planetary-scale information, and for bridging between observations at seismic and tidal time-scales requires a generalized, self-consistent theoretical treatment of anelasticity. In this paper, we apply, for this purpose, the generalized, normal mode theory of Lau et al. (2015) and a variant of this method (the direct solution method) that has advantages in the practical application of the theory. In the next section we begin by summarizing the relevant aspects of this new theory and the traditional approach for modeling anelastic effects in the tidal band (Wahr & Bergen, 1986).

Finally, although we focus here on applications to geophysics, the methodology we develop is equally relevant to studies of other terrestrial planets. We return to this point in the concluding section.

3.2 THEORETICAL BACKGROUND

Gilbert (1971) highlighted the fundamental connection between the deformation of the Earth in response to earthquakes and luni-solar tidal forcing by pointing out that the normal modes of the Earth system relevant to seismic and tidal applications are precisely the same. In the years subsequent to his seminal study, insights from a series of important developments in seismic free oscillation theory (e.g., Dahlen, 1968; Gilbert, 1971; Woodhouse & Dahlen, 1978; Woodhouse, 1980; Park & Gilbert, 1986) were incorporated into analyses of Earth's body tides and other longer period geodynamic processes (e.g., Smith & Dahlen, 1981; Wahr, 1981a,b; Wahr & Bergen, 1986). However, the latter effort did not always mirror the former, as is clear by comparing seismic normal mode treatments and body tide studies of the impact of rotation (compare Dahlen (1968) with Wahr (1981b), Dehant (1987), and Wang (1994)) and asphericity (compare Woodhouse (1980) with Dehant et al. (1999), Métivier & Conrad (2008), Latychev et al. (2009), and Qin et al. (2014)). Moreover, in considering anelastic effects, the standard perturbation approach adopted in the body tide literature (Wahr & Bergen, 1986) predates the seismic normal mode theories of Lognonné (1991) and Tromp & Dahlen (1990), who derived generalized expressions for the orthogonality of eigenfunctions appropriate to this case.

Lau et al. (2015), motivated by the availability of progressively more accurate and extensive space-geodetic measurements of body tide deformation (e.g., Yuan & Chao, 2012; Yuan et al., 2013), derived a generalized normal mode treatment of body tides using the full theoretical machinery of modern seismic free oscillation theory and made appropriate extensions relevant for the tidal application. We begin by reviewing this theory which hereafter we will term the 'extended normal mode' (ENM) theory.

3.2.1 PARAMETERIZING ANELASTICITY

We begin by introducing the frequency-domain fourth-order tensor $\mathbf{\Lambda}$, which relates the deformation to the incremental first Piola-Kirchoff stress tensor, $\mathbf{T}^{\mathrm{PK1}}$, via the following expression:

$$\mathbf{T}^{\mathrm{PK1}}(\omega) = \mathbf{\Lambda}(\omega) : \nabla \mathbf{s}(\omega) \ . \tag{3.1}$$

Here, ω is the (complex) frequency and $\mathbf{s}$ is the displacement, ∇ is the del-operator (and thus $\nabla \mathbf{s}$ represents the full deformation tensor) and the double-dot operation represents $\mathbf{A} : \mathbf{B} = \mathrm{tr}(\mathbf{A}^{\mathrm{T}} \cdot \mathbf{B})$. The Fourier transform convention for a function f used throughout this study is

$$\mathcal{F}[f(t)] \equiv \tilde{f}(\omega) = \int_0^{\infty} f(t)\, e^{-i\omega t}\, \mathrm{d}t \ , \tag{3.2}$$

$$\mathcal{F}^{-1}[\tilde{f}(\omega)] = f(t) = \frac{1}{2\pi} \int_{-\infty}^{+\infty} \tilde{f}(\omega)\, e^{i\omega t}\, \mathrm{d}\omega \ . \tag{3.3}$$

$\mathbf{\Lambda}$ must be analytic in the lower half of the complex plane (Dahlen & Tromp, 1998) and additionally adhere to the following relations:

$$\mathbf{\Lambda}^{*}(\omega) = \mathbf{\Lambda}(-\omega^{*}) \ , \tag{3.4}$$

$$\Lambda_{ijmn}(\omega) = \Lambda_{mnij}(\omega) \ , \tag{3.5}$$

where eq. (3.4) must be satisfied in order to obtain a real-valued $\mathbf{\Lambda}$ in the time domain (O'Connell & Budiansky, 1978) and the symmetry relation (3.5) is commonly assumed to hold within viscoelasticity. For a discussion of the physical significance of eq. (3.5) see Day (1971a,b). The scalar components of $\mathbf{\Lambda}$ represent specific moduli. For an isotropic medium, there are two such moduli: the shear modulus and the bulk modulus, μ and κ, respectively. In this specific case, the elements of $\mathbf{\Lambda}$ are given by:

$$\begin{aligned}\Lambda_{ijmn}(\omega) = &\left[\kappa(\omega) - \frac{2}{3}\mu(\omega)\right]\delta_{ij}\delta_{mn} + \mu(\omega)\left[\delta_{im}\delta_{jn} + \delta_{in}\delta_{jm}\right] \\ &+ \frac{1}{2}\left({T^0}_{ij}\delta_{mn} + {T^0}_{mn}\delta_{ij} + {T^0}_{im}\delta_{jn} - {T^0}_{jm}\delta_{in}\right. \\ &\left. - {T^0}_{in}\delta_{jm} - {T^0}_{jn}\delta_{jm} - {T^0}_{jn}\delta_{im}\right) \end{aligned} \tag{3.6}$$

(eq. 3.146 and Table 3.2 in Dahlen & Tromp, 1998). Here, δ_{ij} is the Kronecker delta and $\mathbf{T}^0$ is the initial stress tensor. Chapters 2–3 of Dahlen & Tromp (1998) provide a comprehensive review of these relations.

For an elastic medium, $\mathbf{\Lambda}$ is purely real and independent of ω. (In the following, and if necessary for clarity, we will denote any parameter, X, associated with the elastic problem as $\bar{X}$.) If we denote a general scalar elastic modulus by $\bar{M}$, then once anelasticity is introduced

$$\bar{M} \rightarrow M(\omega) = \bar{M} + \delta M(\omega) \ , \tag{3.7}$$

where δM is complex and a function of the complex frequency, ω, and thus $M(\omega) = M_1(\omega) + iM_2(\omega)$ where $i = \sqrt{-1}$. We do not discuss the specific frequency dependence of $M(\omega)$ here, though this is an active area of research (e.g., Gribb & Cooper, 1998; Jackson & Faul, 2010; McCarthy et al., 2011; Bellis & Holtzman, 2014). It has been shown experimentally for materials exhibiting absorption band behaviour that $M_1(\omega)$ will decrease with decreasing frequency and $M_2(\omega)$ will increase (e.g., Faul & Jackson, 2015). The following ratio

$$Q(\omega) \equiv \frac{M_1(\omega)}{M_2(\omega)} \tag{3.8}$$

is known as the quality factor of the modulus M (Chapter 1.3 in Nowick & Berry, 1972), where $\arcsin[Q^{-1}(\omega)]$ describes the lag angle between the stress and strain acting on M, and is also known as the loss angle. We note that in many applications where $Q \gg 1$ (and thus the lag angle is small), this angle is often listed as $\arctan[Q^{-1}(\omega)]$. For a more complete discussion of this issue, the reader is referred to Efroimsky (2012, 2013). In the present study, which is limited to the high Q regime, we will adopt the approximate form to aid comparisons to the literature. We emphasize, however, that our theory does not require such an approximation. Q may also be interpreted in terms of energy loss where Q^{-1} represents the fractional average energy dissipated per cycle and so we may also write

$$Q^{-1} \equiv \frac{\oint \dot{E}\,\mathrm{d}t}{2\omega \oint E\,\mathrm{d}t} , \tag{3.9}$$

where E is the elastic energy density (Chapter 6; 1.6 in Dahlen & Tromp, 1998). The numerator and denominator represent the dissipated and stored energies per cycle, respectively. The interpretation of Q^{-1} has caused confusion in the past, as outlined by O'Connell & Budiansky (1978), and in this chapter we will highlight some continuing misinterpretations found within the tidal literature of Q—a key parameter that is ubiquitous in discussions of anelasticity—in Section 3.3.2.

To summarize, all information concerning the anelastic properties of the medium is stored within $\mathbf{\Lambda}(\omega)$. How $\mathbf{\Lambda}(\omega)$ fits into the general framework of long-period seismic and body tide problems is addressed next.

3.2.2 An Extended Normal Mode (ENM) Theory

Consider the governing equation for a self-gravitating, non-rotating, elastic Earth, forced by some arbitary body force, $\tilde{\mathbf{f}}$. The frequency-domain equation in this case is given by

$$\bar{\mathcal{H}}(\mathbf{r})\mathbf{s}(\mathbf{r};\omega) - \omega^2\mathbf{s}(\mathbf{r};\omega) = \tilde{\mathbf{f}}(\mathbf{r};\omega) , \tag{3.10}$$

where

$$\rho(\mathbf{r})\,\bar{\mathcal{H}}(\mathbf{r})\mathbf{s}(\mathbf{r};\omega) = \rho(\mathbf{r})\,\nabla\phi(\mathbf{r};\omega) + \rho(\mathbf{r})\,\mathbf{s}(\mathbf{r};\omega)\cdot\nabla\nabla(\Phi(\mathbf{r})) - \nabla\cdot\left[\bar{\mathbf{\Lambda}}(\mathbf{r}) : \nabla\mathbf{s}(\mathbf{r};\omega)\right] \; . \tag{3.11}$$

Here, $\mathbf{r}$ is the position vector whose origin is at the center of mass (we will use this to denote radius, r, co-latitude, θ, and east-longitude, ψ), ρ is the mass density, and the following gravitational quantities,

$$\Phi(\mathbf{r}) = \; - G\int_V \frac{\rho(\mathbf{r}')}{||\mathbf{r}-\mathbf{r}'||}\,\mathrm{d}V' \; , \tag{3.12}$$

$$\phi(\mathbf{r};\omega) = \; - G\int_V \frac{\rho(\mathbf{r}')\,\mathbf{s}(\mathbf{r}',\omega)\cdot(\mathbf{r}-\mathbf{r}')}{||\mathbf{r}-\mathbf{r}'||^3}\,\mathrm{d}V' \; , \tag{3.13}$$

are the equilibrium gravitational potential and incremental gravitational potential, respectively. In these expressions, G is the universal gravitational constant and V is a volume that encompasses the Earth. We have omitted the impact of rotation on these expressions in order to simplify discussion, however the theory described in Lau et al. (2015) is able to incorporate this effect. Eq. (3.10) is solved along with the following traction-free boundary condition:

$$\hat{\mathbf{n}}\cdot\left[\bar{\mathbf{\Lambda}}(\mathbf{r}) : \nabla\mathbf{s}(\mathbf{r};\omega)\right] = \mathbf{0} \; , \;\; \mathbf{r}\in\Omega \; , \tag{3.14}$$

where Ω is the surface of the Earth with unit outward normal $\hat{\mathbf{n}}$. When anelasticity is introduced $\bar{\mathbf{\Lambda}}(\mathbf{r}) \to \mathbf{\Lambda}(\mathbf{r};\omega)$ and the governing equation (3.10) becomes

$$\mathcal{H}(\mathbf{r};\omega)\mathbf{s}(\mathbf{r};\omega) - \omega^2\mathbf{s}(\mathbf{r};\omega) = \tilde{\mathbf{f}}(\mathbf{r};\omega) \; . \tag{3.15}$$

In the following, we will treat any dependency on $\mathbf{r}$ and ω as implicit unless the clarity of meaning demands otherwise. The homogeneous version of eq. (3.15) is

$$\mathcal{H}(\omega_k)\mathbf{s}_k - {\omega_k}^2\mathbf{s}_k = \mathbf{0} \ , \tag{3.16}$$

where $\mathbf{s}_k$ and ω_k are the eigenfunctions and eigenfrequencies, respectively, for which there exists a non-trivial solution to eq. (3.16). (Note the non-linearity in the eigenvalue parameter.) In Lau et al. (2015) the duality product first derived by Lognonné (1991) was incorporated into the theory. In this paper, we choose to instead adopt the inner product to aid the comparison between the ENM theory and the traditional normal mode theory of Wahr & Bergen (1986). (Yang & Tromp (2015) showed that the duality and inner product lead to equivalent results.) Following Yang & Tromp (2015), we define the inner product as

$$\langle \mathbf{s}_k, \mathbf{s}_{k'} \rangle = \int_V \rho \, {\mathbf{s}_k}^* \cdot \mathbf{s}_{k'} \, \mathrm{d}V \ , \tag{3.17}$$

which has the following symmetries:

$$\langle \mathbf{s}_k, \mathbf{s}_{k'} \rangle = \langle \mathbf{s}_{k'}, \mathbf{s}_k \rangle^* \ , \tag{3.18}$$

$$\langle \mathbf{s}_k, \mathcal{H}(\omega_{k'})\mathbf{s}_{k'} \rangle = \langle \mathcal{H}^*(\omega_k)\mathbf{s}_k, \mathbf{s}_{k'} \rangle = \langle \mathbf{s}_{k'}, \mathcal{H}^*(\omega_k)\mathbf{s}_k \rangle^* \ . \tag{3.19}$$

The eigenfunctions are normalized as follows

$$\langle \mathbf{s}_k, \mathbf{s}_{k'} \rangle - \tfrac{1}{2}\omega_k^{-1} \langle \mathbf{s}_k, \partial_\omega \mathcal{H}(\omega_{k'})\mathbf{s}_{k'} \rangle = \delta_{kk'} \ . \tag{3.20}$$

Thus, eq. (3.16) has the following symmetry

$$\mathcal{H}(-\omega^*) = \mathcal{H}^*(\omega) \tag{3.21}$$

and as such, one finds that if and only if ω_k and $\mathbf{s}_k$ are eigenmodes of eq. (3.16), then so too are $-\omega^*$ and $\mathbf{s}^*$ (Lognonné, 1991).

After finding the eigenmodes, any solution $\mathbf{s}$ may be formed by the appropriate weighted sum of eigenfunctions $\mathbf{s}_k$ with time dependence given by ω_k. In normal mode seismology a Green function for such a system, that is the solution to a point force (subject to the appropriate initial and boundary conditions), is given by (Lognonné, 1991):

$$\mathbf{G}(\mathbf{r}, \mathbf{r}'; t) = \mathrm{Re} \sum_k \frac{1}{2i\omega_k} \mathbf{s}_k(\mathbf{r}) \mathbf{s}_k{}^*(\mathbf{r}') \exp(i\omega_k t) \ . \tag{3.22}$$

The function $\mathbf{G}$ is simplified in the normal mode seismology application due to the symmetry of eigenfrequencies ω_k and $-\omega_k{}^*$ such that $\mathbf{G}$ is often quoted as (e.g., Dahlen & Tromp, 1998):

$$\mathbf{G}(\mathbf{r}, \mathbf{r}'; t) = \mathrm{Re} \sum_{\substack{k \\ \mathrm{Re}\{\omega_k\}>0}} \frac{1}{i\omega_k} \mathbf{s}_k(\mathbf{r}) \mathbf{s}_k{}^*(\mathbf{r}') \exp(i\omega_k t) \ , \tag{3.23}$$

where the summation includes only eigenfrequencies where $\mathrm{Re}\{\omega_k\} > 0$. The simplification implied by eq. (3.23) cannot be used in the tidal approach due to the existence of "relaxation modes" which will be discussed in Section 3.2.2 (or see Lau et al., 2015). $\mathbf{G}$ describes the time-domain response to an impulse force and convolving $\mathbf{G}$ with a time-domain force, $\mathbf{f}$, yields the solution, $\mathbf{s}$,

$$\begin{aligned}\mathbf{s}(\mathbf{r};t) = &\int_{t_0}^{t}\int_{V}\mathbf{G}(\mathbf{r},\mathbf{r}';t-t')\cdot\mathbf{f}(\mathbf{r}',t')\,\mathrm{d}V'\mathrm{d}t' \\ &+\int_{t_0}^{t}\int_{\Omega}\mathbf{G}(\mathbf{r},\mathbf{r}';t-t')\cdot\tau(\mathbf{r}',t')\,\mathrm{d}\Omega'\mathrm{d}t' \\ &+\int_{t_0}^{t}\int_{V}\mathbf{B}(\mathbf{r},\mathbf{r}';t-t')\cdot\mathbf{f}(\mathbf{r}',t')\,\mathrm{d}V'\mathrm{d}t' \\ &+\int_{t_0}^{t}\int_{\Omega}\mathbf{B}(\mathbf{r},\mathbf{r}';t-t')\cdot\tau(\mathbf{r}',t')\,\mathrm{d}\Omega'\mathrm{d}t'\ ,\end{aligned}\tag{3.24}$$

where t_0 is the time of initiation of forcing $\mathbf{f}$. The expression (3.24) includes an additional traction, τ, which generalizes our application to include any surface force. $\mathbf{B}(\mathbf{r};t)$ is the contribution due to singularities of the frequency domain solution other than isolated simple poles, which could potentially include features like branch cuts or other non-modal singularities. $\mathbf{B}$ arises due to the specific form we will adopt for $\mathbf{\Lambda}(\omega)$ (see Section 3.2.2). The existence of these non-modal singularities within the complex plane of ω greatly complicates the evaluation of eq. (3.24).

We will consider the form of $\mathbf{s}(\mathbf{r};t)$ for two cases: the long-period response to an earthquake with body force $\mathbf{f}$ and traction τ; and the body tide response to the forcing $\rho\nabla\Psi$ (where Ψ is the tidal potential). In the earthquake problem, this form is written as

$$\begin{aligned}\mathbf{s}(\mathbf{r};t) = &\int_{t_0}^{t}\int_{V}\mathbf{G}(\mathbf{r},\mathbf{r}';t-t')\cdot\mathbf{f}(\mathbf{r}',t')\,\mathrm{d}V'\mathrm{d}t' \\ &+\int_{t_0}^{t}\int_{\Omega}\mathbf{G}(\mathbf{r},\mathbf{r}';t-t')\cdot\tau(\mathbf{r}',t')\,\mathrm{d}\Omega'\mathrm{d}t'\ ,\end{aligned}\tag{3.25}$$

where $\int_{t_0}^{t}\int_{V}\mathbf{B}(\mathbf{r},\mathbf{r}';t-t')\cdot\mathbf{f}(\mathbf{r}',t')\mathrm{d}V'\mathrm{d}t' \approx 0$ and $\int_{t_0}^{t}\int_{\Omega}\mathbf{B}(\mathbf{r},\mathbf{r}';t-t')\cdot\tau(\mathbf{r}',t')\mathrm{d}\Omega'\mathrm{d}t' \approx 0$. These approximations are appropriate for many seismic applications since, for plausible forms of $\mathbf{\Lambda}$, seismic waves do not occur at very low frequencies and thus do not excite the non-modal singularities associated with $\mathbf{B}$ to an appreciable extent. However, $\mathbf{B}$ is likely to be relevant for post-seismic deformation which occurs at lower frequencies than co-seismic deformation. In contrast, for the body tide, the appropriate expression is

$$\begin{aligned} \mathbf{s}(\mathbf{r};t) = &\int_{t_0}^{t}\int_V \rho(\mathbf{r}')\,\mathbf{G}(\mathbf{r},\mathbf{r}';t-t')\cdot\nabla\Psi(\mathbf{r}',t')\,\mathrm{d}V'\mathrm{d}t' \\ &+\int_{t_0}^{t}\int_V \rho(\mathbf{r}')\,\mathbf{B}(\mathbf{r},\mathbf{r}';t-t')\cdot\nabla\Psi(\mathbf{r}',t')\,\mathrm{d}V'\mathrm{d}t'\ , \end{aligned} \tag{3.26}$$

where one may include in (3.26) the surface forcing in the case of ocean tidal loading by including the terms on the second and fourth lines of eq. (3.24) and the appropriate expression for τ. In this case, realistic periodicities of the exciting potential $\nabla\Psi$ are long enough for the contribution from $\mathbf{B}$ to be relevant.

For the seismic problem, the full time dependence of the response is of interest, but for the tidal problem the steady-state solution is required (that is, the transient component of the solution to eq. (3.26) associated with the initiation of forcing may be ignored). If we assume $\Psi(\mathbf{r};t)$ has the form of a single harmonic we may write:

$$\nabla\Psi_{\ell m}(\mathbf{r};t) = c_{\ell m}\exp[i\omega_T t]\,\frac{r^{\ell-1}}{a^{\ell}}\left[\ell\, Y_{\ell m}(\theta,\psi)\hat{\mathbf{r}} + \sqrt{\ell(\ell+1)}\nabla_1 Y_{\ell m}(\theta,\psi)\right]\ , \tag{3.27}$$

where a is the radius of the Earth, ω_T is the (real) tidal frequency, and $c_{\ell m}$ is a factor that accounts for the orbital properties of the forcing body which produces $\Psi_{\ell m}$. $Y_{\ell m}$ is the spherical harmonic of degree ℓ and order m following the normalization of Edmonds (1960). ∇_1 represents the projection of the gradient operator in the θ and ψ directions. In reality there are many forcing harmonics but the linearity of the problem allows the suite of tidal harmonics to be trivially superimposed.

At this point we depart from the treatment of a generalized Earth model to focus on the specialized case of a spherically-symmetric Earth model. We do this to take advantage of analytic results that will be useful in the illustrative case studies described in Section 3.3. The theory of Lau et al.

(2015) may be used to incorporate aspherical structure into any of those case studies. For spherically symmetric (and self-gravitating) Earth models, the forcing given by eq. (3.27) will excite only spheroidal eigenmodes, $\mathbf{s}_k$, for which the eigenfunctions for these may be expressed as

$$ {}_n\mathbf{s}_{\ell m}(\mathbf{r}) = {}_nU_\ell(r) Y_{\ell m}(\theta, \psi)\hat{\mathbf{r}} + {}_nV_\ell(r) \frac{\nabla_1 Y_{\ell m}(\theta, \psi)}{\sqrt{\ell(\ell+1)}} \ . \tag{3.28} $$

The single index k is used to denote ℓ, m and the overtone number, n, of a mode. Note that we have dropped the m subscript for eigenfunctions ${}_nU_\ell$ and ${}_nV_\ell$ as spherical symmetry results in degenerate eigenmodes in m. When necessary, ℓ, m and n will be specified separately.

Thus, by substituting eqs (3.27) and (3.28) into eq. (3.26), and taking the limit $t_0 \to -\infty$, the steady-state solution is given by

$$ \begin{aligned} \mathbf{s}(\mathbf{r}, t) = &- \sum_n \frac{{}_n\mathbf{s}_{\ell m}(\mathbf{r})}{2{}_n\omega_\ell{}^2} \int_V \rho(r') {}_n\mathbf{s}_{\ell m}{}^*(\mathbf{r}') \cdot \nabla \Psi_{\ell m}(\mathbf{r}; t) \, \mathrm{d}V' \\ &- \int_{-\infty}^{t} \rho(r') \, \mathbf{B}(\mathbf{r}, \mathbf{r}'; t - t') \cdot \nabla \Psi_{\ell m}(\mathbf{r}'; t') \, \mathrm{d}V' \mathrm{d}t' \ . \end{aligned} \tag{3.29} $$

After some algebra (which is detailed in Appendix A), one finds that

$$ \begin{aligned} &\sum_n {}_n\mathbf{s}_{\ell m}(\mathbf{r}) \int_V \rho(r') \, {}_n\mathbf{s}_{\ell m}{}^*(\mathbf{r}') \cdot \nabla \Psi_{\ell m}(\mathbf{r}; t) \, \mathrm{d}V' = \\ &\quad \Bigg\{ \sum_n {}_nU_\ell(r) \int_0^a \rho(r) \frac{r^{\ell+1}}{a^\ell} \left[\ell_n U_\ell(r) + \sqrt{\ell(\ell+1)}_n V_\ell(r) \right] \, \mathrm{d}r \ \Psi_{\ell m}(\mathbf{r}) \hat{\mathbf{r}} \\ &\quad + \sum_n \frac{{}_nV_\ell(r)}{\sqrt{\ell(\ell+1)}} \int_0^a \rho(r) \frac{r^{\ell+1}}{a^\ell} \left[\ell_n U_\ell(r) + \sqrt{\ell(\ell+1)}_n V_\ell \right] \, \mathrm{d}r \ \nabla_1 \Psi_{\ell m}(\mathbf{r}) \Bigg\} \exp[i\omega_T t] \ . \end{aligned} \tag{3.30} $$

This expression represents the excitation of spheroidal modes of degree ℓ by a tidal potential of the same degree, ℓ.

Eigenfrequencies on the Complex Plane

Complex eigenfrequencies incorporate two types of behavior: oscillation ($\mathrm{Re}\{\omega_k\}$) and relaxation ($\mathrm{Im}\{\omega_k\}$, where $\mathrm{Im}\{\omega_k\} > 0$). These behaviors may be represented on the complex plane of ω, where the set of ω_k are singularities of $\tilde{\mathbf{G}}(\mathbf{r}, \mathbf{r}'; \omega)$ (the Fourier transform of the Green tensor, $\mathbf{G}$). In seismic free oscillation theory, the eigenfrequencies lie just above the real line, i.e., $\mathrm{Im}\{\omega\} \ll \mathrm{Re}\{\omega\}$, and we will henceforth refer to these as 'dynamic modes'. Fig. 3.1(a) provides a schematic representation of the location of these dynamic modes on the ω-plane. Due to the symmetry property stated in Section 3.2.2, these eigenfrequencies are comprised of reflected pairs about the imaginary axis. In seismic normal mode calculations it is common to assume that these modes 'see' Earth structure at real eigenfrequencies, since the imaginary components are so small (Dahlen & Tromp, 1998). To incorporate the effects of anelasticity on the eigenfrequency, a perturbation theory is used that determines the deviation from the elastic eigenfrequency by taking into account the Q structure of the Earth. In general, we have

$$\omega_k \approx \bar{\omega}_k + \delta\omega_k \tag{3.31}$$

where $\delta\omega_k$ is the small complex perturbation moving $\bar{\omega}$ (an eigenfrequency computed for an elastic Earth) upward and laterally in Fig. 3.1(a). The real perturbation is due to dispersion (i.e., frequency dependence) and the imaginary perturbation is due to attenuation, both a consequence of introducing anelasticity. The summation within the expression for $\mathbf{G}(\mathbf{r}, \mathbf{r}'; t)$ for the time-domain Green tensor (eq. 3.22) can be equivalently expressed as an inversion of $\tilde{\mathbf{G}}(\mathbf{r}, \mathbf{r}'; \omega)$ based on Cauchy's residue theorem, where one assumes that singularities in the ω-plane are isolated simple poles (Al-Attar, 2007).

Lau et al. (2015) demonstrated that for the tidal problem additional contributions must be incorporated into the summation in eq. (3.22). These so-called 'relaxation' modes would be located

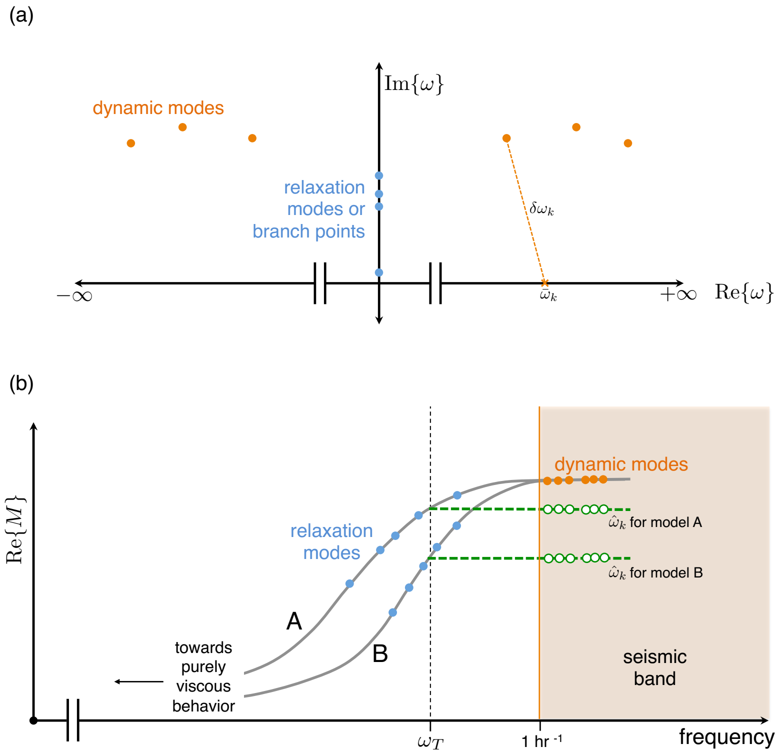
(a)
dynamic modes
$\mathrm{Im}\{\omega\}$
relaxation modes or branch points
$\delta\omega_k$
$-\infty$
$\bar{\omega}_k$
$+\infty$
$\mathrm{Re}\{\omega\}$
(b)
$\mathrm{Re}\{M\}$
dynamic modes
relaxation modes
$\hat{\omega}_k$ for model A
$\hat{\omega}_k$ for model B
A
B
towards purely viscous behavior
seismic band
ω_T
1 hr $^{-1}$
frequency

FIGURE 3.1: (a) A schematic diagram of the complex plane of ω. Orange circles mark the dynamic modes used in seismic normal mode theory. Blue circles mark the position of relaxation modes required, in addition to the dynamic modes, to accurately express the response to a tidal potential forcing. The orange dashed line labeled $\delta\omega_k$ is the complex perturbation from the elastic eigenfrequency, $\bar{\omega}_k$, due to anelastic effects. (b) A schematic diagram of the (real) modulus reduction for two materials, A and B, due to the introduction of anelasticity. As in (a), orange circles mark the dynamic modes and blue circles mark the (distinct) relaxation modes associated with the two models. Green circles illustrate the softening of the modulus assumed in the TNM treatment of anelastic effects on body tides (see text).

along the imaginary axis (i.e., $\mathrm{Re}\{\omega_k\} = 0$) with a magnitude that is much smaller than the imaginary part of the dynamic modes (Fig. 3.1a). Calculations in Lau et al. (2015) yielded a factor of ~ 10 difference in magnitudes, however this factor is highly model-dependent. These modes also exist in the seismic application but are, in most cases, of negligible importance in that frequency band. Relaxation modes relevant to the post-glacial rebound modes would exist at even smaller values along the positive imaginary axis (that is, relatively long relaxation times) provided that such behaviour is incorporated in $\mathbf{\Lambda}(\omega)$.

For models of $\mathbf{\Lambda}(\omega)$ proposed in the literature (e.g., Anderson & Minster, 1979; Benjamin et al., 2006; Faul & Jackson, 2015) branch points exist on the imaginary axis, and avoiding these features by taking branch cuts leads to the additional term involving the function $\mathbf{B}$ in eq. (3.26). The structure of $\mathbf{B}$ is often too complicated to express analytically and in the following sections we will depart from the ENM methodology and adopt a slight variant of this method that avoids these complexities. Nevertheless, the above derivation highlights: (1) the importance of augmenting the mode set that seismologists consider with relaxation modes to rigorously capture anelastic effects on the tidal response; and (2) the deep connection between the seismic and tidal applications of normal mode theory.

Direct Solution Method

The ENM treatment of body tides is useful for building physical intuition since eigenfrequencies reflect the characteristic time-scales of the response (in the case of both the dynamic and relaxation modes) while the sensitivity to internal structure is given by the depth-variation of eigenfunctions. However, as noted above, alternative methods for the tidal problem are necessary once more realistic models of $\mathbf{\Lambda}(\omega)$ are adopted. One such method, which in its practical implementation has close similarities to the ENM approach, is the so-called direct solution (DS) method which has been applied in seismological applications (e.g., Hara et al., 1993; Al-Attar, 2007; Al-Attar et al., 2012). Rather than finding the eigenmodes of the system (which by definition satisfy eq. 3.16), the DS method solves the equations governing the forced system (eq. 3.15).

Following Al-Attar (2007), we express the solution $\mathbf{s}$ as a superposition of an appropriate set of basis functions which, for example, may be eigenfunctions of an elastic Earth, $\bar{\mathbf{s}}$. That is, the solutions to the equation

$$\bar{\mathcal{H}}\bar{\mathbf{s}}_k - \bar{\omega}_k{}^2\bar{\mathbf{s}}_k = \mathbf{0}\ . \tag{3.32}$$

Then we seek appropriate values of β such that

$$\mathbf{s}(\mathbf{r};t) = \sum_k \beta_k(t)\bar{\mathbf{s}}_k(\mathbf{r}) \ . \tag{3.33}$$

Substituting eq. (3.33) into eq. (3.15) and using eq. (3.27) for the forcing term $\tilde{\mathbf{f}}$ yields

$$\sum_{k'} \left(\langle \bar{\mathbf{s}}_k, \mathcal{H}(\omega_T)\bar{\mathbf{s}}_{k'} \rangle - {\omega_T}^2 \langle \bar{\mathbf{s}}_k, \bar{\mathbf{s}}_{k'} \rangle \right) \beta_{k'} = -\langle \bar{\mathbf{s}}_k, \nabla\tilde{\Psi} \rangle \ , \tag{3.34}$$

where the normalization for an elastic earth is $\langle \bar{\mathbf{s}}_k, \bar{\mathbf{s}}_{k'} \rangle = \delta_{kk'}$. $\tilde{\Psi}$ is the frequency-domain forcing where $\Psi(t) = \tilde{\Psi}\exp[i\omega_T t]$. The second term $\langle \bar{\mathbf{s}}_k, \mathcal{H}(\omega_T)\bar{\mathbf{s}}_{k'} \rangle$ introduces anelastic coupling between the elastic eigenfunctions; that is, non-zero elements exist when $k \neq k'$. It may be shown that

$$\langle \bar{\mathbf{s}}_k, \mathcal{H}(\omega_T)\bar{\mathbf{s}}_{k'} \rangle = {\bar{\omega}_{k'}}^2 \delta_{k'k} + \langle \bar{\mathbf{s}}_k, \delta\mathcal{H}(\omega_T)\bar{\mathbf{s}}_{k'} \rangle \ , \tag{3.35}$$

where $\delta\mathcal{H}(\omega_T)$ acts to perturb $\bar{\mathcal{H}}$ (associated with the elastic problem) to the value required by the anelastic $\mathbf{\Lambda}(\omega_T)$. We showed in Chapter 2 that for aspherical Earth models full coupling is essential to accurately capture any prediction of tidal deformation (Lau et al., 2015). However, in the special case of spherically-symmetry we are considering here they demonstrated that self-coupling (which we define as including diagonal components only) provides an accurate approximation for sensible models of $\mathbf{\Lambda}(\omega_T)$. Adopting the self-coupling approximation, we find that

$$\beta_k = \frac{\langle \bar{\mathbf{s}}_k, \nabla\tilde{\Psi} \rangle}{{\bar{\omega}_k}^2 - {\omega_T}^2 + \langle \bar{\mathbf{s}}_k, \delta\mathcal{H}(\omega_T)\bar{\mathbf{s}}_k \rangle} \ . \tag{3.36}$$

Thus, the steady-state solution is given by

$$\mathbf{s}(t) = \sum_k \frac{\int_V \rho(\mathbf{r}')\, \bar{\mathbf{s}}_n{}^* \cdot \nabla\tilde{\Psi}\, \mathrm{d}V'}{[\bar{\omega}_k{}^2 + \varepsilon_k{}^2(\omega_T)] - \omega_T{}^2}\, \bar{\mathbf{s}}_k \exp[i\omega_T t] \ , \tag{3.37}$$

where we define $\varepsilon_k{}^2$ as

$$\varepsilon_k{}^2(\omega_T) \equiv \langle \bar{\mathbf{s}}_k, \delta\mathcal{H}(\omega_T)\bar{\mathbf{s}}_k \rangle \ . \tag{3.38}$$

The term $\varepsilon_k{}^2$ represents a complex perturbation to $\bar{\omega}_k{}^2$.

3.2.3 LOVE NUMBERS

For planetary-scale problems we may introduce tidal Love numbers (Love, 1911; Shida, 1912; Farrell, 1972), which provide a mapping between the forcing potential and response. This mapping is expressed in the spherical harmonic domain as

$$\mathbf{s}(\mathbf{r};t) = \sum_\ell \frac{h_\ell(r)}{g} \left[\hat{\mathbf{r}} \cdot \nabla\Psi_{\ell m}(\mathbf{r};t)\right] + \sum_\ell \frac{l_\ell(r)}{g} \left[\nabla_1 \Psi_{\ell m}(\mathbf{r};t)\right] \ , \tag{3.39}$$

where h is the Love number associated with radial displacement, s_r, and l is the Love number associated with tangential displacements, s_θ and s_ψ. Given the linear nature of this system we may derive expressions for h and l using results from Section 3.2.2. In the case of the ENM method, simple expressions for these parameters are not possible since we do not know the form of $\mathbf{B}$. In contrast, in the case of the DS method, combining eqs (3.30), (3.37) and (3.39) yields

$$h_\ell(a;\omega_T) = \frac{1}{g} \sum_n \frac{{}_n\bar{U}_\ell(a)}{[\bar{\omega}_n{}^2 + \varepsilon_n{}^2(\omega_T)] - \omega_T{}^2} \times \int_0^a \rho(r) \frac{r^{\ell+1}}{a^\ell} \left[\ell_n \bar{U}_\ell(r) + \sqrt{\ell(\ell+1)}\, {}_n\bar{V}_\ell(r)\right] \mathrm{d}r \tag{3.40}$$

and

$$l_\ell(a;\omega_T) = \frac{1}{g\sqrt{\ell(\ell+1)}} \sum_n \frac{{}_n\bar{V}_\ell(a)}{[\bar{\omega}_n{}^2 + \varepsilon_n{}^2(\omega_T)] - \omega_T{}^2} \times \int_0^a \rho(r) \frac{r^{\ell+1}}{a^\ell} \left[\ell_n \bar{U}_\ell(r) + \sqrt{\ell(\ell+1)}\,{}_n\bar{V}_\ell(r)\right] \mathrm{d}r \,, \tag{3.41}$$

where we have evaluated the Love numbers at Earth's surface, $r = a$ (this will be implicitly assumed hereafter), and we have made explicit the Love number dependence on the frequency of the forcing, ω_T. As discussed above, the spherical-symmetry in the adopted Earth model results in a $(2\ell + 1)$-degeneracy in the eigenmodes and thus the expressions (3.40–3.41) exhibit no m-dependence. However, the tidal forcing does include such dependence, and this is reflected in eq. (3.39). The anelastic character is captured in ε^2 which gives rise to complex $h(\omega_T)$ and $l(\omega_T)$ values. Re$\{h(\omega_T)\}$ represents the in-phase response and Im$\{h(\omega_T)\}$ represents the out-of-phase response, relative to the forcing potential. The same is true for $l(\omega_T)$. Wahr (1981a) showed that the Love numbers may be found by the appropriate superposition of the normal modes. However, in treating anelasticity, Wahr & Bergen (1986) introduced approximations that yielded expressions for the complex Love numbers that do not match those in eqs (3.40–3.41).

3.2.4 THE TRADITIONAL NORMAL MODE (TNM) THEORY

The most widely used theory to predict the effects of anelasticity on the body tide was formulated by Wahr & Bergen (1986), the last of a series of canonical studies covering the effects on body tides of rotation, free-core nutation and anelasticity (Wahr, 1981a,b; Wahr & Bergen, 1986, respectively). We will hereafter refer to their approach as the 'traditional normal mode' (TNM) theory. The TNM theory assumes that anelasticity perturbs existing elastic modes but does not introduce new modes, so that

$$\bar{\omega}_k \to \bar{\omega}_k + \delta\hat{\omega}_k \ , \tag{3.42}$$

where $\delta\hat{\omega}_k$ is a real number. This perturbation, $\delta\hat{\omega}$, is found by solving the following system:

$$\mathrm{Re}\{\mathcal{H}(\omega_T)\}\hat{\mathbf{s}}_k - \hat{\omega}_k{}^2\hat{\mathbf{s}}_k = \mathbf{0} \ , \tag{3.43}$$

where $\mathcal{H}(\omega_T)$ is fixed to the forcing frequency of interest, ω_T, and hence $\hat{\omega}_k = \bar{\omega}_k + \delta\hat{\omega}_k$. In this case, $\mathcal{H}$ is no longer a function of frequency and $[\hat{\omega}_k{}^2, \hat{\mathbf{s}}_k]$ are interpreted as eigenfrequency-eigenfunction pairs.

Strictly speaking, $\hat{\mathbf{s}}_k$ and $\hat{\omega}_k$ are not eigenmodes of a frequency-dependent Earth. True eigenmodes are computed by solving eq. (3.16); that is, eigenmodes 'see' the Earth at their eigenfrequency, $\mathcal{H} = \mathcal{H}(\omega_k)$. Moreover, eq. (3.16) involves $\mathcal{H}$, not just its real part, and thus admits the possibility of relaxation behavior (and relaxation modes). As discussed above, these relaxation modes are essential to accurately capture anelastic behaviour at frequencies beyond those of the dynamic modes (Fig. 3.1a; or see Lau et al. 2015). Henceforth, we will use the symbol $\hat{X}$ to denote any variable X associated with the pseudo-eigenvalue problem (eq. 3.43).

Fig. 3.1(b) is a schematic illustration of the variation in the real part of modulus M across a large frequency band. We show two hypothetical models for Re$\{M\}$: A and B. If we were to solve the full eigenvalue problem as formulated within the seismological community we would omit the relaxation modes and include only dynamic modes. With this subset of modes, the application of a tidal force at ω_T (where it is assumed that ω_T lies far away from the seismic band) would lead to the same tidal predictions for both models A and B. The lowest frequency sampled by dynamic modes of a typical Earth model (e.g., PREM, Dziewonski & Anderson, 1981) is approximately 1 hour^{-1}.

Thus, behaviour at lower frequencies than this, where A and B begin to diverge, is not captured. In contrast, applying the ENM theory of Lau et al. (2015) which includes relaxation modes, or the DS variant, would yield distinct tidal predictions for models A and B. This is illustrated by the sampling of relaxation modes at different frequencies for the different models (Fig. 3.1b).

Finally, in the TNM method, which solves the pseudo-eigenvalue problem (eq. 3.43), the resulting pseudo-eigenmodes are limited to (an approximated version of) the dynamic modes. Specifically, the TNM treatment softens Re$\{M\}$ to the values relevant for the Earth at ω_T and this is the Earth that the pseudo-eigenmodes sample, irrespective of their eigenfrequency value. This is shown schematically by the green dashed lines in Fig. 3.1(b).

We have not yet discussed how a fully complex response is calculated using the TNM theory. Wahr & Bergen (1986) solved eq. (3.43), which is analagous to solving an elastic problem with elastic moduli fixed to a reduced value of $\mathbf{\Lambda}(\omega_T)$, and this yielded real $[\hat{\omega}_k{}^2, \hat{\mathbf{s}}_k]$. These eigenmodes were then combined to compute Re$\{\hat{h}\}$. (This approach is in contrast to the normal mode treatment of Tromp & Dahlen (1990) and Lognonné (1991) who computed complex eigenmodes.) Next, assuming that the effects of anelasticity are small enough that perturbations in $\mathbf{\Lambda}(\omega)$ scaled linearly to perturbations in h, they computed the imaginary component of $\hat{h}$ using the following expression

$$\mathrm{Im}\{\hat{h}(\omega)\} = \int_{\mathrm{CMB}}^{a} \frac{\partial \mathrm{Re}\{\hat{h}(\omega)\}}{\partial M(\omega, r)} \mathrm{Im}\{\delta M(\omega, r)\}\, \mathrm{d}r \ . \tag{3.44}$$

Wahr & Bergen (1986) estimated the partial derivative in this expression as

$$\frac{\partial \mathrm{Re}\{\hat{h}(\omega)\}}{\partial M(\omega, r)} \approx \frac{\mathrm{Re}\{\hat{h}(\omega)\} - \bar{h}}{\mathrm{Re}\{M(\omega)\} - \bar{M}} \ , \tag{3.45}$$

where $\bar{h}$ may be found by setting $\varepsilon^2 \to 0$ in eq. (3.40). They discuss in detail choices of ω that yield stable estimates of the partial derivative.

3.3 Comparison of Predictions Using the TNM and DS Theories

Predictions of body tides have numerous applications, including: correcting a wide range of space-geodetic observables for the body tide signal (e.g., IERS standards, Cartwright & Petit, 2004; Petit & Luzum, 2010); inferring anelastic structure from observations of tidal phase lags (e.g., Ray et al., 2001; Benjamin et al., 2006); and, potentially, estimating long-wavelength elastic and density variations in the mantle using tidal tomography (Métivier & Conrad, 2008; Latychev et al., 2009; Qin et al., 2014; Lau et al., 2015). In this regard, given the same input anelastic structure (defined by the tensor $\mathbf{\Lambda}(\omega)$), the TNM and more accurate ENM/DS treatments of the body tide response of the Earth will predict different values of the frequency dependent Love number $h(\omega)$. In this section, we present several simple numerical examples that highlight these differences (Section 3.3.1) and discuss their implications for the interpretation of tidal phase lags (Section 3.3.2).

3.3.1 Numerical Predictions

In the results below, we adopt several models for the form of $\mathbf{\Lambda}(\omega)$ and predict the Love number h as well as a phase parameter Υ, defined as:

$$\Upsilon \equiv \arctan\left(\frac{\mathrm{Im}\{h\}}{\mathrm{Re}\{h\}}\right) . \tag{3.46}$$

To begin, we repeat the calculations based on the TNM treatment to demonstrate that we can reproduce the Wahr & Bergen (1986) results for the M2 semi-diurnal body tide (see Fig. 3.2). These calculations incorporate the isotropic elastic and density structure of seismic model 1066A (Gilbert & Dziewonski, 1975) and perturb this structure by assuming a frequency-dependent Q of the form:

$$Q(\omega) = Q(\omega_0)\left(\frac{\omega}{\omega_0}\right)^{\alpha} , \tag{3.47}$$

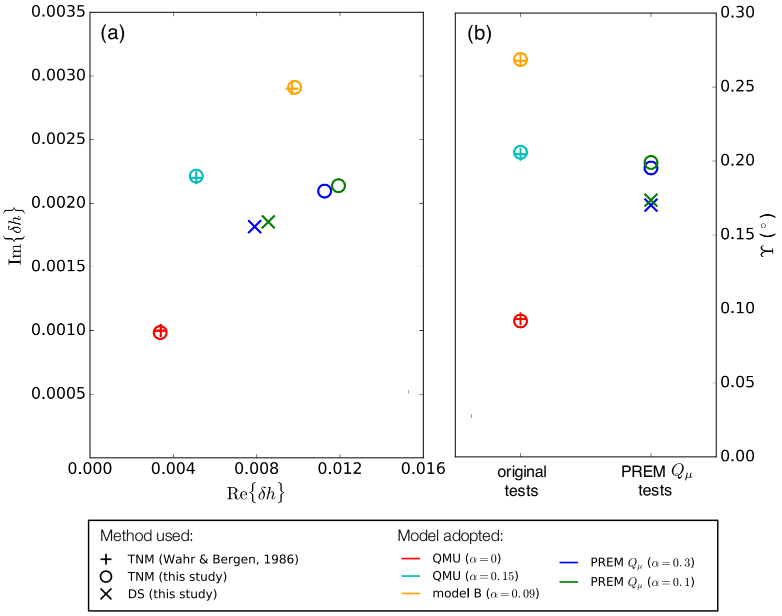

FIGURE 3.2: Predictions of (a) the perturbations to the degree-2 tidal Love number, $\mathrm{Re}\{\delta h\}$ and $\mathrm{Im}\{\delta h\}$, and (b) the predicted tidal phase lag, Υ, calculated using the (circles) TNM and (Xs) DS (Lau et al., 2015) theories for five different Earth models distinguished on the basis of elastic and anelastic properties. The crosses (+) are three results taken directly from the Wahr & Bergen (1986) study that derived the TNM approach. The overlap of the crosses and circles demonstrates that we are able to correctly implement the TNM approach. We note that the reference frequencies, ω_m, for the PREM Q_μ ($\alpha = 0.3$) and PREM Q_μ ($\alpha = 0.1$) Earth models are 3.09×10^{-4} Hz and 5.0×10^{-4} Hz, respectively.

where $Q(\omega_0)$ is the attenuation at reference frequency ω_0. We note that values for α across the seismic-tidal band have been shown to lie between 0.1–0.35 (Faul & Jackson, 2015) but as $\omega \to 0$, $\alpha \to 1$ if one adopts a Maxwell rheological model. The specific choice of phenomenological model is, however, not a focus of this paper. Wahr & Bergen (1986) assumed dissipation in the shear modulus only, and they adopted the expression

$$\delta\mu = \mu(\omega_0)\left\{\cot\left(\frac{\alpha\pi}{2}\right)\left[1-\left(\frac{\omega_0}{\omega}\right)^{\alpha}\right]+i\left(\frac{\omega_0}{\omega}\right)^{\alpha}\right\}\frac{1}{Q_\mu(\omega_0)}\,. \tag{3.48}$$

In this equation, Q_μ is the attenuation associated with μ. In tidal applications it is common to exclude the contribution from bulk dissipation (e.g., Wahr & Bergen, 1986; Benjamin et al., 2006) since many Q models derived from seismic observations (e.g., Dziewonski & Anderson, 1981; Durek & Ekstrom, 1996) exhibit very high values for Q_κ. More recent work, however, suggests that at these frequencies bulk dissipation may play an important role when considering porous media in the presence of partial melt (Takei & Holtzman, 2009). To incorporate bulk dissipation in our theory, the appropriate expression for $\kappa(\omega)$ need only be inserted in the relevant elements of the stress tensor $\mathbf{\Lambda}$ (see eq. 3.6).

Wahr & Bergen (1986) adopted the depth-dependent attenuation models 'QMU' (Sailor & Dziewonski, 1978) and 'Model B' (Sipkin & Jordan, 1979). We performed predictions for three cases: (i) QMU with $\alpha = 0.0$; (ii) QMU with $\alpha = 0.15$ and (iii) Model B with $\alpha = 0.09$. We note that as $\alpha \to 0$,

$$\delta\mu \to \mu(\omega_0)\left[\frac{2}{\pi}\ln\left(\frac{\omega}{\omega_0}\right) + i\right]\frac{1}{Q_\mu(\omega_0)} \tag{3.49}$$

(Kanamori & Anderson, 1977). The results for all three cases in Fig. 3.2 show excellent agreement between predictions of the complex Love number perturbation reported by Wahr & Bergen (1986) and our predictions based on their approach.

We next compare predictions based on the TNM theory and the DS theory using two models of mantle anelasticity described by Benjamin et al. (2006). Both these models adopt the isotropic version of PREM (Dziewonski & Anderson, 1981) and the depth-dependent Q structure of PREM (Q_μ only) at the reference frequency, f_0, of 1 Hz (note we will use the symbol f when referring to numerical values for frequencies, where $f = \omega/2\pi$). The models also assume the frequency-dependent form of Q given by eq. (3.47). The perturbation to μ in both cases is given by

$$\delta\mu(\omega) = \begin{cases} \mu(\omega_0)\left[\frac{2}{\pi}\ln\left(\frac{\omega}{\omega_0}\right) + i\right] Q(\omega_0)^{-1}, \text{ for } \omega \geq \omega_m \\ \mu(\omega_0)\left[\frac{2}{\pi}\left\{\ln\left(\frac{\omega_m}{\omega_0}\right) + \frac{1}{\alpha}\left[1 - \left(\frac{\omega_m}{\omega}\right)^\alpha\right]\right\} + i\left(\frac{\omega_m}{\omega}\right)^\alpha\right] Q(\omega_0)^{-1}, \text{ for } \omega < \omega_m \end{cases}, \tag{3.50}$$

where the free parameter ω_m is the frequency that defines the onset of frequency-dependent behaviour in Q. We adopt two choices for this frequency, f_m, (chosen from a subset of values shown in Figs 6–7 of Benjamin et al., 2006): (i) 3.09×10^{-4} Hz, with $\alpha = 0.2$; and (ii) 5.0×10^{-3} Hz, with $\alpha = 0.1$. Both these frequencies are significantly higher than the semi-diurnal frequency.

Fig. 3.2(a) shows that there is a systematic difference in the predictions based on the two theories. In both cases, the formulation of Wahr & Bergen (1986) overestimates Re$\{\delta h\}$ and Im$\{\delta h\}$ by ~ 50 % and ~ 15 %, respectively. As a result, the traditional theory overestimates the lag angle Υ by ~ 20 % (Fig. 3.2b).

3.3.2 IS INTRINSIC Q THE SAME AS 'OBSERVED Q'?

In this section we highlight the implications of our revision to the body tide theory for the interpretation of tidal observations. To begin, we define Υ as the observed phase lag at the planetary-scale with respect to the forcing and φ as the phase lag between stress and strain for a material sample:

$$\check{Q}^{-1} \approx \tan[\Upsilon(\omega)] = \frac{\text{Im}\{h(\omega)\}}{\text{Re}\{h(\omega)\}}, \tag{3.51}$$

$$Q^{-1} \approx \tan[\varphi(\omega)] = \frac{\text{Im}\{Q(\omega)\}}{\text{Re}\{Q(\omega)\}}. \tag{3.52}$$

We refer to the quantity $\check{Q}^{-1}$ as the apparent attenuation (i.e., the attenuation manifest in observations and to which tidal calculations discussed above are compared) and Q^{-1} as the intrinsic (i.e.,

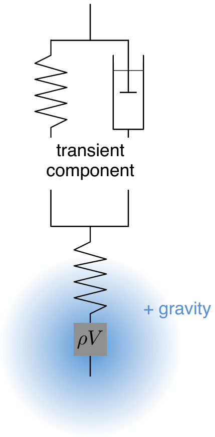

FIGURE 3.3: A schematic illustration of the system described by eq. (3.16). The Kelvin-Voigt element is left incomplete to imply any combination of spring-dashpot elements to form a transient component to the system. Additional components to the system include the mass component, ρV, to represent the presence of inertia and the blue shading to represent the presence of self-gravity (see text).

material) attenuation. It is common to assume that $\check{Q}^{-1}$ and Q^{-1} are equivalent (Ray et al., 2001; Benjamin et al., 2006). However, while the difference between the two parameters is subtle, we demonstrate in this section that distinguishing between them is crucial for a robust understanding of Earth's anelastic response across a wide frequency band.

To illustrate the relevant arguments, consider the schematic Fig. 3.3, which shows a system involving a 1-D analogue of anelastic behaviour. The spring-dashpot component is left incomplete to imply any linear combination of mechanical elements may be applied in this scenario to represent the transient component (e.g., an absorption band, Kanamori & Anderson, 1977). In addition to this, several components are included in Fig. 3.3 which illustrate processes ongoing across the entire planet: inertia and self-gravity. The former is represented by the mass component, ρV, and the latter by the blue shading. In previous studies, planetary-scale phase lags, Υ, have been interpreted as reflecting only the intrinsic anelastic property of the material that forms the building blocks of the planet (i.e., these studies have ignored the impact of the mass component and gravitational body force on the observed lag; e.g., Wahr & Bergen, 1986; Ray et al., 2001; Benjamin et al., 2006). However, consideration of all these issues is required to accurately interpret the anelastic response of the Earth. In the following, we will use numerical calculations to consider, in turn, each factor that distinguishes these two interpretations (inertia, self-gravity, energy considerations, as defined below) and demonstrate how the intrinsic attenuation, Q^{-1}, may be extracted from the apparent attenuation, $\check{Q}^{-1}$.

We note that different processes (e.g., body waves or tides) will be sensitive to different regions of the spatially-varying Q^{-1} structure of the Earth (see, e.g., the Q model of Durek & Ekstrom, 1996). This issue will, in general, complicate the mapping between Q and $\check{Q}$ and we address it in detail in future work. In the discussion below we avoid this complication by adopting a simple anelastic Earth model and focusing on observables with comparable spatial sensitivity. Nevertheless, the calculations are sufficiently complex to demonstrate the main points in our present argument.

The calculations discussed below adopt the elastic and density structure of the seismic model PREM (Dziewonski & Anderson, 1981). We will assume a spatially-uniform Q_μ value of 250 throughout the mantle, and frequency dependence governed by eq. (3.50) with parameter values $\alpha = 0.3$, $f_0 = 1$ Hz, and $f_m = 3.09 \times 10^{-4}$ Hz. Fig. 3.4 (black line) shows the resulting frequency dependence of the intrinsic attenuation Q^{-1}.

The orange line on the same figure is the prediction of $\check{Q}^{-1}$ based on the theory of Wahr & Bergen (1986) applied to the above model of anelastic Earth structure. This prediction clearly differs from the imposed Q^{-1}. If, for example, one were to assume that this prediction was equivalent to intrinsic attenuation Q^{-1} (e.g., Ray et al., 2001; Benjamin et al., 2006), then one would overestimate the latter by a factor of ~ 2 within the semi-diurnal frequency.

It is particularly important to emphasize the implications of the above error for inferences of the frequency dependence of Q^{-1}. Tidal and seismic observations sample anelastic behavior at a relatively small set of frequencies. For example, let us presume that the red crosses labeled A and B in Fig. 3.4 represent observations of attenuation with two distinct frequencies: a semi-diurnal tide,

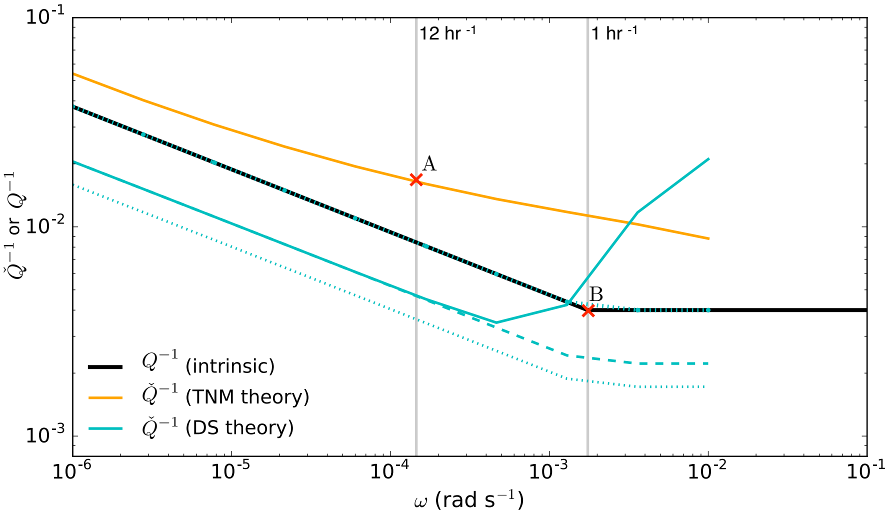

FIGURE 3.4: Intrinsic attenuation, Q^{-1} (black line), as a function of frequency associated with the anelastic Earth model described in the text (see Section 3.3.2). The remaining lines are various predictions of apparent attenuation, $\check{Q}^{-1}$, based on the same Earth model: Orange line - prediction using the TNM theory; solid cyan line - prediction using the DS theory dashed cyan line - correction to the solid cyan line to remove the impact of inertia; dotted cyan line - correction to the solid cyan line to remove the impact of both inertia and self-gravity; dashed-dotted cyan line (coincident with the black line) - calculation in which the solid cyan line is mapped into intrinsic attenuation using the expression (3.61). The two highest frequency predictions using the DS theory (solid cyan line) have been multiplied by -1 so they may be plotted on the same log-log scale. (We note in this regard that a system will oscillate in anti-phase with a forcing if the forcing has a frequency well above the resonant frequency of the system.) Points A and B mark frequencies that can be realistically observed on Earth: the semi-diurnal tide M2 and the $_0\mathcal{S}_2$ normal mode, respectively. See Section 3.3.2 for further discussion.

with frequency of 12 hour^{-1}, and the seismic free oscillation $_0\mathcal{S}_2$, with frequency of $\sim$ 1 hour^{-1}. (Lau et al. (2015) demonstrated that $_0\mathcal{S}_2$ deformation is responsible for 95 % of the semi-diurnal body tide response, and thus both observations sample very similar Q structure; see Anderson & Minster (1979); Benjamin et al. (2006).) The goal in the application of TNM theory of body tides would be to accurately predict the observation A, and this might lead, e.g., to the orange line in Fig. 3.4. As noted above, whilst this is in fact a prediction of apparent attenuation, it has been commonly interpreted as an accurate proxy for the intrinsic attenuation at this frequency. In contrast, seismic normal mode measurements of the decay time of the $_0\mathcal{S}_2$ mode would infer the correct value of intrinsic attenuation $Q(\omega)^{-1}$ at 1 hr^{-1}, i.e., the value at point B. Using these two observables, one might suppose a variety of trends in the intrinsic attenuation between A and B, but a simple straight line (or equivalently, a constant exponent in ω^{α}) would clearly yield an inaccurate model for the true trend.

The solid cyan line in Fig. 3.4 shows the trend in $\check{Q}^{-1}$ computed using the DS theory. Of course, it would also be incorrect to assume that these predictions reflect the intrinsic attenuation, but the following question arises: If calculations of $\check{Q}^{-1}$ in the tidal band based on the DS (or ENM) theory and a specific model of anelastic structure, fit available observations, can one extract a robust estimate of intrinsic attenuation and (through a comparison with seismic observation of attenuation) its frequency dependence? To answer this question requires that we consider and correct for each of the physical cases that differentiate the intrinsic attentuation from the observed (and modeled) response of the Earth (i.e., the apparent attenuation). In this regard, in the next three sections we outline a set of progressive corrections that accurately map $\check{Q}^{-1}(\omega)$, as computed using the DS and ENM methods, into $Q^{-1}(\omega)$.

3.3.3 INERTIA

Consider, once again, the apparent attenuation in Fig. 3.4 computed using the DS theory. At frequencies lower than $\sim 4 \times 10^{-4}$ rad s^{-1} the slope of $\check{Q}^{-1}(\omega)$ accurately tracks the trend in intrinsic attenuation Q^{-1}, however the values on the former are offset to lower values than those on the latter. The difference between the predictions of $\check{Q}^{-1}$ based on the TNM and DS (or ENM) theories is to be expected given the results in Fig. 3.2(b). The large swing in $\check{Q}^{-1}$ predicted by the DS theory at frequencies above $\sim 4 \times 10^{-4}$ rad s^{-1} is due to resonant effects associated with the dynamic eigenmodes (the lowest frequency of which is ≈ 1 hr^{-1}).

The first correction toward mapping the $\check{Q}^{-1}$ prediction computed using the DS (or ENM) method into an estimate of the intrinsic attenuation thus involves the removal of this resonance effect. This is equivalent to neglecting inertia in the calculation by invoking the limit $\omega_T \rightarrow 0$ in eqs (3.40-3.41). The result of applying this correction is shown by the dashed cyan line in Fig. 3.4, which now accurately follows (with a constant offset) the frequency dependence of Q^{-1}.

3.3.4 SELF-GRAVITY

The tidal force causes expansional deformation on the Earth and acting against this deformation are the elastic restoring forces and inward self-gravity which are embedded in the operator $\mathcal{H}$ (eq. 3.11). In the case of the body tide problem, both forces in $\mathcal{H}$ resist the expansion and as such, the self-gravity term provides an additional effective rigidity to the elastic rigidity. We note that Efroimsky (2012, 2013) discusses this physics in relation to Earth and super-Earths and argues that the effect cannot be ignored when considering tidal dissipation on the latter planets. The same process acts on Earth, and contributes to a difference in intrinsic and apparent attenuation. To remove gravity from the general equations, we take the limits $\Phi \rightarrow 0$ and $\phi \rightarrow 0$, so that the operator $\mathcal{H}$ in eq. (3.11) becomes

$$\rho \mathcal{H} \mathbf{s} = -\nabla \cdot (\mathbf{\Lambda} : \nabla \mathbf{s}) \ . \tag{3.53}$$

In this case, the only restoring force arises from the elastic properties of the Earth. In the schematic Fig. 3.3 this would be equivalent to removing the body force from the system. This procedure represents the second correction necessary to map $\check{Q}^{-1}$ to Q^{-1}, and applying it to the dashed cyan line in Fig. 3.4 yields the result shown by the dotted cyan line. The resultant reduction in the attenuation is due to the increase of Re$\{h\}$ associated with a lowering of the effective rigidity when gravitational body forces are removed. Moreover, the constant shift downwards from dashed to dotted cyan line reflects the fact that the contribution from gravity is independent of frequency. We further note that self-gravity would have the opposite effect if the induced deformation was compressional, acting in the same direction as the external forcing, thus lessening the effective rigidity.

3.3.5 ENERGY CONSIDERATIONS

In this section we revisit eq. (3.40), though we note that all the results below hold for eq. (3.41). Removing the impact of inertia from eq. (3.40), as discussed in Section 3.3.3, yields

$$h_\ell(\omega_T) = \frac{1}{g} \sum_n \frac{{}_n\bar{U}_\ell}{\bar{\omega}_n{}^2 + \varepsilon_n{}^2} \int_0^a \rho(r) \frac{r^{\ell+1}}{a^\ell} \left[\ell{}_n\bar{U}_\ell(r) + \sqrt{\ell(\ell+1)}{}_n\bar{V}_\ell(r) \right] \mathrm{d}r \; . \tag{3.54}$$

Following Section 3.3.4, we note that the eigenfunctions and eigenfrequencies in these expressions are associated with a system without self-gravity (the operator $\mathcal{H}$ is given by eq. 3.53).

To complete the mapping between $\check{Q}^{-1}$ and Q^{-1} we recall arguments made by O'Connell & Budiansky (1978) who, in a similar vein as the present study, set out to clarify the distinction between the intrinsic Q^{-1} of a material and measures of $\check{Q}^{-1}$ in several phenomenological processes (e.g., traveling plane waves, standing waves). In particular, we interpret Q^{-1} using energy considerations as briefly mentioned in Section 3.2.1. To begin, we rewrite the definition in eq. (3.9) as

$$Q^{-1} \equiv \frac{\Delta W}{W} \; , \tag{3.55}$$

where ΔW and W represent the dissipated and stored energies per cycle, respectively. When considering a vibrating system close to resonance, one may treat the system as having only one degree of freedom; we can thus identify the pair ΔW_k and W_k for each eigenmode, k. We note that such an approach already exists in the seismic normal mode literature (see Dahlen & Tromp, 1998). Accordingly, for the particular case described by eq. (3.54), invoking the definition given by eq. (3.51) yields (see Appendix B):

$$\begin{aligned}\check{Q}^{-1} &= \frac{\sum_k \chi_k \, \mathrm{Im}\{{\varepsilon_k}^2\}}{\sum_k \chi_k \left({\bar{\omega}_k}^2 + \mathrm{Re}\{{\varepsilon_k}^2\}\right)} \\ &= \frac{\sum_k \chi_k \int_V \nabla \mathbf{s}_k^* : \mathrm{Im}\{(\mathbf{\Lambda}(\omega_T)\} : \nabla \mathbf{s}_k \, \mathrm{d}V}{\sum_k \chi_k \left({\bar{\omega}_k}^2 \int_V \rho \, {\mathbf{s}_k}^* \cdot \mathbf{s}_k \, \mathrm{d}V + \int_V \nabla \mathbf{s}_k^* : \mathrm{Re}\{\delta \mathbf{\Lambda}(\omega_T)\} : \nabla \mathbf{s}_k \, \mathrm{d}V\right)} \ , \end{aligned} \tag{3.56}$$

where

$$\chi_k = \frac{\int_0^a \rho(r) \frac{r^{\ell+1}}{a^\ell} \left[\ell_n \bar{U}_\ell(r) + \sqrt{\ell(\ell+1)}_n \bar{V}_\ell(r)\right] \, \mathrm{d}r}{{\bar{\omega}_k}^4 + \mathrm{Im}\{{\varepsilon_k}^2\}^2} \ . \tag{3.57}$$

χ_k represents a weighting of each mode which reflects excitation by the tidal forcing.

The first term in the denominator of eq. (3.56) is the kinetic energy (this term is equivalent to the stored elastic energy) and the second term is the energy correction associated with dispersion. The numerator is the energy loss due to dissipation. That is,

$$\Delta W_k = \chi_k \int_V \nabla {\mathbf{s}_k}^* : \mathrm{Im}\{\mathbf{\Lambda}(\omega_T)\} : \nabla \mathbf{s}_k \, \mathrm{d}V \ , \tag{3.58}$$

where, for the specific Q model we have prescribed (i.e., where all dissipation occurs in shear energy)

$$\Delta W_k = \chi_k \int_V 2\mu \left({\mathbf{d}_k}^* : \mathbf{d}_k\right) Q_\mu(\omega)^{-1} \, \mathrm{d}V \ . \tag{3.59}$$

In this expression $\mathbf{d}$ is the deviatoric strain. Since the energy associated with dispersion is much smaller than the elastic energy, one can make the following approximation

$$W_k \approx \chi_k {\bar{\omega}_k}^2 \int_V \rho \, {\mathbf{s}_k}^* \cdot \mathbf{s}_k \, \mathrm{d}V \ , \tag{3.60}$$

where, if the system included self-gravity, an additional gravitational potential energy term would contribute to W. Our final, complete form for the mapping between $\check{Q}^{-1}$ and Q^{-1} is thus given by

$$\check{Q}^{-1}(\omega_T) = \left(\frac{\sum_k \chi_k \int_V 2\mu \left(\mathbf{d}_k{}^* : \mathbf{d}_k \right) \mathrm{d}V}{\sum_k \chi_k \, \bar{\omega}_k{}^2 \int_V \rho \, \mathbf{s}_k{}^* \cdot \mathbf{s}_k \, \mathrm{d}V} \right) Q^{-1}(\omega_T) \ . \tag{3.61}$$

This expression relates the apparent attenuation arising from a planetary-scale phase lag in the tidal response to the intrinsic attenuation of the material that comprises the planet. The simple mapping between $\check{Q}^{-1}$ and Q^{-1} is only possible in our specialized case where Q^{-1} is spatially uniform. Using this expression in Fig. 3.4 yields a line that precisely matches the intrinsic attenuation $Q(\omega)^{-1}$ adopted in the simulations.

We note that Nowick & Berry (1972, Appendix A) present an analysis of the energy budget for the case of a 1-D spring-dashpot system . The mapping between $\check{Q}^{-1}$ and Q^{-1} for their toy example is analagous to our eq. (3.61).

3.4 SUMMARY

Lau et al. (2015) presented an extended normal mode (ENM) theory for predicting body tides on an aspherical, rotating and anelastic Earth. In this paper we have elaborated on the ENM theory, as well as a relatively minor variant, the direct solution (DS) approach, and have explored the implications of the theory for the modeling of anelastic effects and interpretations of relevant observations. Our theory differs from the traditional normal mode (TNM) theory of Wahr & Bergen (1986) in several significant ways:

1. it is based on a pure normal mode formalism that is in accord with, and extends, the theory used in seismic free oscillation research by incorporating a set of relaxation modes that are not considered in the TNM theory; and

2. it treats anelastic effects on each mode by determining the imaginary perturbation to their

eigenfrequencies. The TNM theory, in contrast, estimates the imaginary part of the full response by considering the imaginary part of the modulus perturbation.

Given the same model for anelastic Earth structure, the more accurate ENM (or DS) theory will predict a different perturbation to tidal Love numbers than the TNM method and this will have implications not only for the inferences of the anelastic structure of the Earth but also for model-based corrections to geodetic data that are applied to remove the body tide signal.

We have also demonstrated that previous analyses of the tidal phase lag observation have, in effect, assumed that the tidal lag angle on a planetary-scale is the same as the loss angle (i.e., the lag angle between the stress and strain acting on a material sample, see eq. 3.52). We have shown that if inertia, self-gravity and energy considerations are taken into account, the true loss angle, or equivalently the intrinsic Q^{-1}, may be accurately extracted from the observed planetary phase lag, or apparent $\check{Q}^{-1}$. If these issues are not addressed, it is likely that systematic biases in the estimates of the frequency dependence of Q^{-1} will arise. Our formulation provides a rigorous procedure for estimating intrinsic attenuation in the tidal band and for connecting measurements of dissipation across frequencies that span tidal to seismic processes.

As a final note, we emphasize that the generalized treatment of anelasticity described here and in Lau et al. (2015) may be applied to investigate the response of other planetary bodies to tidal forcing. Indeed, planetary science provides a far broader range of physical conditions than the geophysical applications we have focused on, and this range will no doubt sample regimes with sensitivities vastly different from those explored in our simple numerical examples. As one obvious example, the impact of self-gravitation on the anelastic response of massive super-Earths will be significantly larger than the already important effect revealed in Fig. 3.4. More generally, observational constraints on other terrestrial bodies are often limited to an estimate of the tidal Love number, and the correct interpretation of this number is then clearly critical to any assessment of physical conditions of that body.

4

Tidal Tomography Constrains Earth's Deep Mantle Buoyancy Structure

Goals are overrated. The beauty is in the struggle.
—J. Wilson

4.1 Introduction

Earth's elastic and density structure is dominated by spherical symmetry (i.e., structure that varies with depth), as captured by seismic reference (or 1-D) models such as PREM (Dziewonski & Anderson, 1981). However, beginning in the early 1980s, images of Earth's interior provided by seismic tomography have revealed more complicated structures characterized by laterally varying, percent-level perturbations in seismic wave speed (Ritsema et al., 2011; Masters et al., 2000). These perturbations reflect thermal and/or compositional heterogeneity linked to mantle convection, the main driving force for plate tectonics and, more generally, the long-term evolution of the Earth system. Constraining the thermochemical structure of the Earth's mantle, and its associated dynamics, remains a key goal in global geophysical research.

Since mantle convection is driven by density variations, or buoyancy, the density field of the Earth is a key parameter in constraining the dynamics of mantle flow. Seismic tomographic images show fast wave speed anomalies that spatially correlate with the history of subduction, indicative of colder than average mantle, and thus relatively dense material, driving downward flow (van der Hilst et al., 1991; Zhao, 2004). However, the interpretation of slow wave speed anomalies in the form of large-scale domes rising $\sim$1000 km above the core-mantle boundary (CMB) beneath southern Africa and the Pacific (Ritsema et al., 2011; Ishii & Tromp, 1999; Masters et al., 2000) remains a source of contention (Davies et al., 2012).

The debate regarding these structures (commonly known as the 'large low shear velocity provinces', LLSVPs; shown in Fig. 4.1) centers, at least to some extent, on their net buoyancy. An important complication is that the low seismic wave speeds that characterize the LLSVPs may be due to thermal and/or chemical effects, and thus the buoyancy of the structures derives from some combination of these effects: a hot, thermal anomaly producing positive buoyancy, and compositional heterogeneity (e.g., from the enrichment of iron) with an intrinsic negative buoyancy. The uncertainty in the relative contribution of these effects has led to significantly contrasting views of large-scale mantle dynamics: e.g., these may represent denser than average regions and thus a less energetic mode of mantle convection (Ishii & Tromp, 1999; Kellogg et al., 1999; Tackley, 2002; Trampert et al., 2004; Moulik & Ekström, 2016) or the converse (Davies et al., 2012; Hager et al., 1985; Forte & Mitrovica, 2001).

With the growing availability of highly precise space-geodetic measurements of crustal deformation, modeling studies (Dehant et al., 1999; Métivier & Conrad, 2008; Latychev et al., 2009; Ito & Simons, 2011; Qin et al., 2014) have begun to explore the information content of tidal observations.

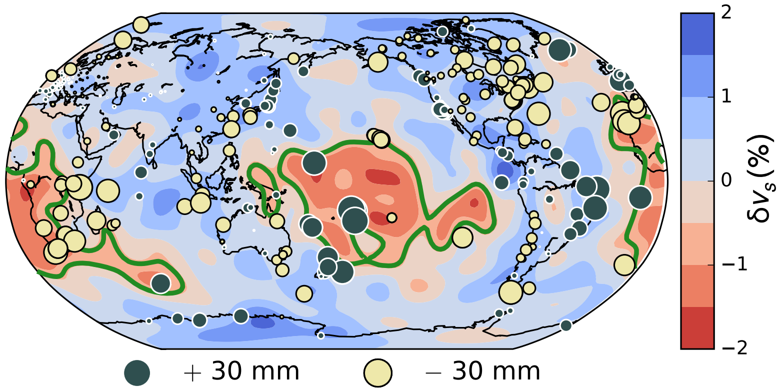

Figure 4.1: Circles indicate locations of GPS stations used in this study (Yuan et al., 2013). The size of the circle is proportional to the amplitude of the in-phase (relative to the tidal potential) vertical displacement associated with the M2 body tide after removing predictions from a 1-D density, elastic and anelastic model (PREM Dziewonski & Anderson, 1981) and correcting for crustal (Laske et al., 2013) and core-mantle boundary (Mathews et al., 2002) topography (see Section 4.4 for details). Dark blue circles indicate positive residuals and yellow circles indicate negative residuals. The underlying contour field displays the shear wave speed (v_s) tomography model S40RTS (Ritsema et al., 2011) at 2800 km depth. The solid green lines mark the boundaries of the two Large Low Shear Velocity Provinces (LLSVPs) as defined by the 0.65% relative perturbation in shear wave speed (Torsvik et al., 2006).

Furthermore a recent study has probed 1-D Earth structure beneath the western US using observations of crustal deformation driven by ocean tides (Ito & Simons, 2011). In this chapter, we image lower mantle density variations using a powerful new tomographic procedure—tidal tomography—based on high-precision, GPS-derived observations of the Earth's body tide. Tidal tomography provides an independent constraint on the long-wavelength density and elastic structure of the Earth. The methodology is based on the theoretical advances in the treatment of the Earth's body tidal response described in Chapters 2 and 3 (Lau et al., 2015) and our application takes advantage of a data set comprised of crustal displacement measurements in the semi-diurnal tidal band recorded by a global network of GPS stations with sub-mm level precision (Yuan et al., 2013). Tidal deformations are sensitive to deep mantle, long-wavelength structure (see below) and thus our tomographic procedure is uniquely suited to investigating the nature of the LLSVPs.

The symbols in Fig. 4.1 display the in-phase (with respect to the tidal potential) vertical crustal displacement of the M2 semi-diurnal body tide corrected for rotational effects, crustal and core-mantle boundary topography, and 1-D density, elastic, and anelastic structure (Yuan et al., 2013). The residual signal is comprised of errors in the above corrections, displacements associated with ocean tidal loading and the perturbation to the body tide response due to lateral variations in mantle elastic and density structure. Constraining the deep, long-wavelength component of the latter field is the goal of this study. Fig. 4.1 also shows the shear wave speed heterogeneity in the deep mantle (2800 km depth) according to tomographic model S40RTS (Ritsema et al., 2011), and highlights the locations of the two LLSVPs.

4.2 Procedure

We performed preliminary sensitivity analyses which indicated that the body tide response is sensitive to long-wavelength shear wave speed (v_s) and density (ρ) structure in the deepest parts of the mantle (Fig. 4.2, left and middle columns, top two rows) and is relatively insensitive to bulk sound speed (v_b) (Fig. 4.2, right column).

To explore this issue further, and to guide the tomographic analysis described below, we performed a second sensitivity analysis designed as follows. First, we adopted variations in v_s within the mantle using one of five seismic tomographic models: GYPSUM (Simmons et al., 2010); HMSL (Houser et al., 2008); S362MANI (Kustowski et al., 2008); S40RTS (Ritsema et al., 2011); or SAW24B16 (Mégnin & Romanowicz, 2000), and scaled these variations in shear wave speed to variations in bulk sound speed using a fixed scaling $R_b = \delta v_s / \delta v_b = 0.05$ (Masters et al., 2000). (Note that δX denotes the fractional perturbation in parameter X.) Next, we divided the bottom 1020 km of the mantle into three layers: 'deep' (2891–2551 km depth), 'mid' (2551–2211 km depth), and 'top' (2211–1871 km depth). Across each of these layers we defined two regions: 'LLSVP' and 'outside'. The areal extent of the LLSVP regions in each layer is defined by the -0.65% vs contour (Torsvik et al., 2006) and any region outside these defined margins is considered to be 'outside'. We then per-

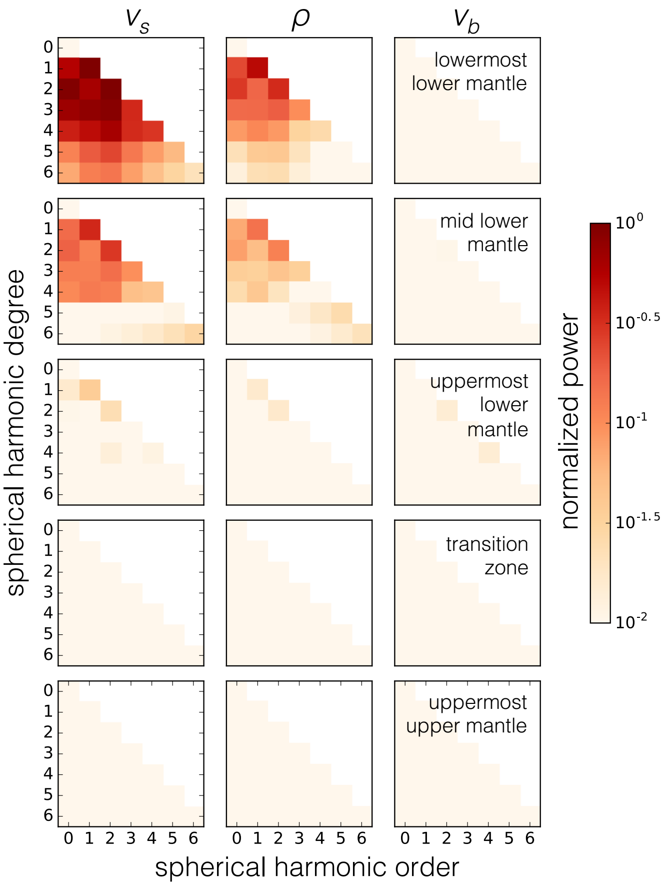

FIGURE 4.2: The sensitivity of the computed semi-diurnal body tide response to perturbations in (left) shear wave speed (v_s), (middle) density (ρ), and (right) bulk sound speed (v_b) structure. Perturbations to structure are applied in five layers throughout the mantle (from top row to bottom): lowermost lower mantle (2891–2211 km depth); mid lower mantle (2211–1201 km depth); uppermost lower mantle (1201–670 km depth); transition zone (670–400 km depth); and uppermost upper mantle (400–24 km). The perturbations are expressed in terms of normalized power and decomposed into spherical harmonic coefficients up to degree and order 6. We define the normalized power as the total sum of the squared residual (3-D minus 1-D Earth model).

turbed the density in each of the six regions by 5% and computed the perturbation in the M2 body tide response at all sites shown in the GPS network of Fig. 4.1. This procedure was repeated for each of the five seismic tomographic models.

Fig. 4.3(a) provides a measure of the sensitivity (defined by the sum of the squares of the perturbed body tide response at all sites) derived from the above calculations. For results based on each seismic tomographic model (i.e., each panel in the figure), the sensitivities are normalized by the largest of the values computed for the six regions. The results show good consistency across the different shear wave tomographic models. This consistency reflects the fact that while the five tomographic models are derived from a wide range of seismic data sets, they have similar long-wavelength structure (Lekić et al., 2012). The four tomographic models other than HMSL show dominant sensitivities to perturbations in density within the two regions that comprise the base layer, and to a lesser extent (with the exception of SAW24B16) the mid layer within the LLSVPs. Calculations based on the HMSL model are characterized by sensitivity to the two deep base layer regions and the mid layer region outside the LLSVPs. Fig. 4.3(b) is a schematic representation of the average sensitivity across all five tomographic models within each of the six spatial regions. From this we reduce our model parameter space to the three regions within which perturbations in density have the greatest impact on the M2 body tide response: deep LLSVP (DL), deep outside (DO), and mid LLSVP (ML). (Given the negligible difference in the sensitivity of the response to variations in either of the mid layer regions, i.e., within and outside the LLSVPs, we additionally performed an analysis considering the regions DL, DO and the entire mid layer as a single region. The final conclusions of such a parameterization are consistent with those discussed below.)

Our inversion procedure is focused on these three regions and is based on a probabilistic approach with a penalty function related to how well a given model prediction correlates with the body tide observations. Specifically, our approach searches for coherence between predictions based on models with laterally varying mantle structure and the large and globally distributed geodetic data set, and it is particularly suited to data sets involving significant levels of noise. The procedure is as follows: (1) We produce a large data set by randomly sampling the entire data set shown in Fig. 4.1 in accordance with the assigned Gaussian errors associated with each station (Yuan et al., 2013). Each station is sampled with a frequency that depends on how densely it is clustered with other sites in or-

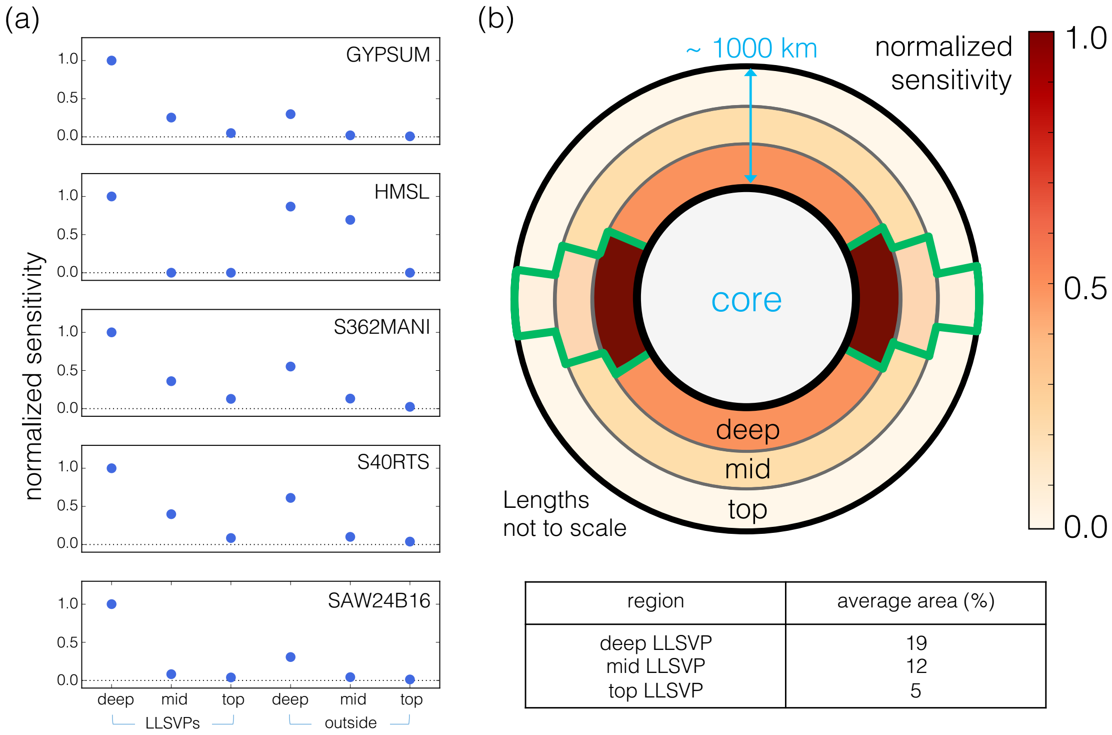

region	average area (%)
deep LLSVP	19
mid LLSVP	12
top LLSVP	5

FIGURE 4.3: Analysis of the sensitivity of the body tide response as measured by the global GPS network (Fig. 4.1) to perturbations in density within the six deep mantle regions defined in the text (deep, mid and top 'LLSVP'; deep, mid and top 'outside'). (a) Each frame refers to an analysis based on one of the five v_s tomography models described in the text, as labeled (Ritsema et al., 2011; Simmons et al., 2010; Houser et al., 2008; Kustowski et al., 2008; Mégnin & Romanowicz, 2000). In each case we compute the sum of the squares of the difference between the 3-D and 1-D Earth model response, where the former is defined by a 5% perturbation in density across one of the six deep mantle regions, as indicated on the abscissa. The results on each frame are normalized by the greatest of the six RMS differences. Other details of the analysis are described in the text. (b) A schematic diagram showing the geometry of the six regions considered in the sensitivity analysis, where the color intensity indicates the average normalized sensitivity across the five v_s tomography models in frame (a). The table beneath lists the total areal extent of the LLSVPs within each depth layer.

der to limit bias within the sampled data set toward data in any single geographic region. Fig. 4.4(a) (top panel) shows a histogram of RMS residuals after these samples are corrected (see Yuan et al., 2013) for the geographically uniform body tide prediction based on the 1-D elastic, anelastic and density model (we denote these residuals as u_{RAW}); (2) we apply additional corrections associated with Earth rotation (u_{ROT}) and core-mantle boundary (u_{CMB}) and crustal topographies (u_{CT}).

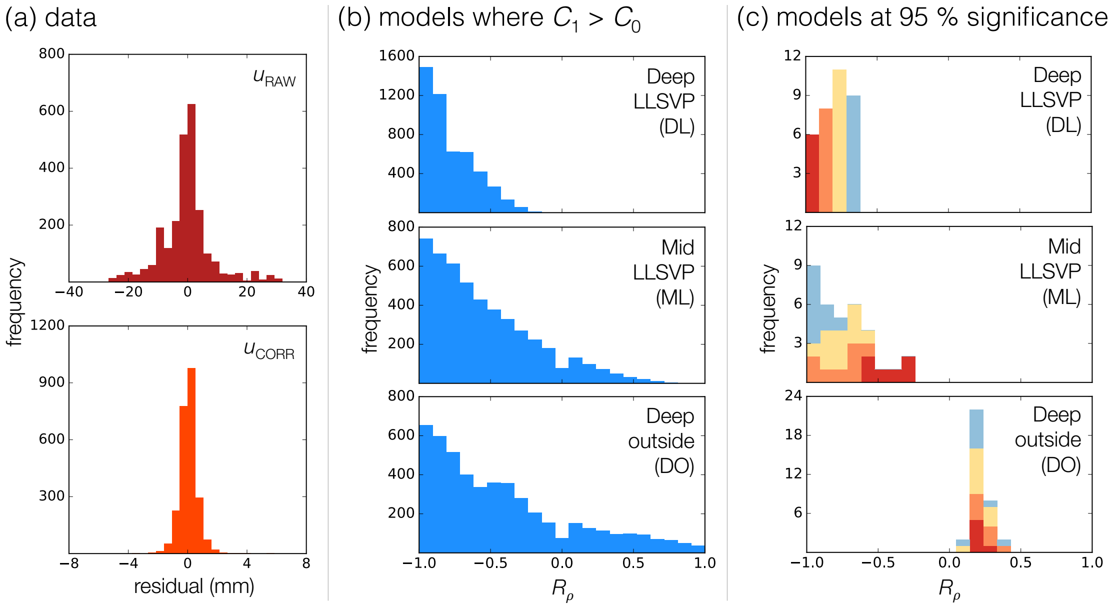

FIGURE 4.4: (a) Top panel shows the histogram of the GPS estimates of the in-phase M2 tidal response after correction for the signal computed from an Earth model with the 1-D elastic, density and anelastic structure of the PREM Q-model (Dziewonski & Anderson, 1981) (u_{RAW}, as defined in the main text). Bottom panel shows the data after applying corrections for the following effects: rotation, crustal and core-mantle boundary topography and ocean tidal loading (i.e., $u_{\mathrm{CORR}} = u_{\mathrm{RAW}} - u_{4\mathrm{C}}$ in the main text). (b) Histograms of parameters defining the set of 3-D Earth models which yield a correlation coefficient C_1 that exceeds C_0 (see main text). (c) Histograms of the subset of 3-D Earth models in (b) that improve the correlation at a 95% significance level. The colors discretize the range of R_ρ estimates in the top frame and these colors are used to group together subsets of 3-D Earth models common to all three frames in (c).

Note that the u_{ROT} correction was provided in Yuan et al. (2013), and u_{CMB} and u_{CT} have a net signal that is an order of magnitude smaller than the uncertainty in the body tide observations (see Fig. 4.5); (3) a final correction is applied for the response due to the ocean tidal load, u_{OTL}. This correction is performed by randomly drawing u_{OTL} values provided by seven global ocean tide models (see Section 4.4) with the same sampling frequency adopted in step (1). We will denote the sum of all four corrections listed above as $u_{4\mathrm{C}}$. A histogram of RMS residuals generated by correcting u_{RAW} for the signals $u_{4\mathrm{C}}$ (i.e., u_{CORR}, where $u_{\mathrm{CORR}} = u_{\mathrm{RAW}} - u_{4\mathrm{C}}$) is shown in Fig. 4.4(a) (bottom panel). The correction for the response to the ocean tidal load is by far the most important, and it leads to a significant reduction in the spread of the histograms (±35 mm for u_{RAW}

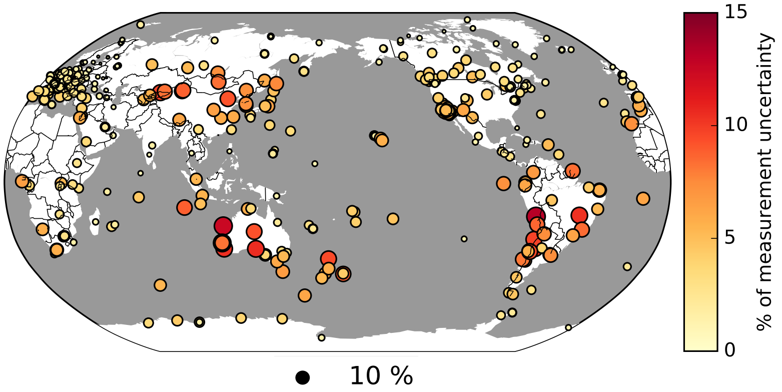

FIGURE 4.5: Crustal (Laske et al., 2013) and core-mantle boundary topography (Mathews et al., 2002) corrections to the body tide response (see Section 4.4) shown as a percentage of the measurement uncertainty in the GPS data (Yuan et al., 2013). The magnitude of the corrections is indicated by both the size and color intensity of the circles.

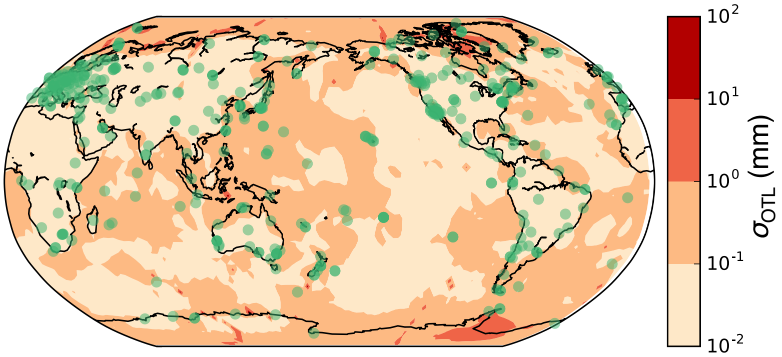

FIGURE 4.6: Standard deviation, σ, of a set of predictions of vertical crustal displacement associated with ocean loading, $u_{\rm OTL}$ computed using the seven ocean tide models described in the Section 4.4. The green circles mark the locations of the GPS sites use in our analysis.

to ±6 mm for $u_{\rm CORR}$), consistent with findings in Yuan et al. (2013). (We note that most errors in $u_{\rm OTL}$ are $<$ 1 mm, see Fig. 4.6). The next three steps in the procedure involve the calculation and assessment of correlations. In particular, we: (4) compute the correlation coefficient, C_0, between the two populations: $u_{\rm RAW}$ and $u_{\rm 4C}$; (5) calculate forward predictions of body tide displacement, $u_{\rm 3D}(i)$, for a given 3-D mantle structure model i (removing the contribution from the 1-D background model PREM; Dziewonski & Anderson, 1981) where we apply all possible combina-

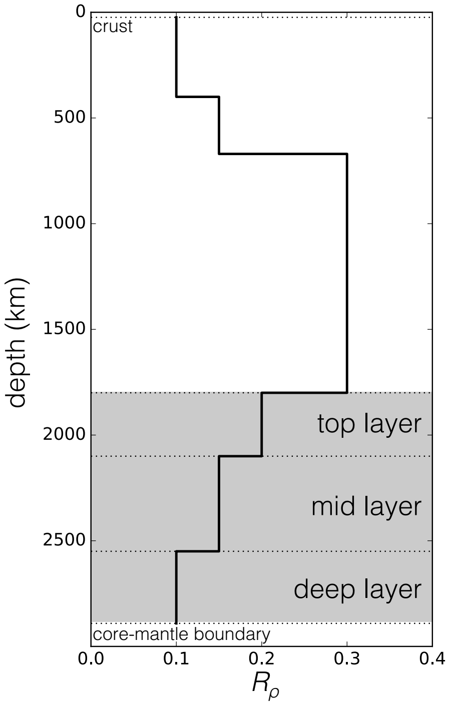

FIGURE 4.7: Radial dependence of the scaling factor, R_ρ, applied (within the shallowest three layers of our Earth models) to convert perturbations in shear wave speed v_s to perturbations in density ρ (Karato, 1993). The scaling factors within the lowest three regions (highlighted by shading) are treated as free parameters in the analyses described in the text.

tions of $R_\rho(= \delta v_s/\delta\rho)$ values in the range $-1 \leq R_\rho(\mathrm{DL}) \leq 1, -1 \leq R_\rho(\mathrm{ML}) \leq 1$, and $-1 \leq R_\rho(\mathrm{DO}) \leq 1$ (at increments of 0.05) to a v_s tomographic model randomly drawn from the five listed above. (For the rest of the mantle, we apply the depth-dependent scaling factor shown in Fig. 4.7 (Karato, 1993).) This exercise, which adopts the same sampling frequency at each site as in step (1), yields a set of $\sim 10^5$ forward predictions. For each forward prediction i, we calculate a new correlation coefficient, $C_1(i)$, between the populations u_{RAW} and $u_{4\mathrm{C}} + u_{3\mathrm{D}}(i)$, and pose the question: does the additional correction $u_{3\mathrm{D}}(i)$ result in a value of $C_1(i)$ for which $C_1(i) > C_0$? Fig. 4.4(b) shows the histogram of (randomly sampled) Earth models that meet this criterion; finally (6) we assess the statistical significance (see Section 4.4) of each of the models in Fig. 4.4(b). Fig. 4.4(c) shows the subset of models from Fig. 4.4(b) in which $C_1(i)$ exceeds C_0 at 95% confidence level. In this step, we additionally cull any models that perturb the mean density in any of the three layers by more than 0.5% from the 1-D background model.

4.3 Results and Discussion

Fig. 4.8(a) shows histograms of the mean excess density within the three mantle regions DL, ML and DO, computed using each of the solutions summarized in Fig. 4.4(c). The median excess densities on each histogram are +0.67%, +0.54% and −0.03%, with interquartile ranges of (+0.61–+0.74)%, (+0.44–+0.64)% and (−0.04––0.02)%, respectively. We conclude, on the basis of these GPS-based constraints on the M2 body tide, that the integrated excess density within the lowest ∼700 km of the LLSVPs has a median value of +0.60% and an interquartile range of (+0.56–+0.62)%. This result indicates that high-density chemical components within these deep, large-scale mantle regions dominate thermal effects in establishing the integrated buoyancy of the LLSVPs. An example of the inferred density field within the 'deep' mantle layer derived from one of the models in Fig. 4.4(c), with R_ρ values of (DL) 0.82, (ML) 0.76, and (DO) 0.20, applied to seismic tomographic model S40RTS (Ritsema et al., 2011), is shown in Fig. 4.8(b).

Supporting evidence for the existence of compositional heterogeneity within the mantle comes from a variety of sources, including geochemical analyses of mantle-derived rocks (Hofmann, 1997), where potential sources of different chemical reservoirs include subducted oceanic lithosphere (Christensen & Hofmann, 1994), unprocessed mantle material (i.e., mantle untouched by melt extraction at the surface) (Allègre et al., 1996), and residual material from a differentiation event early in Earth's history (Kellogg et al., 1999). Numerical simulations of thermochemical mantle convection indicate that relatively dense compositional heterogeneity may be naturally collected within deep mantle regions, or piles (Tackley, 1998), and that the morphology of such regions is consistent with LLSVP geometries when realistic plate subduction histories are incorporated into the modeling (Davies et al., 2012; McNamara & Zhong, 2005). Laboratory experiments exploring convection

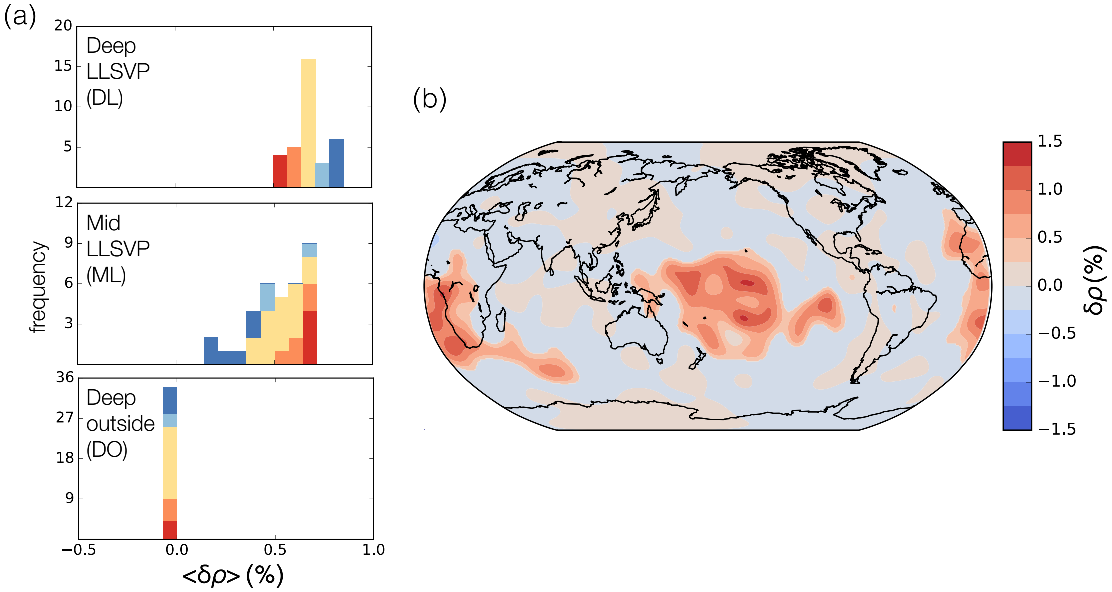

Figure 4.8: (a) Histograms of the mean excess density ($\langle\delta\rho\rangle$) in each region for the models shown in Fig. 4.4(c). The colors discretize the range of $\langle\delta\rho\rangle$ estimates in the top frame and they are used to group together subsets of the 3-D Earth models common to all three frames. Note that the colors here are unrelated to those in Fig. 4.4(c). (b) The density field across the deepest mantle layer (extending to 350 km above the CMB) computed by applying the mean values of R_ρ(DL) and R_ρ(DO) in the top and bottom panels of Fig. 4.4(c) to the shear wave tomography model S40RTS (Ritsema et al., 2011).

in a chemically stratified mantle suggest that the LLSVPs may instead reflect a doming regime active for density contrasts less than 1% (Davaille, 1999), a value consistent with our derived bounds on the excess density in these structures (Fig. 4.8a). These bounds are also consistent with numerical "mixing" experiments (Nakagawa & Tackley, 2004; Brandenburg et al., 2008) that indicate that excess densities of order 1% are required to preserve chemical heterogeneity over billion year time-scales.

A global inversion of seismic normal mode splitting data, augmented by geodynamic modeling of long-wavelength free-air gravity anomalies (Ishii & Tromp, 1999), inferred an anti-correlation between v_s and ρ (i.e., negative R_ρ values) at the base of the mantle. The spatial resolution of such studies was subsequently questioned (Kuo & Romanowicz, 2002). However, a recent inversion of a large database of seismic records, including updated normal splitting functions, surface wave phase anomalies, body wave travel times, and long-period waveforms, inferred a $\sim$1% excess density at the base of the mantle, roughly coincident with the location of the LLSVPs, consistent with the results in Ishii & Tromp (1999). Nevertheless, we note that the adoption of the self-coupling approximation of normal mode theory in both these seismic studies may introduce inaccuracies in the inference of structure Deuss & Woodhouse (2001); Al-Attar et al. (2012); Yang & Tromp (2015). (Our methodology does not adopt the self-coupling approximation; see Section 4.4 for a more detailed discussion.) Many seismological studies (Masters et al., 2000; Su & Dziewonski, 1997) also report anti-correlation between v_b and v_s within the LLSVPs, a result that implies compositional heterogeneity (Karato & Karki, 2001). Moreover, an analysis of a set of SKS phases traversing the eastern flank of the African LLSVP has suggested that this boundary has a relatively sharp ($\sim$50 km) gradient in wave speed, consistent with a dense chemical layer bordered by an upwelling thermal structure (Ni et al., 2002; Sun et al., 2007).

Notwithstanding the above studies, the relative role of chemistry and temperature on the buoyancy of the LLSVPs has been a source of significant debate. As an example, a combined analysis of seismic, geodynamic and mineral physics data within the framework of viscous flow modeling concluded that while the LLSVPs are characterized by compositional heterogeneity relative to the surrounding mantle, they are, in bulk, buoyant and actively upwellings (Forte & Mitrovica, 2001). In addition, recent thermochemical flow modeling by Davies et al. (2012) has suggested that many seismic observations used to argue that LLSVPs are denser than the surrounding mantle—this includes the anti-correlation between v_b and v_s within the LLSVPs, the sharp gradient in shear wave speed at the edge of the African LLSVP, the large amplitude of the shear wave speed anomaly and high ratio of shear-to-compressional wave speed within the structures (Karato & Karki, 2001; Brodholt et al., 2007)— are consistent with a model in which the LLSVPs are buoyant structures. In particular, it is possible that the anti-correlation between v_b and v_s may reflect the existence of a post-perovskite phase (Murakami et al., 2004; Wookey et al., 2005) at the base of the LLSVPs and that the large amplitudes and gradients in v_S may be explained by considering the effects of temperature and pressure dependent anelasticity (Karato, 1993).

While these arguments do indicate non-uniqueness in the inference of compositional heterogeneity within the deep mantle, they cannot explain our inferred anti-correlation between v_S and ρ (Karato & Karki, 2001) (Fig. 4.4c) and thus our conclusion that the LLSVPs are, on average, denser than the surrounding mantle is robust. Future work in developing tidal tomography, including the incorporation of seismic measurements of body tides and the analysis of other (diurnal and long-period) tidal bands, will refine our bounds on buoyancy within the Earth's deep mantle, and thus further improve our understanding of mantle flow and its role in the evolution of the Earth system.

4.4 METHODOLOGICAL DETAILS

4.4.1 FORWARD MODELING OF BODY TIDES

To predict the semi-diurnal body tide response we use a fully-coupled normal mode perturbation theory that accounts for the effects of rotation, topography on discontinuities, laterally varying elastic/anelastic and density structure (Chapter 2; Lau et al., 2015). Note that the full coupling of normal modes is distinct from the approach adopted in previous seismic data analyses, which have invoked approximate methods of normal mode coupling (Ishii & Tromp, 1999; Moulik & Ekström, 2016). The self-coupling approximation, in particular, significantly degrades the accuracy of predictions of the body tide response (Chapter 2; Lau et al., 2015); similar concerns regarding accuracy have been raised in the application of self-coupling to the seismic normal mode problem (Deuss & Woodhouse, 2001; Al-Attar et al., 2012; Yang & Tromp, 2015).

Our methodology adopts the normal modes of a 1-D Earth (PREM; Dziewonski & Anderson, 1981) as a basis set, and, in the presence of the effects listed above, calculates the coupling between these modes. After considering many synthetic tests, we have chosen to fully couple the following

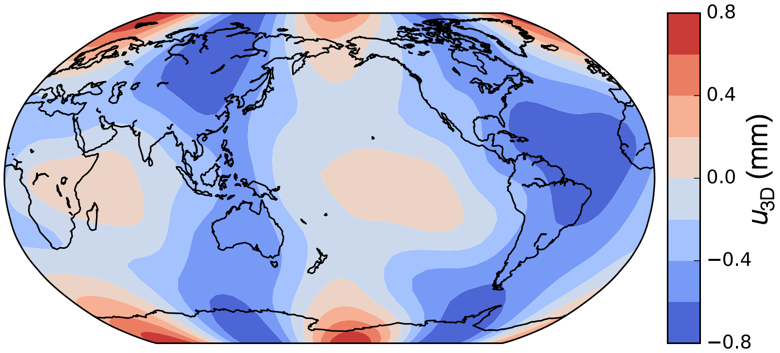

FIGURE 4.9: Difference in the amplitude of the in-phase vertical displacement of the semi-diurnal body tide predicted using 3-D and 1-D Earth models. The underlying mantle structure is that of S40RTS (Ritsema et al., 2011), scaled to perturbations in bulk sound speed v_b (as discussed in text) and to perturbations in ρ by applying scaling factors shown in Fig. 4.7.

set of modes: $\{{}_0\mathcal{S}_2, {}_2\mathcal{S}_1, {}_0\mathcal{S}_3, {}_0\mathcal{S}_4, {}_1\mathcal{S}_2, {}_0\mathcal{S}_0, {}_0\mathcal{S}_5, {}_1\mathcal{S}_3, {}_2\mathcal{S}_2, {}_0\mathcal{S}_6, {}_3\mathcal{S}_2, {}_1\mathcal{S}_4, {}_2\mathcal{S}_3, {}_2\mathcal{S}_4, {}_1\mathcal{S}_0, {}_4\mathcal{S}_2\}$. We note that other modes, including toroidal modes, have a minor and undetectable effect on the vertical component of the body tide response. An example of a prediction of the M2 body tide response is provided in Fig. 4.9. The figure shows the residual (3-D minus 1-D) amplitude of the in-phase (with respect to the tidal potential) vertical displacement. This particular calculation adopts the v_s tomographic model S40RTS (Ritsema et al., 2011). Density perturbations are prescribed by applying the depth-dependent scaling shown in Fig. 4.7 (Karato, 1993) and perturbations in bulk sound speed are computed from the shear wave model using a fixed value of R_b of 0.05 (Masters et al., 2000).

In analogy to the seismic normal mode problem, the sensitivity of body tide predictions to lateral variations in structure is most significant for perturbations characterized by even spherical harmonic degrees. Fig. 4.10 shows, across our full suite of 3-D Earth models, the power spectrum of the density field within the deepest layer, DL. Each bar represents the largest contribution at a given spherical harmonic degree across all our models, normalized by the largest value across all spherical harmonic degrees. A dominant signal is evident at spherical harmonic degree 2. This result, combined with the even-degree sensitivity described above and the spherical harmonic degree 2 (sectorial) ge-

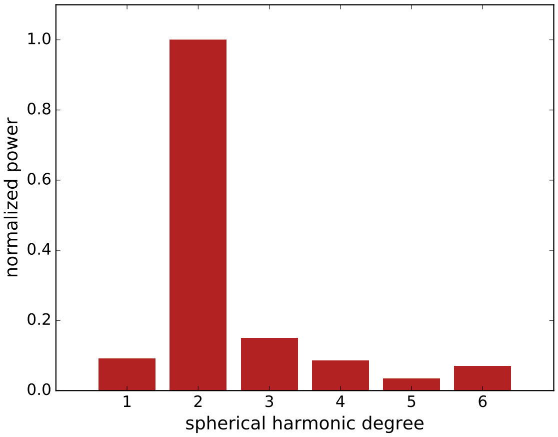

FIGURE 4.10: A combined power spectrum of the density field of the deep layer, DL, across the entire suite of 3-D models tested. Each bar represents the maximum power across all models at the associated spherical harmonic degree. The values on the histogram are normalized using the maximum power across all models and all degrees (which occurs at spherical harmonic degree 2).

ometry of the semi-diurnal forcing, indicates that body tide observations are particularly well suited to constraining the long-wavelength structure of the Earth's deep mantle.

4.4.2 DATA PROCESSING

We use a published data set comprised of Earth's in- and out-of-phase crustal deformation associated with several semi-diurnal and diurnal tidal constituents (Yuan et al., 2013), as measured by 456 globally-distributed GPS stations (Fig. 4.1). Our analysis uses only the in-phase vertical component of the M2 body tide, the largest semi-diurnal tidal constituent, and GPS-based estimates are corrected for the following effects: (1) rotation of the Earth (which is already applied in Yuan et al., 2013); (2) crustal topography using the crustal model CRUST1.0 (Laske et al., 2013); and (3) the excess ellipticity of the core-mantle boundary (Mathews et al., 2002). Although core-mantle boundary topography is uncertain (Koelemeijer et al., 2012), the excess ellipticity component of this topography is accurately known (Mathews et al., 2002). Nevertheless, Fig. 4.5 demonstrates that the GPS-derived body tide data set is insensitive to the excess-ellipticity and crustal topography relative to the uncertainty of the GPS measurements. Corrections (2) and (3) are applied using the normal mode perturbation theory (Lau et al., 2015) described in the last section. Finally, all values of u_{RAW} considered in the analysis are residuals, and so are corrected for the background 1-D elastic, density and anelastic structure of the Earth, as described in Yuan et al. (2013). All observations and predictions are taken relative to a reference site located in Williams Lake, Canada (we chose this site due to its very small observational uncertainty).

As we have noted, the focus of this study is the 3-D elastic and density structure of the Earth. The question arises as to the possible sensitivity of our results to Earth's 3-D Q structure. Very little is known in regard to this structure. 1-D anelasticity has a $\sim 1\%$ effect on the in-phase response of the body tide (Wahr & Bergen, 1986). 3-D anelasticity is likely to introduce an order $\sim$ 1% perturbation to this signal (i.e., $\sim 0.01\%$ overall). We conclude that 3-D anelasticity will produce an in-phase signal that is an order of magnitude beneath the level of detection of our data. The impact of 3-D anelasticity on the out-of-phase component of the body tide response will be much larger and for this reason the present analysis considers only the in-phase component of the M2 tidal constituent.

4.4.3 OCEAN TIDAL LOADING

In order to isolate the signature of 3-D mantle elastic and density structure, the final effect to be removed from the GPS estimates is the deformation associated with M2 ocean tidal loading, which has the same frequency as the M2 body tide. As part of our statistical tests, we considered u_{OTL} calculated from seven global ocean tidal models (NAO99, Matsumoto et al. (2000); FES2004, Lyard et al. (2006); TPX2010, Egbert et al. (2002); DTU, Cheng & Andersen (2010); EOT, Savcenko & Bosch (2012); HAMTIDE, Taguchi, E. & Zahel (2010)) and randomly sample from these. To calculate the deformation signal, u_{OTL}, associated with each of these models, we adopt PREM (Dziewonski & Anderson, 1981) (both the continental and oceanic lithosphere versions) and use the software package SPOTL (Agnew, 1997). We do not consider the impact of 3-D structure on the ocean tide response for two reasons: (1) the implementation of a correction based on 3-D structure would be difficult due to the high resolution that is required at coastlines in order to accurately compute these effects; and (2) the ocean tidal loading signal is primarily sensitive to structure in the uppermost upper mantle (Ito & Simons, 2011), which, as demonstrated by Fig. 4.2, has little impact on the body tide response. Hence, any deep mantle 3-D structure we adopt in our analysis of the body tide will have negligible effect on the ocean tidal response. The effect of shallow 3-D structure is accounted for by implementing the different versions of upper mantle PREM structure in the SPOTL software. We also note that the standard deviation in the ocean tidal loading correction across the seven ocean tidal models is relatively low at most of the sites used in this study (see Fig. 4.6).

STATISTICAL TESTS

The expanded data set required for our statistical tests is constructed by randomly sampling GPS estimates at each site (accounting for Gaussian errors in these estimates; Yuan et al., 2013) with a frequency proportional to a site's cumulative squared distance from other sites. We normalize this number such that the maximum number of samples for any site is 10,000. This approach results in a data set of 2,457,122 measurements with a mean sampling number of 5388. We note that in the test for correlations described below we remove outliers that can only be explained by unmodeled noise. This results in the removal of $\sim$ 4% of the total data set.

As we note in the text, we compute the correlation, C_0, between the raw GPS data set u_{RAW} and the set of corrections for Earth rotation, core-mantle boundary and crustal topographies, and ocean tidal loading (which sum to $u_{4\mathrm{C}}$; see main text). We then add an additional correction for the signal due to 3-D elastic and density structure and re-compute the correlation, C_1. By considering a large number of 3-D Earth models we derive the set $C_1(i)$ and retain only those models for which $C_1(i) > C_0$. We can denote this smaller set as $C_1(i^*)$.

In the event that the GPS-based estimates from each sampled set were uncorrelated, establish-

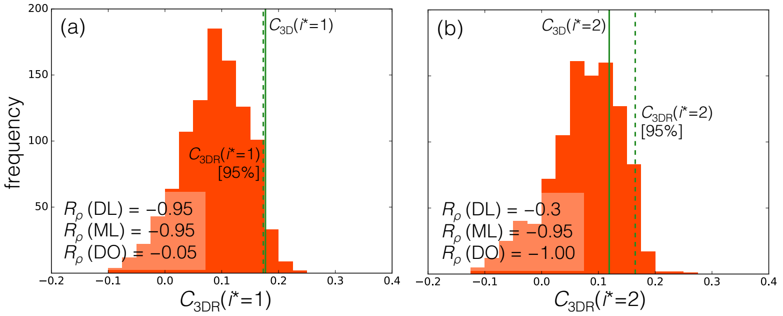

FIGURE 4.11: Testing the significance level of two different 3-D Earth models ($i^* = 1$ and 2) for which $C_1(i^*) > C_0$ (as defined in the text). Each panel corresponds to a different 3-D Earth model (constructed with the R_ρ values listed in the inset) and shows the histogram of $C_{\mathrm{3DR}}(i^*, j = 1, 2, .., 1000)$ values produced by rotating the predicted field (see Section 4.4). The dashed green line shows the 95% level of these histograms and the solid green line shows $C_{\mathrm{3D}}(i^*)$ for the given 3-D Earth model. In (a), $C_{\mathrm{3D}}(i^* = 1)$ exceeds the 95% confidence level and thus passes the significance test; in contrast, (b) $C_{\mathrm{3D}}(i^* = 2)$ fails this test.

ing the statistical significance of the difference between a given C_1 in the set $C_1(i^*)$ and C_0 would involve a standard statistical test (e.g., the t-test). However, this is not the case in our analysis. Accordingly, to assess statistical significance we adopt the following approach. For each model that improves C_0, i.e., the set i^* of all 3-D models and their associated predicted body tide displacements $u_{\mathrm{3D}}(i^*)$, we perform 1000 random rotations of the predicted body tide displacement field of that model. For each rotation (which we denote by the index j) we sample the field at the location of the GPS sites, yielding $u_{\mathrm{3DR}}(i^*, j)$. Then, for a given 3-D Earth model in the set i^*, we calculate a new correlation coefficient, $C_{\mathrm{3DR}}(i^*, j)$, between the two populations $u_{\mathrm{CORR}} (= u_{\mathrm{RAW}} - u_{\mathrm{4C}})$ and $u_{\mathrm{3DR}}(i^*, j)$, resulting in different 1000 values of $C_{\mathrm{3DR}}(i^*, j = 1, 2, .., 1000)$. This random distribution serves as our null hypothesis. We then calculate a single correlation coefficient, $C_{\mathrm{3D}}(i^*)$, between the following populations u_{CORR} and $u_{\mathrm{3D}}(i^*)$. We consider a model $u_{\mathrm{3D}}(i^*)$ to be statistically significant at the percentile it lies within the distribution of $C_{\mathrm{3DR}}(i^*, j = 1, 2, .., 1000)$. Fig. 4.11 provides two examples of the application of this test, one in which a model reaches the 95% significance level and one where it does not. In the successful case, the geographical variation of the displacement field shows a level of coherence with respect to the GPS-based measurements beyond that which can be explained by merely reproducing the spatial wavelengths captured by observation.

5

Inferences of Mantle Viscosity Based on Ice Age Data Sets: Radial Structure

> *Many years later, as he faced the firing squad, Colonel Aureliano Buendía was to remember that distant afternoon when his father took him to discover ice.*
>
> –G.G. Marquez

5.1 INTRODUCTION

The viscosity structure of the Earth's mantle, as inferred from data related to glacial isostatic adjustment (hereafter GIA), has been a source of debate spanning decades, with consensus oscillating between arguments for a significant increase in (spherically averaged) viscosity with depth from the

---

A version of this chapter was published with Jerry X. Mitrovica, Jacqueline Austermann, Ophelia Crawford, David Al-Attar, Konstantin Latychev in *Journal of Geophysical Research: Solid Earth*, vol. 121, p. 6991-7012, 2016.

base of the lithosphere to the deep mantle (e.g., McConnell, 1968; O'Connell, 1971), to suggestions of an essentially isoviscous mantle (e.g., Cathles, 1975; Peltier, 1976; Wu & Peltier, 1983, 1984; Tushingham & Peltier, 1992), and back again (e.g., Nakada & Lambeck, 1989; Mitrovica, 1996). The latter studies were broadly consistent with independent inferences based on viscous flow modeling of surface observables associated with mantle convection (e.g., Ricard et al., 1984; Richards & Hager, 1984; Forte, 1987; Hager & Richards, 1989; King & Masters, 1992), which favor viscosity profiles that increase 1–2 orders of magnitude from the base of the lithosphere to the core-mantle-boundary (CMB). This apparent reconciliation weakened arguments for a transient (i.e., time-scale dependent) mantle viscosity (Sabadini et al., 1985; Peltier et al., 1986) and was supported by two other lines of study. First, joint inversions of data associated with GIA and mantle convection yielded simultaneous fits to both data sets and viscosity profiles that were characterized by a significant (several order of magnitude) increase of viscosity with depth (Forte & Mitrovica, 1996; Mitrovica & Forte, 1997, 2004; Kaufmann & Lambeck, 2002). Second, a reanalysis of GIA-based inferences of an isoviscous mantle demonstrated that many such studies had misinterpreted the so-called Haskell number (10^{21} Pa s) (Haskell, 1935) as a constraint on the bulk average viscosity above 670 km depth (the modern definition of the upper mantle) rather than the average above $\sim$1200 km depth, as indicated by a resolving power analysis of the Fennoscandian sea-level record that the Haskell number was based upon (Mitrovica, 1996). This misinterpretation biased these inferences toward a lower mantle viscosity of 10^{21} Pa s and isoviscous mantle models. However, while more recent GIA-based estimates of mantle viscosity are no longer tied to bulk upper mantle values of 10^{21} Pa s (Peltier, 2004), there remain significant apparent differences between such inferences, particularly within the lower mantle (e.g., Argus et al., 2014; Nakada et al., 2015a), where discrepancies continue to exceed an order of magnitude. One goal of the present study is to understand the origin of these differences.

A major complication in GIA-based studies of mantle viscosity is the strong sensitivity of most ice age related observations to the space-time history of ice cover, and the most rigorous analyses have sought parameterizations of the data that reduce this sensitivity. These parameterizations include the strandline-derived Fennoscandian relaxation spectrum (FRS) (e.g., McConnell, 1968; Mitrovica & Peltier, 1993a; Wieczerkowski et al., 1999; Peltier, 2004), relaxation times estimated from the post-glacial uplift of previously glaciated regions (e.g., Mitrovica & Peltier, 1995; Mitrovica, 1996; Mitrovica & Forte, 1997; Peltier, 1998a; Mitrovica et al., 2000; Nordman et al., 2015) and differential Late Holocene sea-level highstands from sites in the far-field of ice cover (Nakada & Lambeck, 1989). Resolving power analyses indicate that the FRS and post-glacial decay times from Fennoscandia are sensitive to viscosity variations to a depth of $\sim$1200 km (Parsons, 1972; Mitrovica & Peltier, 1993a; Mitrovica, 1996), while decay times from Hudson Bay, a region covered by the massive Laurentide Ice Sheet, are sensitive to viscosity to a depth of $\sim$1600 km (Mitrovica, 1996). As a consequence, analyses based upon these data sets do not constrain viscosity in the bottom half of the mantle (e.g., McConnell, 1968; Mitrovica & Peltier, 1993a, 1995; Mitrovica, 1996; Peltier, 1998a; Wieczerkowski et al., 1999). One way to extend the sensitivity to the CMB is to augment the analysis with long-wavelength observables related to mantle convection (Forte & Mitrovica, 1996; Mitrovica & Forte, 1997, 2004). Differential sea-level highstands, since they reflect, in part, the response to large-scale ocean loading (Nakada & Lambeck, 1989), have a non-zero sensitivity to viscosity that extends to the CMB; however, these data are also sensitive to shallower, upper mantle structure (Kendall & Mitrovica, 2007).

In the 1980s and 1990s, a number of GIA analyses incorporated satellite-derived estimates of the rate of change of low degree zonal harmonics of the Earth's geopotential into inferences of mantle viscosity, and in particular $\dot{J}_2$ (Yoder et al., 1983; Rubincam, 1984; Wu & Peltier, 1984; Peltier, 1985; Yuen & Sabadini, 1985; Mitrovica & Peltier, 1989; Vermeersen et al., 1998). While this effort stalled with the growing recognition that these harmonics were sensitive to ongoing ice mass variations (e.g., Sabadini et al., 1988; Peltier, 1988; Ivins et al., 1993; Mitrovica & Peltier, 1993a; Peltier, 1998b), the deep mantle sensitivity provided by the $\dot{J}_2$ observation (Mitrovica & Peltier, 1993a; Peltier, 1998b; Morrow et al., 2013) has continued to make it a focus of GIA research. In this regard, recent GIA analyses have followed two approaches. In the first, Peltier and colleagues (Peltier, 2004; Argus et al., 2014; Peltier et al., 2015) have used the datum to constrain deep mantle viscosity under the assumption that melting of ice sheets and glaciers had negligible impact on the $\dot{J}_2$ signal estimated from the analysis of satellite altimeter records prior to ~1990 ($\sim -3 \times 10^{-11}$ y^{-1}). The VM2 and VM5a viscosity profiles (Peltier, 2004; Argus et al., 2014, respectively) are characterized by a deep mantle value of $\sim 3 \times 10^{21}$ Pa s. In contrast, Nakada et al. (2015a) and later Mitrovica et al. (2015) infer deep mantle viscosity using the pre-1990 $\dot{J}_2$ datum after correction for an ice melt signal based on a tabulation of glacier mass flux appearing in the Fifth Assessment Report of the Intergovernmental Panel on Climate Change (IPCC) (Vaughan et al., 2013). Both these studies argued for a deep mantle viscosity in excess of 10^{22} Pa s.

In this study we return, once more, to the inverse problem for mantle viscosity. In particular, we perform, for the first time, joint nonlinear inversions of GIA data sets, including the FRS, decay times determined from local sea-level curves in Fennsocandia and Hudson Bay, differential sea-level highstands and $\dot{J}_2$. In regard to the last of these, we explore the sensitivity of the inversions to the correction of the pre-1990 trend for the signal due to glacier and ice sheet mass flux. As noted above, one overarching goal is to understand the nature and significance of the major inconsistencies in recently published GIA-based inferences of mantle viscosity (Argus et al., 2014; Peltier et al., 2015; Nakada et al., 2015a). Specifically, we explore whether these differences are significant given the finite resolving power of the GIA data sets and, if so, whether particular data sets are responsible for the discrepancy. The analysis herein serves as a comprehensive study of the information content in these classical data sets of GIA used to infer the radial profile of mantle viscosity. Discrepancies in the above inferences may also arise from lateral heterogeneities in viscoelastic structure. In a companion study we use synthetic calculations of GIA on a 3-D, viscoelastic Earth model to assess the level of bias introduced into our inversions by our neglect of lateral viscosity structure.

5.2 METHODOLOGY

5.2.1 THE FORWARD PROBLEM

We are concerned with four distinct observables: (1) the Fennoscandian relaxation spectrum; (2) decay times from relative sea-level (uplift) curves near the center of the ancient Laurentian and Fennoscandian Ice Sheets; (3) $\dot{J}_2$; and (4) differential sea-level highstands. In the following, we briefly summarize forward calculations associated with each. All calculations adopt spherically-symmetric, (Maxwell) viscoelastic and self-gravitating Earth models. The elastic and density structure of all models is given by the seismic model PREM (Dziewonski & Anderson, 1981). Unless otherwise specified, for all calculations that involve a space-time history of ice cover, we adopt the ice model ICE-6G (Argus et al., 2014; Peltier et al., 2015).

THE RELAXATION SPECTRUM

Following Peltier (1974), viscoelastic load (or tidal-effective) Love numbers can be written in the following general, impulse response form:

$$\chi_\ell(t) = \chi_\ell^E \delta(t) + \sum_{n=1}^{N} r_n^\ell \exp(-s_n^\ell t)\,, \tag{5.1}$$

where the time-dependent Love number, $\chi_\ell(t)$ at spherical harmonic degree ℓ, is decomposed into an immediate elastic response, χ_ℓ^E, followed by viscoelastic relaxation governed by N normal modes of exponential decay. Each normal mode is prescribed by an amplitude r_n^ℓ and inverse decay time, or eigenfrequency, s_n^ℓ, and these are functions of the density, elastic and viscosity structure of the adopted Earth model (Peltier, 1974; Wu, 1978). The collection of s_n^ℓ forms the relaxation spectrum for a given viscoelastic Earth model.

We compute the relaxation spectrum using the approach described by Peltier (1974). As discussed below, the Fennoscandian relaxation spectrum (FRS) determined from geological records of sea-level change is defined by a single, best-fitting decay time at each harmonic degree above 10 in a strandline deformation field. Forward calculations of the relaxation spectrum indicate that above degree 10 the response is dominated by the fundamental "M0" mode of relaxation and synthetic tests indicate that neglecting other modes of relaxation in forward predictions does not introduce significant error into the analysis of the observed spectrum (Wieczerkowski et al., 1999). As a consequence, in computing the relaxation spectrum we limit ourselves to the fundamental mode and, for simplicity, we drop the subscript n when refering to the FRS spectrum, s_ℓ.

POST-GLACIAL DECAY TIMES

Post-glacial decay times are computed in two steps. First, we solve the sea-level equation derived by Mitrovica & Milne (2003) using the pseudo-spectral algorithm outlined in Kendall et al. (2005) with a truncation at spherical harmonic degree and order 256. This gravitationally self-consistent treatment incorporates the migration of shorelines and the signal in sea level due to perturbations in Earth rotation, and it requires, as input, a viscoelastic Earth model and an ice history. Upon output, the calculation yields sea-level (SL) changes over time at any site $\mathbf{r}$ relative to sea level at present (t_P), i.e., relative sea level (RSL):

$$\mathrm{RSL}(\mathbf{r}, t) = \mathrm{SL}(\mathbf{r}, t) - \mathrm{SL}(\mathbf{r}, t_\mathrm{P}). \tag{5.2}$$

We note that sea level in this context is defined as the height of the sea surface equipotential, which is globally defined, relative to the solid surface.

It has long been understood that RSL curves at sites near the center of ancient ice sheets (e.g., Hudson Bay) are characterized by an exponential decay given by the form (Walcott, 1972):

$$\mathrm{RSL}(\mathbf{r}, t) \approx A(\mathbf{r}) \left[\exp\{t/\lambda\} - 1 \right], \tag{5.3}$$

during periods when no ice remains in the vicinity of the site (i.e., the uplift is in so-called free decay). While the amplitude A is a strong function of both the Earth model and the ice history, the decay time λ is much less sensitive to the ice history (e.g., Mitrovica & Peltier, 1995; Mitrovica et al., 2000; Nordman et al., 2015). Our forward prediction of the post-glacial decay time for a specific site $\mathbf{r}$ is based on finding the best-fit function of the form (5.3) through the RSL curve calculated using the full sea-level theory described above.

$\dot{J}_2$

The coefficient J_2, the dynamical form factor, is a measure of the oblateness of the Earth's geoid. Specifically, it may be expressed as the suitably normalized spherical harmonic degree two and order zero coefficient in a spherical harmonic decomposition of the geopotential. As noted above, the calculation of gravitationally self-consistent sea-level changes naturally yields a determination of changes in both bounding surfaces of sea level: the sea surface, which is constrained to remain an equipotential, and the solid surface. The J_2 coefficient, and its rate of change, $\dot{J}_2$, may then be trivially determined from a time series of the degree two zonal harmonic of the sea surface height (or the geoid). Details of this mapping are given in Mitrovica & Peltier (1993a). Predictions of $\dot{J}_2$ are sensitive to the total change in ice volume from the Last Glacial Maximum to the end of the deglaciation phase but not to the detailed geometry of the ice cover (Wu & Peltier, 1984)

DIFFERENTIAL SEA-LEVEL HIGHSTANDS

In the far-field of ice cover, relative sea-level histories are commonly characterized by a fall in sea level of several meters during the current interglacial. The physics of this sea-level fall, which follows the rapid sea-level rise associated with the global deglaciation, is well understood (e.g., Nakada & Lambeck, 1989; Mitrovica & Peltier, 1991; Mitrovica & Milne, 2003; Lambeck et al., 2012), and it reflects the combined impact of: (1) continental levering, the tilting of the crust at shorelines driven by ocean loading; and (2) ocean syphoning, the migration of water from far-field shorelines to fill acommodation space created by the subsidence of the peripheral bulges that encircle the areas of ancient ice cover and offshore areas experiencing continental levering. The sea-level fall produces a RSL highstand that dates to the time when major melting ceased. If the age of the far-field highstand record at site $\mathbf{r}_1$ is t_1 and at site $\mathbf{r}_2$ is t_2, then the differential sea-level (DSL) highstand between these two sites is defined as:

$$\mathrm{DSL}_{1,2} = \mathrm{RSL}(\mathbf{r}_2, t_2) - \mathrm{RSL}(\mathbf{r}_1, t_1). \tag{5.4}$$

Calculating the DSL for any pair of sites is straightforward using the output of the ice age sea-level calculation described in Section 5.2.1. By taking the difference of the two sites within reasonably close proximity it is thought that the dependence on ice history is significantly reduced (Nakada & Lambeck, 1989).

5.2.2 THE INVERSE PROBLEM

The data considered in this study, the Fennoscandian relaxation spectrum, post-glacial decay times, the $\dot{J}_2$ harmonic and far-field differential sea-level highstands, are all nonlinear functions of the radial viscosity profile adopted in the forward calculations. That is, the Fréchet, or sensitivity kernels associated with these data are themselves functions of the viscosity profile. As such, our inversions adopt a nonlinear Bayesian methodology (Tarantola & Valette, 1982; Backus, 1988) in which constraints provided by any observations are combined with an *a priori* probability distribution to produce an *a posteriori* estimate of the radial viscosity profile. If we assume that any prior information and observational errors are Gaussian, then the maximum likelihood estimate of the posterior distribution may be found by solving the following iterative algorithm (Tarantola & Valette, 1982):

$$\hat{\mathbf{X}}_{k+1} = \hat{\mathbf{X}}_k + \left(\mathbf{F}_k^T \mathbf{V}_\xi^{-1} \mathbf{F}_k + \mathbf{V}_{\text{PR}}^{-1}\right)^{-1} \times \left\{\mathbf{F}_k^T \mathbf{V}_\xi^{-1} \left(\mathbf{y} - f(\hat{\mathbf{X}}_k)\right) - \mathbf{V}_{\text{PR}}^{-1} \left(\hat{\mathbf{X}}_k - \mathbf{X}_{\text{PR}}\right)\right\}, \tag{5.5}$$

where $\hat{\mathbf{X}}_k$ is the k-th model iterate, $\mathbf{F}_k$ is a matrix whose rows are the discretized form of the Fréchet kernels (i.e., partial derivatives) associated with $\hat{\mathbf{X}}_k$, $\mathbf{V}_\xi$ is the covariance matrix of the data errors (with zero mean), $\mathbf{X}_{\text{PR}}$ and $\mathbf{V}_{\text{PR}}$ are the prior model and covariance matrix, $\mathbf{y}$ is the observational data vector and $f(\hat{\mathbf{X}}_k)$ is a forward prediction of the data vector based on model $\hat{\mathbf{X}}_k$. Since the problem is nonlinear, tests must be performed to ensure that the converged solution is not sensitive to the prior or starting model on spatial scales resolved by the data (see below).

Following earlier work (Mitrovica & Peltier, 1995; Mitrovica, 1996; Mitrovica & Forte, 2004), we parameterize the model in terms of the logarithm of the viscosity profile $\log \nu(r)$, where r is the radius, in some discretized form. In this case, the inverse problem is rendered weakly nonlinear and the *a posteriori* covariance matrix of the model, $\mathbf{V}_{\text{PO}}$, may be approximated as (Tarantola & Valette, 1982; Backus, 1988):

$$\mathbf{V}_{\text{PO}} \approx \left[\mathbf{F}^T \mathbf{V}_\xi^{-1} \mathbf{F} + \mathbf{V}_{\text{PR}}^{-1}\right]^{-1}, \tag{5.6}$$

where $\mathbf{F}$ is the matrix of Fréchet kernels computed using the final model iterate. Using the $\log \nu(r)$

parameterization, we define the Fréchet kernel for a given datum y_i, $F_i(\log \nu, r)$, by the relation:

$$\delta \log y_i = \int_{\mathrm{CMB}}^{\mathrm{LAB}} F_i(\log \nu, r)\, \delta \log \nu(r)\, r^2 \mathrm{d}r, \tag{5.7}$$

where CMB and LAB are the radii of the core-mantle boundary and the lithosphere-asthenosphere boundary (or the base of the lithosphere), respectively (Mitrovica & Peltier, 1995).

In the case of forward predictions of the relaxation spectrum, Peltier (1976), following Parsons (1972), derived analytical expressions for the kernels F_i, and we adopt these expressions. For predictions of $\dot{J}_2$, post-glacial decay times and DSL highstands, we compute the Fréchet kernels using the numerical perturbation procedure described by Mitrovica & Peltier (1993a). In this case we discretize the radial viscosity profile (and the Fréchet kernels) into 28 layers, 13 in the upper mantle and 15 in the lower mantle. By choosing a discretization that is much finer than the resolving power of the data (see below) variations in the inverted viscosity profile will have a spatial scale that reflects the resolving power, not the model discretization. Inverse or forward analysis based on a much smaller number of layers (e.g., isoviscous, upper and lower mantle) may significantly misrepresent the information content of the data and lead to biased viscosity profiles (see Mitrovica, 1996, for a more complete discussion of this issue).

In the inversions described below, we incorporate an additional model parameter, the thickness of the elastic lithosphere, L. The associated 29th element of the Fréchet kernel vector for each datum is defined by

$$\delta \log y_i = F_i^L(\log \nu)\, \delta L, \tag{5.8}$$

where δL is a perturbation in the thickness of the elastic lithosphere. The 29th parameter thus determines the LAB and the thickness of the 28th model layer.

The iteration scheme given by eq. (5.5) will be deemed to have converged once the misfit statistic $Q(\hat{\mathbf{X}}_k)$ given by:

$$Q(\hat{\mathbf{X}}_k) = \left[\mathbf{y} - f(\hat{\mathbf{X}}_k)\right]^T \mathbf{V}_{\xi}^{-1} \left[\mathbf{y} - f(\hat{\mathbf{X}}_k)\right], \tag{5.9}$$

falls within the 99% confidence interval of the χ^2_N distribution, where N is the number of degrees of freedom. The converged solution will be defined by an *a posteriori* model, which we denote by $\hat{\mathbf{X}}_{\mathrm{PO}}$ and the associated covariance $\mathbf{V}_{\mathrm{PO}}$. Due to the weakly nonlinear character of this inversion, the solutions generally converge after one iteration.

5.3 DATA

5.3.1 FENNOSCANDIAN RELAXATION SPECTRUM

The FRS is derived from ancient strandlines that can be traced more or less continuously for ~1000 km from the center of uplift out to the periphery, and that permit an estimate of the uplift rate in the region versus spatial scale. The data set, and its analysis, were pioneered by McConnell (1968), who used strandline data compiled by Sauramo (1958) to infer the radial profile of viscosity to a depth of 1200 km. This depth is consistent with the resolving power of the data set (Parsons, 1972; Mitrovica & Peltier, 1993b). A revised FRS spanning the degree ranges $15 \leq \ell \leq 49$ and $61 \leq \ell \leq 73$ was derived by Wieczerkowski et al. (1999), who used a set of strandline records published by Donner (e.g., Donner, 1980) that extend from near Ångerman River to southern Finland and (in a subset of the records) terminate in Estonia (see Fig. 5.1a). Wieczerkowski et al. (1999) used a damped least squares approach that allowed for a rigorous assessment of uncertainty in the FRS and the reader is referred to this publication for a comprehensive discussion of both their methodology and a suite of sensitivity tests related to the sampling of the strandline data and common assumptions made in forward calculations of the FRS. We adopt the FRS derived by Wieczerkowski et al. (1999), although we truncate our analysis at degree 64 (Fig. 5.2a). This truncation has no impact on our results given the large uncertainty in the relaxation times for degrees above 60 (Wieczerkowski et al., 1999). It does, however, decrease the shallow mantle sensitivity of the FRS data relative to the sensitivity associated with original values of McConnell (1968).

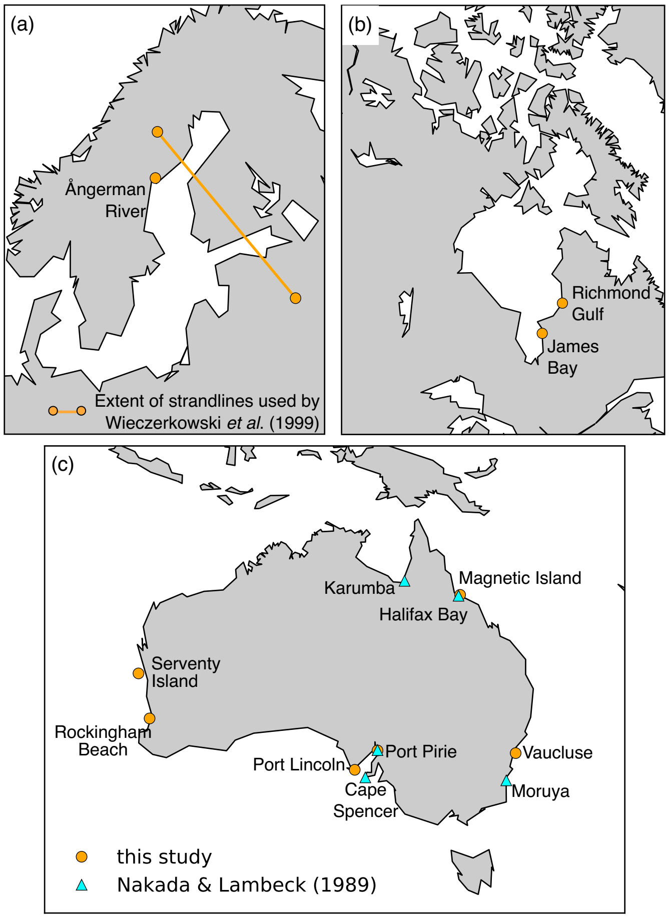
(a)
Ångerman
River
Extent of strandlines used by
Wieczerkowski *et al.* (1999)
(b)
Richmond
Gulf
James
Bay
(c)
Karumba
Magnetic Island
Halifax Bay
Serventy
Island
Rockingham
Beach
Port Lincoln
Port Pirie
Cape
Spencer
Vaucluse
Moruya
this study
Nakada & Lambeck (1989)

FIGURE 5.1: (a) Map of Scandinavia including the extent of strandlines used to determine the FRS (Wieczerkowski et al., 1999) and the location of Ångerman River. (b) Map of Hudson Bay showing the locations of Richmond Gulf and James Bay. (c) Location of Australian Late Holocene sea level highstand records studied by Nakada & Lambeck (1989), and the more recent compilation adopted in the present study as labeled.

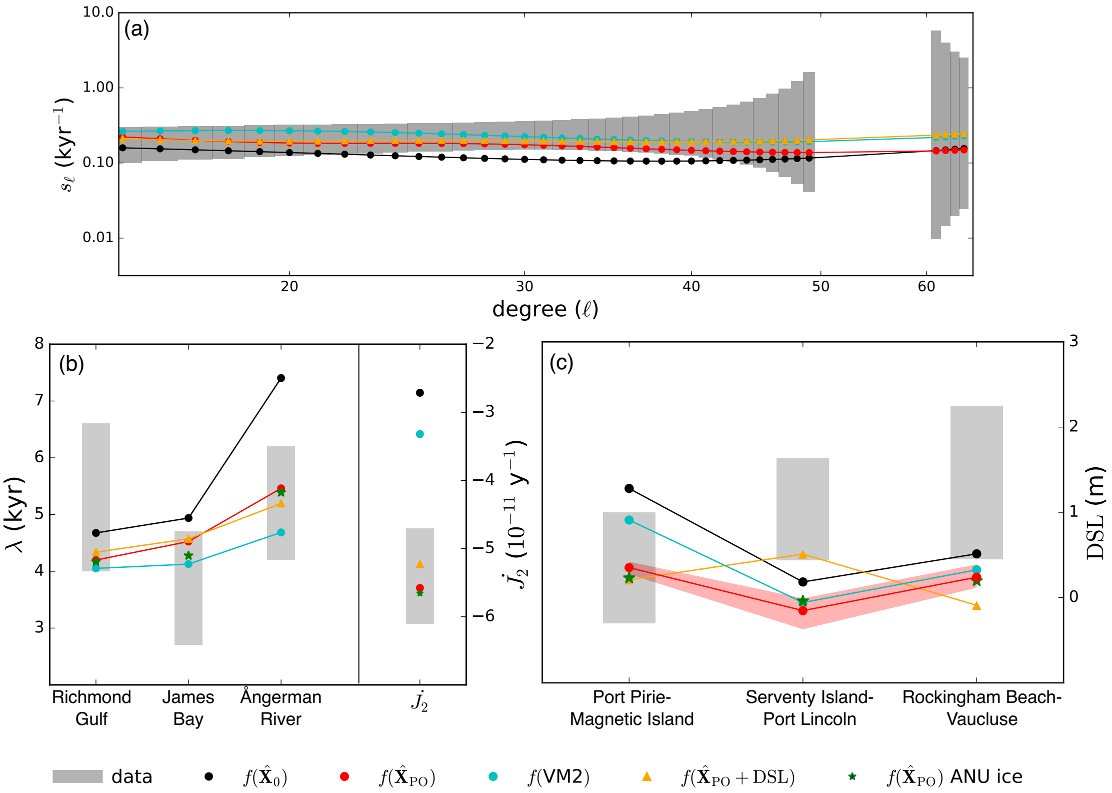

FIGURE 5.2: Observational constraints (gray bars) associated with: (a) the Fennoscandian relaxation spectrum, (b) post-glacial decay times in Richmond Gulf, James Bay and Ångerman River, and $\dot{J}_2$; and (c) Differential sea level highstands. Predictions based on both the starting model, $\hat{\mathbf{X}}_0$, and the *a posteriori* model in Fig. 5.4, $\hat{\mathbf{X}}_{\mathrm{PO}}$, are superimposed on each frame. The red shading in (c) encompasses a set of predictions of the DSL highstands based upon the *a posteriori* viscosity model in Fig. 5.4 and lithospheric thicknesses ranging from (87–107) km. Also included in each frame are predictions based on the viscosity model VM2 (Peltier, 2004) and an additional *a posteriori* model, $\hat{\mathbf{X}}_{\mathrm{PO}}$ + DSL, discussed in Section 5.4.2 in which DSL highstand data were incorporated into the inversion.

5.3.2 Post-Glacial Decay Times

As we noted above, and following the original analysis of records from Hudson Bay (Walcott, 1972), post-glacial decay times have been determined by fitting an exponential form (eq. 5.3) through local RSL histories (sometimes termed uplift or emergence curves) at sites near the centre of the now-vanished Late Pleistocene ice sheets. Given their relative insensitivity to ice history, the decay times

(λ) represent an important constraint on mantle viscosity, and there have been many efforts to estimate them at sites in Hudson Bay and James Bay, Canada (e.g., Mitrovica & Peltier, 1995; Mitrovica & Forte, 1997; Peltier, 1998a; Mitrovica et al., 2000; Fang & Hager, 2002) and Ångerman River, Sweden (Mitrovica, 1996; Mitrovica & Forte, 2004; Nordman et al., 2015). For Richmond Gulf in Hudson Bay we adopt a one-sigma constraint on the decay time of 4.0–6.6 kyr (Mitrovica et al., 2000). For James Bay, we have computed a post-glacial decay time of 2.7–4.7 kyr based on a new RSL curve for the region (Pendea et al., 2010). An earlier estimate of the James Bay decay time (2.0–2.8 kyr), based on records collected in the mid 1970s (Hardy, 1976; Mitrovica et al., 2000), was inconsistent with the Richmond Gulf value, and this posed significant difficulties for viscosity inversions based upon both of them. The revised decay time is more consistent with the Richmond Gulf datum and avoids this complication. For the decay time at Ångerman River, we adopt the recent estimate of Nordman et al. (2015), 4.2–6.2 kyr, which is a minor revision to the estimate in Mitrovica & Forte (2004) (4.0–5.7 kyr). The decay times adopted in our inversions are shown in Fig. 5.2(b) and their geographical locations are shown in Fig. 5.1(a,b). The Mitrovica et al. (2000) analysis ensured free-decay of the Hudson Bay and James Bay sites by choosing a time window for their decay time analysis of 8.5 kyr. Nordman et al. (2015) adopted a time window of 7 kyr for their analysis of the Ångerman River decay time. Our numerical calculations of decay times adopt the same windows.

5.3.3 $\dot{J}_2$

As noted in the Introduction, recent analyses of the J_2 time series estimated from satellite altimetry measurements since the mid-1970s indicated a significant change in trend circa 1990 (Nerem & Wahr, 2011; Roy & Peltier, 2011; Cheng et al., 2013), and the time series has been fit with, for example, a quadratic trend (Cheng et al., 2013) or with a slope break in the early 1990s (Roy & Peltier, 2011). The change in trend that occurred $\sim$1990 has been associated with the onset of significant melting from polar ice sheets, and so we focus here on the altimetry record from 1976–1990. Using the results of Cheng et al. (2013), we estimate a linear trend across the time window of $(-3.4 \pm 0.3) \times 10^{-11}$ yr^{-11}, where the uncertainty accounts for nonlinearity in the time series (Mitrovica et al., 2015). Cheng et al. (2013) estimated the size of signals in the observed time series associated with atmospheric and ocean variability, and the 18.6 year tide, and using their calculations suggests that these signals may combine to produce a trend of order 0.3×10^{-11} yr^{-1}. Accordingly, we augment the above uncertainty in the observed trend to a value of 0.5×10^{-11} yr^{-11}.

In order to isolate the signal from GIA (which would have remained constant over the 20th century) in the harmonic $\dot{J}_2$, one must correct the observed trend for contamination associated with ice melting (Ivins et al., 1993; Mitrovica & Peltier, 1993a; Nakada et al., 2015a; Mitrovica et al., 2015). Marzeion et al. (2015) recently updated glacier tabulations by Marzeion et al. (2012) and Leclercq et al. (2011) and compared these, together with release 1301 of the Cogley (2009) database. The latter two tabulations are based on direct and geodetic measurements, with suitable extrapolation to unsampled areas, while the first is based on modeled responses to local climate observations. Over the period 1976–1990, the Cogley (2009) database has a mass flux rate from all glaciers of 0.66 ± 0.03 mm y^{-1} in units of equivalent global mean sea-level (GMSL) rise. The analogous values for the updated Leclercq et al. (2011) database are 0.35 ± 0.05 mm y^{-1}, and for the updated Marzeion et al. (2012) database, 0.42 ± 0.12 mm y^{-1}. Over the period 1971–2009, AR5 of the IPCC based its estimates of glacier mass flux on Marzeion et al. (2012) and Cogley (2009). Following the IPCC, we focus on the Cogley (2009) and Marzeion et al. (2012) results to compute the $\dot{J}_2$ signal for the period 1976–1990. We have calculated the total $\dot{J}_2$ signal associated with these tabulations and they are: $(-1.94 \pm 0.10) \times 10^{-11}$ y^{-1} and $(-1.07 \pm 0.05) \times 10^{-11}$ y^{-1}, respectively. Combining these two estimates yields a J_2 rate of $(-1.5 \pm 0.4) \times 10^{-11}$ y^{-1}, where the uncertainty is computed from the spread of the two estimates rather than the formal uncertainties in each. (Including the Leclercq et al. (2011) time series yields a marginally different estimate of the rate,

$(-1.4 \pm 0.4) \times 10^{-11}$ y^{-1}.)

In addition to the above source of melt, Kjeldsen et al. (2015) analyzed photographic evidence to estimate mass loss from the Greenland Ice Sheet from 1900–2010. Their so-called geodetic method yields an estimate of mass loss from 1976–1990 of 0.12 ± 0.5 mm y^{-1} in units of GMSL. Using this inference, we have calculated a $\dot{J}_2$ signal of $(0.5 \pm 0.2) \times 10^{-11}$ y^{-1} over the same period. Combining this with the glacier signal gives a total $\dot{J}_2$ signal due to modern melt sources of $(2.0 \pm 0.5) \times 10^{-11}$ y^{-1}. Our standard inversion described below will adopt this melt signal. Correcting the observed trend $(-3.4 \pm 0.5) \times 10^{-11}$ y^{-1} for this signal, yields a residual signal of $(-5.4 \pm 0.7) \times 10^{-11}$ y^{-1}, which represents our estimate of the ongoing GIA contribution to $\dot{J}_2$. (This value is consistent with the GIA rate inferred by Nakada et al. (2015a) and Mitrovica et al. (2015).) We will, however, consider the sensitivity of our results to the adopted melt signal by varying it over a range consistent with the above uncertainty; i.e., $(1.5–2.5) \times 10^{-11}$ y^{-1}.

5.3.4 DIFFERENTIAL SEA-LEVEL HIGHSTANDS

We will explore the consistency of predictions based on our inverted viscosity profiles with differential sea-level (DSL) highstands between various pairs of far-field sites. In the classic study of Nakada & Lambeck (1989), four DSL highstand pairs were used to infer a large increase (∼two orders of magnitude) in mantle viscosity with depth. All sites were located in the Australasia region (see Fig. 5.1): Karumba (Queensland), Halifax Bay (Queensland), Moruya (New South Wales), Port Pirie (South Australia), Cape Spencer (South Australia) and Christchurch (New Zealand). The late Holocene sea-level record across Australia has recently been updated (e.g., Sloss et al., 2007; Lewis et al., 2013), and our analysis is based on this new set of records. We performed synthetic tests to explore the sensitivity of the predicted DSL highstands to variations in the ice model by considering forward predictions based on two ice models: ICE-6G (Peltier et al., 2015) and a global ice model developed at the ANU (Fleming & Lambeck, 2004). On this basis, we culled the DSL highstand data set to include only site pairs for which the two predictions agreed to within half of one-sigma observational uncertainty. This yielded site pairs: Port Pirie-Magnetic Island (Belperio et al., 2002; Collins et al., 2006, respectively), Serventy Island-Port Lincoln (Collins et al., 2006; Belperio et al., 2002, respectively), and Rockingham Beach-Vaucluse (Lewis et al., 2013; Sloss et al., 2007, respectively). (See Fig. 5.1 for site locations.) Their associated DSL highstand values are 0.35 ± 0.65 m, 1.04 ± 0.45 m, and 1.35 ± 0.90 m, respectively.

5.4 Results and Discussion

5.4.1 Fréchet Kernels

Fréchet kernels provide a measure of the sensitivity of a datum to depth-dependent perturbations in mantle viscosity. We explore this sensitivity in Fig. 5.3, which shows kernels for the data sets listed in Section 5.3, for two different viscoelastic models (see Table 5.1). Model A has a moderate, factor of two increase in viscosity from the upper mantle (10^{21} Pa s) to the lower mantle; this jump is increased to a factor of ten in Model B by reducing the upper mantle viscosity to 5×10^{20} Pa s and increasing the lower mantle viscosity to 5×10^{21} Pa s.

Figs 5.3(a,b) show values of the kernel for each datum associated with a perturbation in lithospheric thickness, L (i.e., F^L in eq. 5.8, plotted as a percent perturbation in the datum per kilometer perturbation in L). The DSL highstand data—and in particular the Serventy Island-Port Lincoln pair—exhibit the greatest sensitivity to lithospheric thickness variations, which reflects the underlying physical process that gives rise to spatial variations in the Australian RSL highstands; namely, the levering (or tilting) of the lithosphere and crust in response to ocean loading. The sensitivity is, however, a strong function of the specific pair of sites being considered. The sensitivity of the FRS data to changes in L increases monotonically with increasing spherical harmonic degree, with the greatest sensitivity being a $\sim$1% reduction in the predicted inverse decay time per kilometer increase

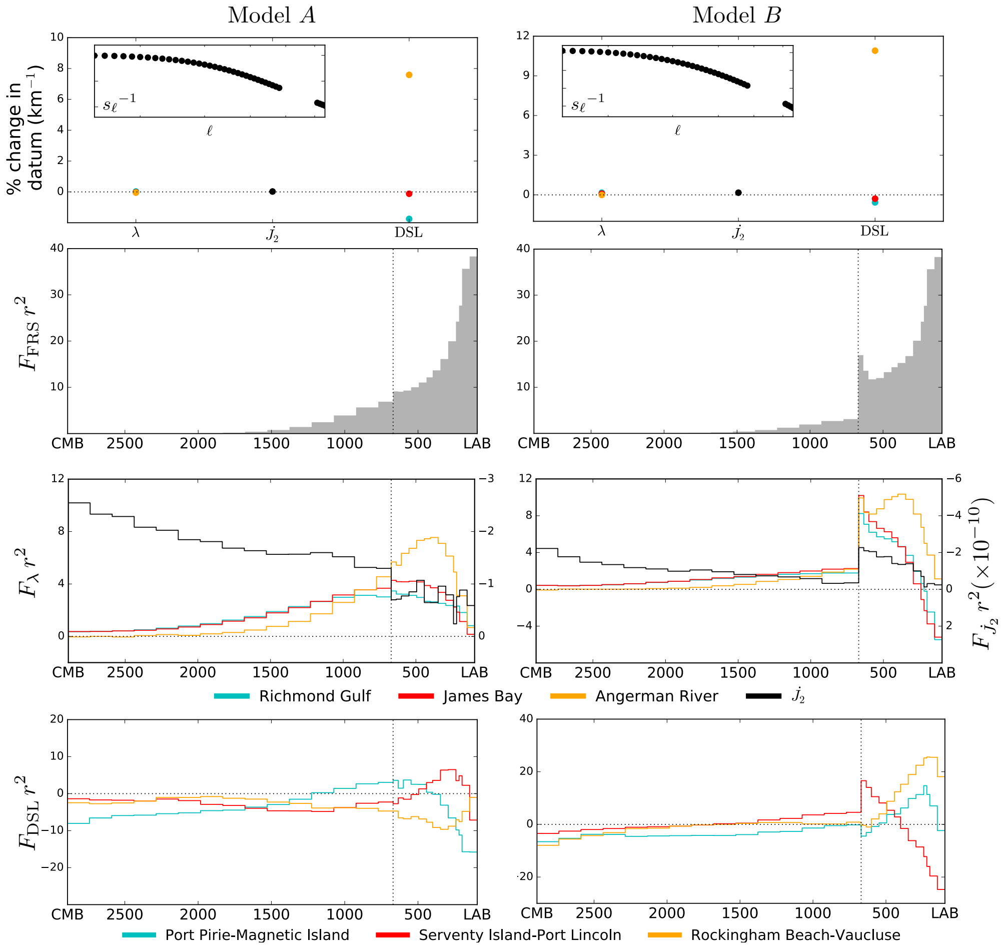

FIGURE 5.3: Dimensionless Fréchet kernels computed using Model A (left panels) and Model B (right panels). See Table 5.1 for all model parameters. Frames (a–b) show the 29th value of the Fréchet kernel for each datum associated with the lithospheric thickness parameter, in units of percent change per km (eq. 5.8). The insets show kernel values associated with the FRS. The color circles correspond to the specific sites shown in the keys below (e,f) and (g,h). Frames (c–h) show Fréchet kernels computed for the 28 radial viscosity parameters. (c,d) Kernels for the FRS, where the shaded band spans the full region sampled by all kernels in the degree range $15 \leq \ell \leq 49$ and $61 \leq \ell \leq 64$. The blue line in frame (c) is discussed in Section 5.4.2. (e,f) Kernels for the logarithm of the post-glacial decay times, log λ, at Richmond Gulf (Canada), James Bay (Canada) and Ångerman River (Sweden), as well as the $\dot{J}_2$ datum. Note that the left vertical axes in (e,f) are values associated with the decay times and the right vertical axes are associated with $\dot{J}_2$. (g,h) Kernels for the DSL highstands between the following pairs of Australian sites: Port Pirie-Magnetic Island, Serventy Island-Port Lincoln, and Rockingham Beach-Vaucluse. All kernels in (c–h) are scaled by r^2. In frames (c–h) the horizontal axes mark depth (km) and the black dotted vertical line marks the boundary between the upper and lower mantle.

in the lithospheric thickness. Finally, the Hudson Bay and Fennoscandian decay times, as well as the $\dot{J}_2$ datum, are insensitive to lithospheric thickness changes.

In considering the remaining Fréchet kernels, we first focus on results for Model A. The sensitivity of the FRS to variations in mantle viscosity is strongest in the upper mantle with peak sensitivities at the base of the lithosphere (the latter reflects the sensitivity associated with highest degree components of the FRS). There is a monotonic decrease in the lumped sensitivity with depth and the relaxation spectrum is relatively insensitive to viscosity perturbations below $\sim$1000 km. The kernel for the post-glacial decay time at Ångerman River has a sensitivity that peaks in the upper mantle and extends $\sim$500 km into the lower mantle. In comparison, the kernels for the decay times at sites in Hudson Bay have a diminished sensitivity to the upper mantle and a sensitivity that extends further into the lower mantle. This difference in the radial range of the kernels reflects the distinct spatial scales of the ice sheets that covered the two regions (Mitrovica, 1996). In contrast to the FRS and decay times, the sensitivity of the $\dot{J}_2$ datum to perturbations in mantle viscosity increases towards the CMB. The amplitude of the kernel decreases by $\sim$50% across the lower mantle from the CMB to 670 km depth, and drops abruptly at the boundary with the upper mantle. Finally, DSL highstand data each have distinct sensitivities to mantle viscosity, though all the kernels tend to show a broad sensitivity to viscosity across both the lower and upper mantle. The former results from the large spatial scale of the ocean load, while the latter reflects the sensitivity of the levering process to shallow mantle structure.

Model	lithospheric thickness (km)	upper mantle ν (Pa s)	lower mantle ν (Pa s)
A	96	1.0×10^{21}	2.0×10^{21}
B	96	0.5×10^{21}	5.0×10^{21}

Table 5.1: Viscosity models discussed in the text. The boundary between the upper and lower mantle is at 670 km depth. Elastic and density structure is given by the seismic model PREM (Dziewonski & Anderson, 1981)

	Model A		Model B	
	lower	upper	lower	upper
FRS	5	95	2	98
Richmond Gulf	25	75	16	84
James Bay	23	77	18	92
Ångerman	12	88	5	95
$\dot{J}_2$	56	44	30	70
Port Pirie-Magnetic Island	32	68	31	69
Serventy Island-Port Lincoln	38	62	9	91
Rockingham Beach-Vaucluse	18	82	9	91

TABLE 5.2: Integrated area under the Fréchet kernels in Fig. 5.3 within the lower and upper mantle, expressed as a percentage of the total area.

The Frećhet kernels computed using Model B, characterized by an order of magnitude viscosity jump at 670 km depth, show sensitivities that are shifted toward shallower depths, relative to predictions based on Model A. By introducing a higher viscosity lower mantle, flow is more confined to the upper mantle, thus increasing the upper mantle sensitivity of each datum. As a measure of this trend, Table 5.2 lists the integrated area under the Fréchet kernels in the upper and lower mantle for each datum (or in the case of the FRS, the lumped kernel) and the two Earth models. The significant change in the depth range of the kernels evident in Fig. 5.3 and Table 5.2 underscores the nonlinearity of the mapping between viscosity and GIA data sets.

5.4.2 BAYESIAN INVERSION FOR MANTLE VISCOSITY

We begin by presenting the results of nonlinear, Bayesian inversions (eq. 5.5) that adopt Model A as both the starting model, $\hat{\mathbf{X}}_0$, and the *a priori* model, ($\mathbf{X}_{\mathrm{PR}}$). We assume no prior covariance between the model parameters, and adopt a prior variance, ${\sigma_{\mathrm{PR}}}^2$, of 20 for all log-viscosity model parameters and 100 km^2 for the lithospheric thickness. The large prior variances allow the *a posteriori* solution to move significantly from the *a priori* model should the data require this. Predictions

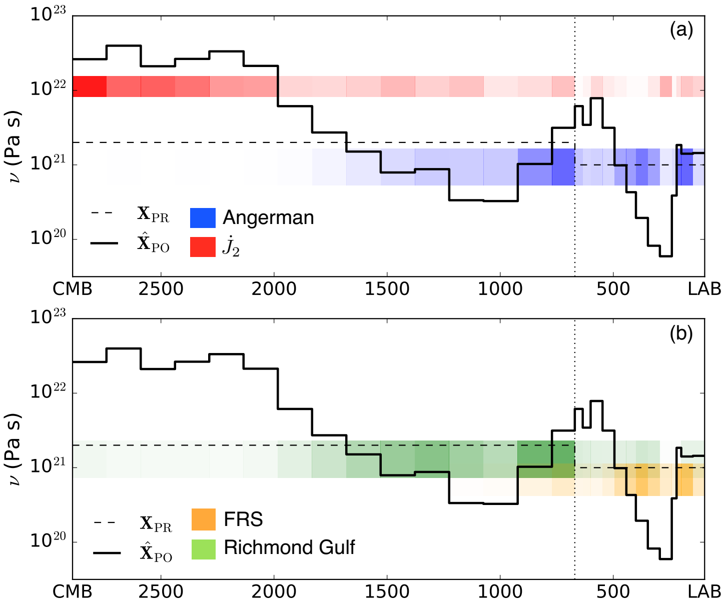

FIGURE 5.4: Nonlinear, Bayesian inversion of the FRS, post-glacial decay times from Richmond Gulf, James Bay and Ångerman River, and $\dot{J}_2$ observations. The dashed black line is the starting and *a priori* model adopted in the inversion. The solid black line is the *a posteriori* solution. These are repeated in both panels (a) and (b). The height of the center of each color band denotes the weighted average ($\bar{\mathbf{F}}_i^T \mathbf{X}_{\mathrm{PO}}$) of the inverted model, where the weightings are normalized and volumetrically scaled Fréchet kernels for the posterior model shown in Fig. 5.5 (eq. 5.10). The vertical thickness of each color band represents the one standard deviation bound on the weighted average, while the color intensity indicates the normalized amplitude of the averaging kernel, $\bar{\mathbf{F}}_i$ (see Fig. 5.5). In each frame the horizontal axis marks depth (km) and the black dotted vertical line marks the boundary between the upper and lower mantle.

based on the *a priori* (and starting) model are shown in Fig. 5.2.

Fig. 5.4 shows the results of a joint inversion of the FRS, post-glacial decay times, and $\dot{J}_2$ data sets. The *a posteriori* estimate of the lithospheric thickness is 96.87 ± 9.97 km. The minor reduction in the uncertainty of the estimate of L from its *a priori* value reflects the relative lack of sensitivity of these data to variations in this parameter. The inverted model is characterized by: a weak asthenosphere, with a viscosity as low as $\sim 10^{20}$ Pa s, an average viscosity of $\sim 10^{21}$ Pa s in the top ~ 1000 km of the lower mantle, and a relatively uniform increase in viscosity to $\sim 5 \times 10^{22}$ Pa s at 2400 km depth. The latter is maintained to the base of the mantle. Predictions based on the inverted model are shown on Fig. 5.2, labeled $f(\hat{\mathbf{X}}_{\mathrm{PO}})$.

The *a priori* (and starting) model misfits all data used in the inversion except the post-glacial decay time at Richmond Gulf and decay times in the FRS outside the degree range 21–42. The lower viscosity of the inverted model relative to the starting model across nearly all depths from the LAB to the mid-lower mantle reduces the relaxation times at all degrees and brings the predicted FRS into accord with the observations. This reduction in viscosity also decreases the predicted post-glacial decay times. In particular, the *a posteriori* model yields decay times that match the observed values at all three sites: Ångerman River, James Bay and Richmond Gulf. Finally, the inverted model is characterized by a significantly higher viscosity in the deep mantle (below $\sim$1700 km depth) relative to the starting model, and this increases the amplitude of the predicted $\dot{J}_2$ anomaly by $\sim$80 %, sufficient to match the observation. Predictions based on the viscosity model VM2 (Peltier, 2004) are also shown in Fig. 5.2. We note that this model yields a reasonable fit to all the data in Figs 5.2(a,b) with the exception of a major misfit with the $\dot{J}_2$ datum.

The significance of the variability and trends in the inverted viscosity profile in Fig. 5.4 is dependent on the radial resolving power of the data set. We explore this issue in two ways. First, we compute weighted averages of the inverted model parameters, where the weightings are given by Fréchet kernels computed using the *a posteriori* model (Fig. 5.5). (In this exercise we do not include the final lithospheric thickness component of the Fréchet kernel; see eq. 5.8). Following eq. (5.7), we denote the ith such Fréchet kernel as $F_i(\mathbf{X}_{\mathrm{PO}}, r)$, and define normalized versions of these kernels that satisfy:

$$\int_{\mathrm{CMB}}^{\mathrm{LAB}} \bar{F}_i(\mathbf{X}_{\mathrm{PO}}, r) r^2 \mathrm{d}r = 1, \tag{5.10}$$

where $\bar{F}_i(\mathbf{X}_{\mathrm{PO}}, r) = c_i F_i(\mathbf{X}_{\mathrm{PO}}, r)$, and the constant c_i is chosen to satisfy the normalization constraint. If we express the normalized kernel in vector form as $\bar{\mathbf{F}}_i$, then the ith weighted average is given by:

$$\hat{X}_i = \bar{\mathbf{F}}_i^T \mathbf{X}_{\mathrm{PO}}, \tag{5.11}$$

which has variance

$$\mathbf{V}_i = \bar{\mathbf{F}}_i^T \mathbf{V}_{\mathrm{PO}} \bar{\mathbf{F}}_i. \tag{5.12}$$

The colored horizontal bars superimposed on Figs 5.4(a,b) are designed to provide three pieces of information. The intensity of the shading across the bar reflects the amplitude of the normalized kernel $\bar{F}_i(\mathbf{X}_{\mathrm{PO}}, r)$ across the 28 layers spanning the CMB to LAB. The height at the center of the bar represents the weighted average $\bar{\mathbf{F}}_i^T \mathbf{X}_{\mathrm{PO}}$, and the vertical thickness of the bar represents one standard deviation uncertainty of the estimate. The four bars refer, as labeled, to weighted averages of the posterior model based on kernels for the post-glacial decay times at Richmond Gulf (green) and Ångerman River (blue), the $\dot{J}_2$ constraint (red), and the FRS (orange; in this case, the averaging kerning kernel is denoted by the black line in Fig. 5.5(a), which provides a representative sensitivity of the FRS to variations in mantle viscosity).

As an example, the weighted average associated with the Ångerman River decay time is $\sim 10^{21}$ Pa s. The averaging reflects a dominant sensitivity that extends to a depth of ~ 1000 km (see the blue bar in Fig. 5.4a or the posterior Fréchet kernel for this decay time in Fig. 5.5b). This average represents the classic constraint on mantle viscosity known as the "Haskell value" (Haskell, 1935; Mitrovica, 1996). The weighted average resolved by the Hudson Bay decay time data is also $\sim 10^{21}$ Pa s; however, the averaging kernel in this case shows significantly greater sensitivity to viscosity in the top half of the lower mantle than the Ångerman River kernel (Fig. 5.5b). The yellow bar in Fig. 5.4 indicates that the FRS data are highly sensitivity to the viscosity structure just beneath the LAB. Whereas the higher degree components of the FRS constrain this shallow upper mantle structure, the lower degree components extend the sensitivity throughout the upper mantle and into the top 200 km of the lower mantle (Fig. 5.5a).

The weighted averages in Fig. 5.4 provide insight into the high deep mantle viscosity of the inverted model. The Hudson Bay and Ångerman River data have combined sensitivities that extend from the middle of the upper mantle to the middle of the lower mantle and these constraints drive the mean viscosity in this region to $\sim 10^{21}$ Pa s (within the upper mantle, the inverted profile is also

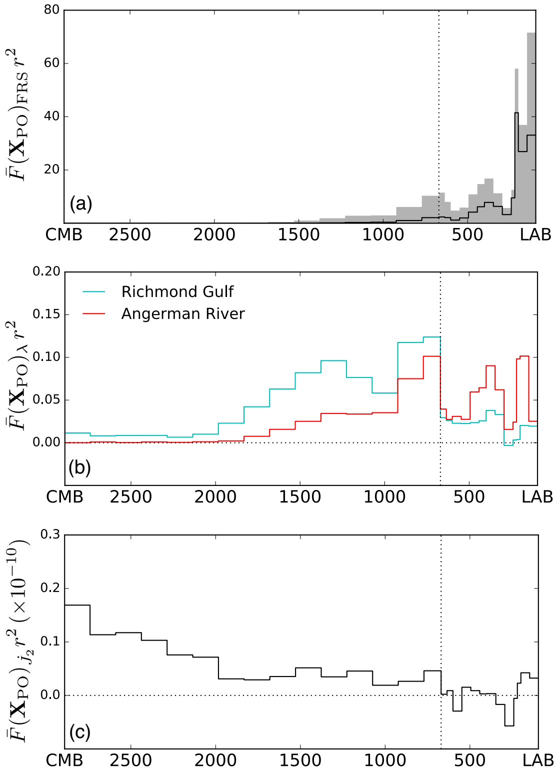

FIGURE 5.5: Fréchet kernels as defined in eq. (5.7) for (a) the FRS, (b) post-glacial decay times at Ångerman River, Sweden and Richmond Gulf, Canada, and (c) the $\dot{J}_2$ datum, all computed using the *a posteriori* model in Fig. 5.4 (the lithospheric thickness of this model is 96.87 km). The kernel for the James Bay decay time (not shown) differs negligibly from the kernel associated with the Richmond Gulf decay time. All kernels are scaled by r^2. In each frame the horizontal axis marks depth (km) and the black dotted vertical line marks the boundary between the upper and lower mantle.

strongly controlled by the FRS). The $\dot{J}_2$ datum has a sensitivity to viscosity that is non-negligible throughout the lower mantle and fitting it requires a weighted mean viscosity of $\sim 10^{22}$ Pa s across this region, where the weighting is dominated by values in the bottom half of the lower mantle (red bar in Fig. 5.4a, kernel in Fig. 5.5c). Thus, in order to fit both the decay time data and the $\dot{J}_2$ observation, the viscosity of the bottom half of the lower mantle in the inverted model must increase to values above 10^{22} Pa s. Indeed, $\mathbf{X}_{\mathrm{PO}}$ peaks at $\sim 4 \times 10^{22}$ Pa s in this region, and the volumetric average of the model in the bottom 1000 km of the mantle is $\sim 2.5 \times 10^{22}$ Pa s.

The resolving power of the inversion as a function of depth can be also explored by examining the *a posteriori* covariance matrix, $\mathbf{V}_{\mathrm{PO}}$, as defined in eq. (5.6); (Fig. 5.6). With the exception of the shallowest layers of the inverted model, the variance of the model parameters, i.e., the diagonal elements of $\mathbf{V}_{\mathrm{PO}}$ (Fig. 5.6a), show little reduction from their *a priori* values, and this indicates that the observations do not resolve viscosity structure on the radial length-scale of the individual model layers. As discussed in Section 5.2.2, although ice age data are not able to resolve the viscosity across a length-scale comparable to any single model layer thickness, we adopt this fine discretization to avoid biasing any viscosity inversion by introducing, for example, artificial viscosity jumps. The resolving power is, in this regard, more directly reflected by the rows of the covariance matrix. Figs 5.6(b–e) show a representative set of rows of $\mathbf{V}_{\mathrm{PO}}$ that span target depths in the top 1800 km of the mantle. The covariances in each frame are normalized such that the peak off-diagonal value is unity (the normalized posterior covariance matrix is denoted $\bar{\mathbf{V}}_{\mathrm{PO}}$).

For rows corresponding to model layers within the top half of the mantle (Figs 5.6b–d), the covariances are roughly centered on the target depth and the resolving power (as reflected by the spread of the covariances) decreases with depth. As an example, the estimate of viscosity at 373 km depth (Fig. 5.6b) will represent an average that extends across the most of the upper mantle. This resolution decreases to $\sim$1000 km (420–1450 km depth) and $\sim$1400 km (700–2100 km depth) for targets at 846 km (Fig. 5.6c) and 1452 km (Fig. 5.6d) depth. Finally, covariances associated with

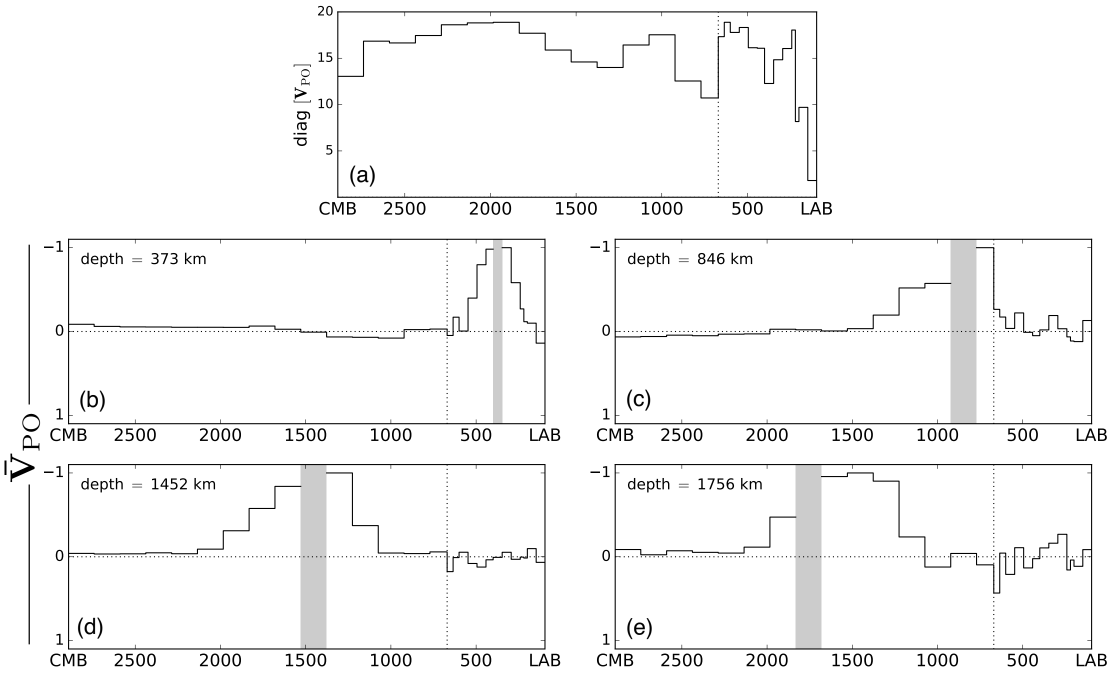

Figure 5.6: The posterior covariance matrix, $\mathbf{V}_{\rm PO}$ (eq. 5.6), for the inversion shown in Fig. 5.4. (a) The diagonal values of $\mathbf{V}_{\rm PO}$. (b–e) Select rows of $\bar{\mathbf{V}}_{\rm PO}$ for target radii (as labeled) ranging from (b) just below the LAB to (e) the middle of the lower mantle. The target layer in each case is shown by gray shading that identifies its location. In all frames, the $\mathbf{V}_{\rm PO}$ values associated with the lithospheric thickness parameter are not included. The horizontal axis marks depth (km) and the black dotted vertical line marks the boundary between the upper and lower mantle.

estimates of viscosity at depths greater than the middle of the lower mantle (e.g., Fig. 5.6e) peak in layers at shallower depths (i.e., the covariances are no longer centered on the target depth) and this reflects the limited ability of the data set to resolve structure at these depths.

Sensitivity Analyses

In a first series of sensitivity tests, we adopted the same prior and starting model discussed above but included only one data type (FRS, $\dot{J}_2$, or decay times) in each inversion (Fig. 5.7). The goal in these tests is to further refine our understanding of the constraints that each data subset contributes to the joint inversion in Fig. 5.4.

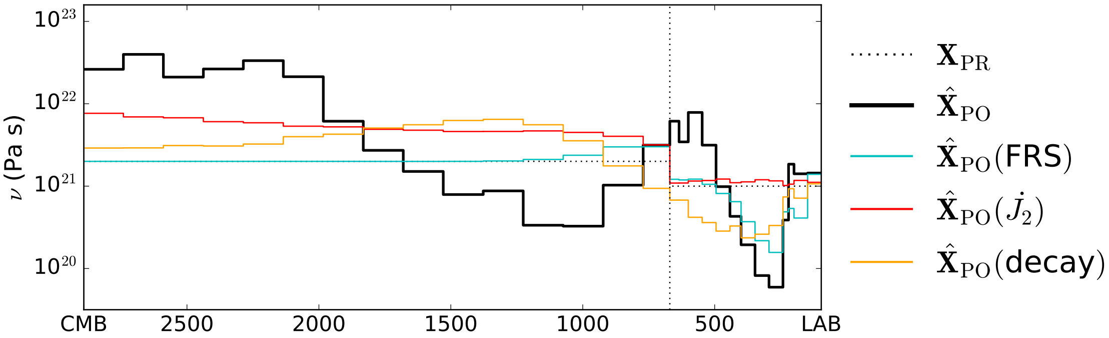

FIGURE 5.7: Results from sensitivity testing of the nonlinear, Bayesian inversion: $\hat{\mathbf{X}}_{\mathrm{PO}}$ and $\mathbf{X}_{\mathrm{PR}}$ are reproduced from Fig. 5.4. $\hat{\mathbf{X}}_{\mathrm{PO}}$(FRS) is the posterior model for an inversion that included only the Fennoscandian relaxation spectrum, $\hat{\mathbf{X}}_{\mathrm{PO}}(\dot{J}_2)$ included only the $\dot{J}_2$ datum and $\hat{\mathbf{X}}_{\mathrm{PO}}$(decay) included only the three post-glacial decay times. The horizontal axis marks depth (km) and the black dotted vertical line marks the boundary between the upper and lower mantle.

An inversion of the FRS data alone departs from the *a priori* model in the top 800 km of the mantle and it closely tracks the *a posteriori* model generated from the inversion of the full data set in the upper mantle above the transition zone. The latter indicates that much of the finer scale upper mantle structure of the inverted model in Fig. 5.4 is controlled by the constraints imposed by the FRS. The decay time inversion yields a model characterized by a mean viscosity of $\sim 5 \times 10^{20}$ Pa s in the upper mantle below the LAB and an increase to $\sim 3 \times 10^{21}$ Pa s across the top 600 km of the lower mantle. This trend satisfies the Haskell constraint on mantle viscosity discussed above (Haskell, 1935; Mitrovica, 1996). Below this depth and toward the CMB, the viscosity values tend toward the *a priori* model, reflecting the progressively decreasing depth sensitivity of these data. Finally, an inversion of the $\dot{J}_2$ constraint alone yields an *a posteriori* model that tracks the *a priori* model in the upper mantle and increases to values of $\sim 10^{22}$ Pa s near the base of the lower mantle. This is consistent with our earlier observation that the datum has relatively little sensitivity to upper mantle viscosity, and a broad sensitivity to lower mantle viscosity that constrains the mean viscosity in this region to be $\sim 10^{22}$ Pa s in the bottom half of this region. This result emphasizes once again that the $\dot{J}_2$ datum provides the dominant constraint on deep mantle viscosity in our inversions;

Test	tr$[\mathbf{R}]$
$\hat{\mathbf{X}}_{\mathrm{PO}}$	6.75
$\hat{\mathbf{X}}_{\mathrm{PO}}$(FRS)	4.03
$\hat{\mathbf{X}}_{\mathrm{PO}}(\dot{J}_2)$	0.99
$\hat{\mathbf{X}}_{\mathrm{PO}}$(decay)	2.36

Table 5.3: Trace of resolution matrix for inversions based on various data subsets

without this constraint the information content of the GIA data would largely end at mid-lower mantle depths.

The information content of each data subset can be quantified by considering the trace of the so-called resolution matrix (Backus, 1988):

$$\mathbf{R} = \mathbf{I} - \mathbf{V}_{\mathrm{PO}}\mathbf{V}_{\mathrm{PR}}^{-1} \tag{5.13}$$

where $\mathbf{I}$ is the identity matrix. The trace of $\mathbf{R}$, tr$[\mathbf{R}]$, is a measure of the number of independent parameters resolvable in a given inversion, and it is listed in Table 5.3 for the four *a posteriori* models shown in Fig. 5.7. If the data provided perfect resolution in any inversion, then tr$[\mathbf{R}]$ would be equal to the number of parameters (in our case 29). The fact that the sum of the tr$[\mathbf{R}]$ computed for inversions with single data types is approximately equal to the trace when all data types are included indicates that the data subsets do not have significant overlap in information content.

Next, we explore the impact on the inversions when applying smoothing to the model parameters. To include smoothing in the inversion we introduce covariances in the matrix $\mathbf{V}_{\mathrm{PR}}$. Specifically, the element on the mth row and n^{th} column of the matrix can be expressed as

$$[V_{\mathrm{PR}}]_{mn} = \sigma(m)\sigma(n)e^{-\|r_m - r_n\|\gamma^{-1}}. \tag{5.14}$$

Here, $\sigma(m)$ is the prior standard deviation of the mth model parameter, r_m is the center radius of

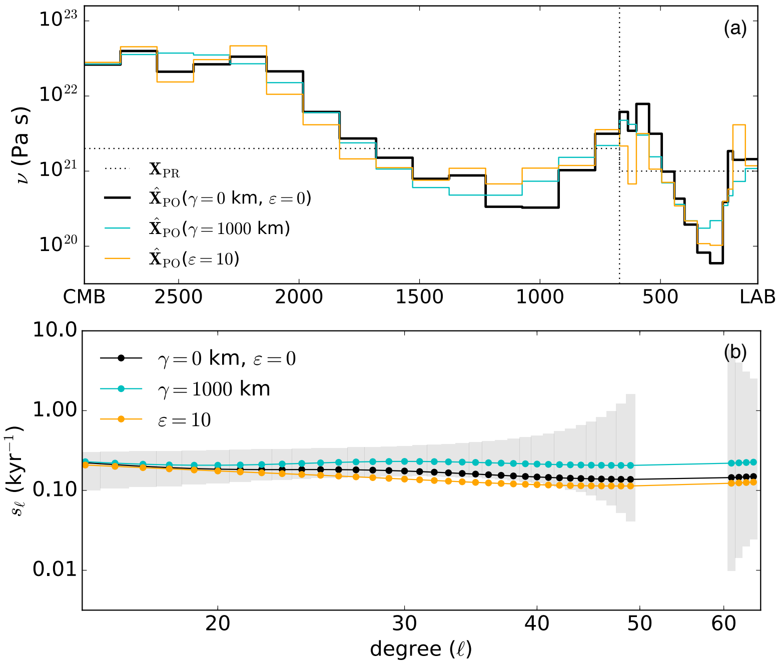

FIGURE 5.8: (a) Posterior models from nonlinear, Bayesian inversions where smoothing is included in the log-viscosity model parameters ($\gamma = 1000$ km; see eq. 5.14) or covariances are introduced between the FRS data ($\varepsilon = 10$; see eq. 5.15). For comparison, we reproduce the posterior model from Fig. 5.4 which adopted $\gamma = 0$ km and $\varepsilon = 0$. The horizontal axis marks depth (km) and the black dotted vertical line marks the boundary between the upper and lower mantle. (b) Predictions of the FRS using the posterior models from panel (a).

that parameter, and the extent of smoothing is controlled by the correlation length-scale γ. Fig. 5.8(a) shows an inversion where $\gamma = 1000$ km. For reference, we include $\mathbf{X}_{\rm PO}$ from Fig. 5.4 in which $\gamma = 0$ km. Note that covariances are confined to the 28 log-viscosity parameters and no smoothing is applied across the 670 km discontinuity. Not surprisingly, oscillations in the inverted model for this case are damped relative to the $\gamma = 0$ km case; in particular the asthenospheric viscosity is not as low. Note also that the inverted model has no viscosity jump at 670 km depth, suggesting that the data do not require a viscosity discontinuity at this depth. The inverted model fits all data sets included in the inversion; as an example, the fit to the FRS is shown in Fig. 5.8(b). Next, we add some

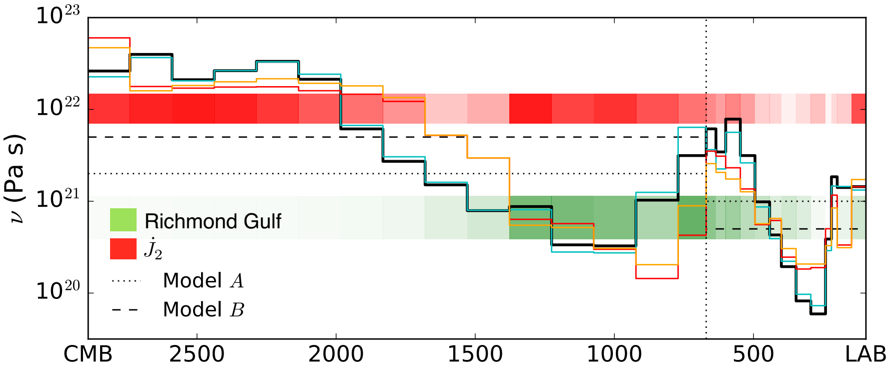

Figure 5.9: Nonlinear, Bayesian inversions adopting various starting and prior viscosity models. The black line reproduces the inversion in Fig. 5.4 which adopted Model A as the prior and starting model. The cyan and orange lines repeat this inversion with the exception that Model B (Table 5.1) is adopted as either the prior or starting model, respectively. The red line is the result of an inversion where Model B is both the starting and prior model. The color bands are weighted averages ($\bar{\mathbf{F}}_i^T \mathbf{X}_{\text{PO}}$; eq. 5.11) of the inverted model (red line), where the weightings are normalized and volumetrically scaled posterior Fréchet kernels for Richmond Gulf and $\dot{J}_2$. The horizontal axis marks depth (km) and the black dotted vertical line marks the boundary between the upper and lower mantle.

covariance to the 39 FRS data points by updating entries of $\mathbf{V}_\xi$ associated with the FRS as follows:

$$[V_\xi]_{mn} = \sigma(m)\sigma(n)e^{-\|\ell(m)-\ell(n)\|\varepsilon^{-1}} \tag{5.15}$$

where the extent of smoothing is controlled by ε and $\ell(m)$ is the spherical harmonic degree associated with data point m. Fig. 5.8(a) shows an inversion where we adopt $\varepsilon = 10$. Introducing a correlation between the FRS effectively down-weights the importance of the FRS in the inversion, and this leads to a somewhat degraded fit of the model to these data. Specifically, the asthenospheric viscosity dip is suppressed resulting in predictions of the FRS (where $21 \leq \ell \leq 42$) that are too low. The fits to the decay time and $\dot{J}_2$ rate are unaffected since these data do not resolve structure on this spatial scale (see Fig. 5.4).

Next, we explore the impact on the inversions of changing the *a priori* and starting models. Fig. 5.9 reproduces the model in Fig. 5.4, which was derived from an inversion using Model A of

Table 5.1 as both the prior and starting model. The figure also shows the results of three further inversions in which Model B replaced Model A as the prior model (cyan line) or starting model (orange line). The red line represents an inversion where both the prior and starting models are Model B. The prior covariance matrix is unaltered from the case in Fig. 5.4; that is, the variance values are unchanged and no smoothing is incorporated into the inversions. Changing the prior model has little impact on the inversion, and thus, in the nomenclature of Bayesian inverse theory, the prior models adopted here are non-informative.

In contrast, changing the starting model does impact the inversion, particularly in the lower mantle: just beneath the 670 km discontinuity the inversions adopting Model B as a starting model (red and orange lines) dip to viscosities of $\sim 10^{20}$ Pa s but are followed by a more rapid rise in viscosity deeper into the mantle. The viscosity values plateau at $\sim 2 \times 10^{22}$ Pa s below 1900 km depth. As we have noted, a comparison of inverted profiles should not be based on a layer-by-layer comparison of model values, but rather should be based on averages that reflect the resolving power of the data. To this end, Fig. 5.9 shows two weighted averages of the posterior model ($\mathbf{F}_i{}^T\mathbf{X}_{\mathrm{PO}}$) for the inversion where Model B is adopted as both the starting and prior model, where the weightings reflect Fréchet kernels of the posterior model associated with the Richmond Gulf decay times (green) and $\dot{J}_2$ datum (red). These averages are consistent with analogous averages computed for the inversion where Model A is adopted as the starting and prior model (Fig. 5.4). We conclude that the inversion is insensitive to the starting model when one accounts for the resolving power of the data.

We have argued that the data sets adopted in our inversions are relatively insensitive to details of the ice history. To investigate this issue, Fig. 5.2 includes a set of forward predictions based on the ANU global ice reconstructions (Fleming & Lambeck, 2004) (green stars). This ice history is paired with the *a posteriori* viscosity model of Fig. 5.4 that was derived via an inversion that adopted the ICE-6G history. Discrepancies between the forward predictions of $\dot{J}_2$, post-glacial decay times and DSL highstands based on these ice histories are small compared to the uncertainties in the data,

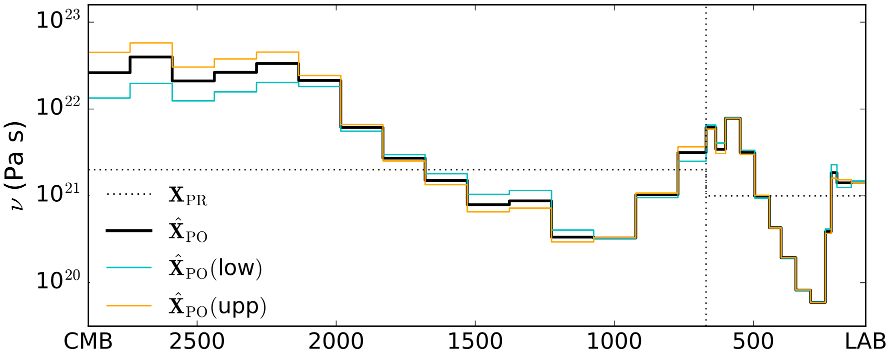

FIGURE 5.10: nonlinear, Bayesian inversions repeating the calculation in Fig. 5.4 (black line) but applying a different modern melt correction to the $\dot{J}_2$ datum. $\mathbf{X}_{\mathrm{PO}}$ (low) and $\mathbf{X}_{\mathrm{PO}}$ (upp) denote the posterior solutions associated with melt corrections of 1.5×10^{-11} y^{-1} and 2.5×10^{-11} y^{-1}, respectively. The horizontal axis marks depth (km) and the black dotted vertical line marks the boundary between the upper and lower mantle.

confirming that these data sets are relatively insensitive to details of the ice history. (We note, by definition, that the FRS is identical for both as this is a property of the posterior model alone.)

Finally, we also explore the sensitivity of our *a posteriori* model to the correction applied to the observed $\dot{J}_2$ signal to account for modern glacier and ice sheet melt over the period 1976–1990. As we have discussed, the $\dot{J}_2$ rate we estimated from Cheng et al. (2013) was $(-3.4 \pm 0.5) \times 10^{-11}$ y^{-1} and the correction for modern melt used in our previous inversions was $(2.0 \pm 0.5) \times 10^{-11}$ y^{-1}. In Fig. 5.10 we explore the impact on the *a posteriori* viscosity model of using modern melt corrections of 1.5×10^{-11} y^{-1} and 2.5×10^{-11} y^{-1}. In the three inversions shown on the figure, the peak viscosity in the lower mantle varies from $\sim 2 \times 10^{22}$ Pa s to $\sim 6 \times 10^{22}$ Pa s across this range of corrections. The mean viscosity across the bottom 1000 km of the mantle varies from 1.7×10^{22} Pa s to 3.8×10^{22} Pa s. We conclude that uncertainty in the melt correction maps into an uncertainty of a factor or ~ 2 in the mean viscosity of the deep mantle, and above this depth the sensitivity is negligible.

VISCOSITY STRUCTURE WITHIN THE LOWER MANTLE

The combination of decay time data, which constrain the average viscosity from the middle of the upper mantle to the top 500 km (Angerman River) and 1200 km (Richmond Gulf, James Bay) of the lower mantle to be $\sim 10^{21}$ Pa s, and the $\dot{J}_2$ datum, which requires a mean viscosity in the bottom half of the lower mantle of $\sim 10^{22}$ Pa s, drive inversions with a robust requirement for a significant increase of viscosity, with depth, in the lower mantle. This increase is consistent with inferences based on a joint inversion of GIA data and mantle convection observables (Mitrovica & Forte, 1997, 2004), which show a ~ 2 order of magnitude increase in viscosity from 670 km depth to the deep lower mantle. However, neither of these earlier inversions included the $\dot{J}_2$ datum, and the inference of a high viscosity deep mantle (and lower viscosity D" region) was, in those studies, driven by constraints associated with a set of convection-related observations.

Important early viscous flow modeling of mantle convection observables demonstrated that a viscosity jump in the shallow lower mantle provided a better fit to observational constraints on the long-wavelength non-hydrostatic geoid, plate motions and CMB topography, than a jump at the 670 km boundary between the upper and lower mantle (Forte, 1987; Forte et al., 1991). This suggestion was supported by a joint inversion of mantle convection and GIA observables (Mitrovica & Forte, 1997) and also by seismic evidence suggesting a boundary at ~ 920 km depth (Kawakatsu & Niu, 1994). Several recent studies have revisited the issue using a variety of data sets and they have added to the case for a viscosity jump at ~ 1000 km depth (Ballmer et al., 2015; Rudolph et al., 2015). The ice age data sets adopted in the present study are unable to resolve a sharp viscosity boundary at such depths, although it is possible from our results that such a boundary is not inconsistent with the constraints imposed by these data sets.

To explore this issue, we set up a large suite of forward calculations in which the upper mantle is prescribed to have the structure given by the inverted model in Fig. 5.4, and the lower mantle is discretized into two isoviscous layers. The boundary between these two lower mantle layers is systematically varied over a depth range of 770–1830 km, and for each location we consider a range of viscosity values above $(1.6\text{–}50)\times10^{20}$ Pa s and below $(1.6\text{–}100)\times10^{21}$ Pa s the boundary. We do not assume that the lower layer is more viscous than the upper layer. A total of 800 simulations were performed. We first culled from this set of simulations all models in which the predicted FRS did not fit the observational constraint; this was a relatively small number (43) since the FRS data are dominantly sensitive to upper mantle structure (Figs 5.3, 5.5), which was not varied. Next, for each depth of the boundary between the two lower mantle regions we determined the best-fitting pair of viscosity values above and below the boundary. The results of this Monte Carlo analysis are summarized in Fig. 5.11.

The vertical lines in Fig. 5.11(a) represent the best fit solutions when the lower mantle viscosity boundary is placed at the specified depth. The extreme values on each line provide the viscosity above and below the boundary that define this best fit model. (All best fit models are characterized by a more viscous lower layer relative to the upper layer within the lower mantle.) The vertical lines are drawn as solid when the best fit model satisfies all observational constraints, dashed when all but one decay time is fit, and dotted when more than one observation is misfit. Accordingly, the data sets can all be satisfied when the viscosity boundary is placed between $\sim$1200–1700 km depth. (The gray shading on the figure covers the depth range 800–1200 km, where previous studies cited above have inferred viscosity jumps.) The preferred viscosity in the upper layer of the lower mantle increases from $(2.3\text{–}7.4)\times10^{20}$ Pa s as the boundary is moved from 1200 km to 1700 km depth, and the viscosity jump across the boundary, which is $\sim$2 orders of magnitude, is required to fit the $\dot{J}_2$ datum. We note that the preferred range of depths for the viscosity boundary placed within the lower mantle is limited by the small number of free parameters in the suite of models considered in Fig. 5.11. Allowing the upper mantle viscosity to vary in the modeling, or adding more layers in the lower mantle, will broaden the range of depths where a sharp boundary can be introduced while

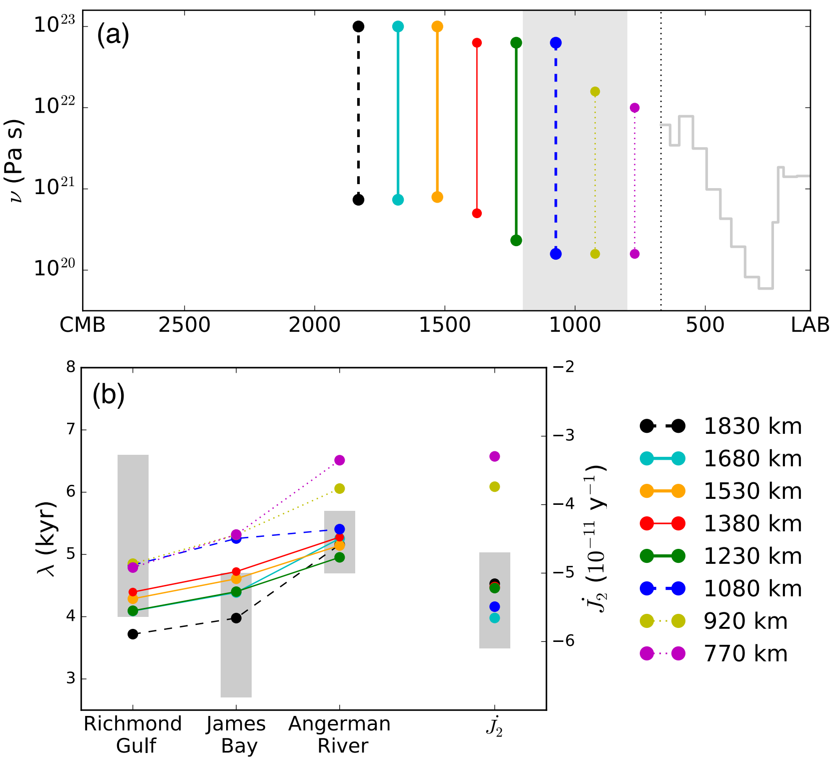

FIGURE 5.11: Results from a suite of 800 forward calculations distinguished on the basis of the adopted Earth model. In all calculations the upper mantle viscosity was fixed to the value obtained in the inversion shown in Fig. 5.4 (and shown here as a gray line with layering). The lower mantle was discretized into two layers. The free parameters of the modeling were: (1) the location of the viscosity boundary in the lower mantle, and (2) the viscosities in layers above and below this boundary (see text). (a) Vertical lines summarize the best fitting model for each of eight boundary locations (see legend at bottom right). The horizontal position of the line indicates the depth of the boundary, the upper and lower bound on each line provide the viscosity below and above the boundary, respectively, for the best fit model. Model results have been culled to include only those that fit the FRS observation. The data used in the misfit calculation includes the post-glacial decay times at Richmond Gulf, James Bay and Ångerman River and $\dot{J}_2$. The horizontal axis marks depth (km) and the black dotted vertical line marks the boundary between the upper and lower mantle. (b) The predictions of the decay time data and $\dot{J}_2$ for the best fit models summarized in frame A. In both frames, best fit models that yielded predictions that satisfied all the decay time constraints and the $\dot{J}_2$ datum are denoted by solid lines and those that misfit one or more of these constraints are denoted by dashed and dotted lines, respectively.

preserving a fit to the observations.

Various lines of evidence suggest that the viscosity of the D" region at the base of the mantle will be relatively low, including, e.g., *ab initio* methods (e.g., Ammann et al., 2010), geodetic observations

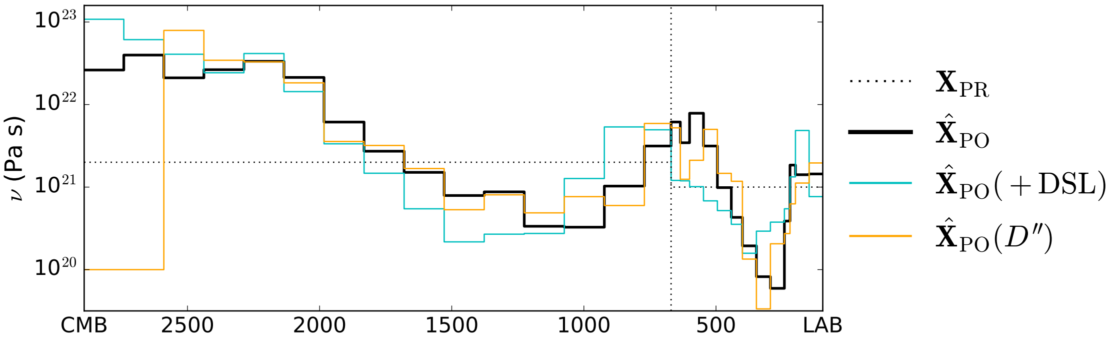

FIGURE 5.12: Results of several nonlinear, Bayesian inversions: $\hat{\mathbf{X}}_{\mathrm{PO}}$ is reproduced from Fig. 5.4. $\hat{\mathbf{X}}_{\mathrm{PO}}(+\mathrm{DSL})$ is the posterior model for an inversion identical to Fig. 5.4 except that the data set is augmented to include the three DSL observations shown in Fig. 5.2. $\hat{\mathbf{X}}_{\mathrm{PO}}(\mathrm{D''})$ is the result of an inversion identical to Fig. 5.4 except that the viscosity values in the two layers extending 300 km above the CMB are fixed to 10^{20} Pa s. The dotted black line is the starting and *a priori* model adopted in both inversions (Model A from Table 5.1). The horizontal axis marks depth (km) and the black dotted vertical line marks the boundary between the upper and lower mantle.

(Nakada & Karato, 2012), and previous joint inversions of GIA and mantle convection data sets (Mitrovica & Forte, 2004). We explored this issue by repeating the inversion in Fig. 5.4, but imposing a viscosity of 10^{20} Pa s in the mantle region extending up to 300 km above the CMB (this region corresponds to the deepest two layers of the discretized viscosity model). The *a posteriori* model in this case (orange line in Fig. 5.12) exhibits only minor differences from the original inversion, reinforcing our earlier argument that the data used in the inversion have limited resolving power in the deepest mantle (see Fig. 5.6h). This conclusion is in accord with the GIA analyses of Nakada et al. (2015a,b).

CONSISTENCY WITH DSL HIGHSTANDS

DSL highstand data have played an important role in inferences of mantle viscosity based on GIA data (Nakada & Lambeck, 1989). The inversions discussed above did not include the DSL highstand data summarized in Section 5.3.4. To investigate the consistency of the DSL highstand data to our earlier inversion, Fig. 5.2(c) shows predictions of the DSL highstand data computed using the viscosity profile in Fig. 5.4 (red line). The shading superimposed on this line encompasses a range of predictions obtained by running a series of forward calculations in which we varied the lithospheric thickness across the one-σ range inferred from this original inversion (i.e., $87\text{ km} \leq L \leq 107\text{ km}$) while keeping the viscosity profile unchanged . This posterior solution is able to provide a fit to the Port Pirie-Magnetic Island datum but misfits the other two DSL highstand data.

We next repeated the inversion of Fig. 5.4 with a data set that was augmented to explicitly include the three DSL highstand pairs. The only other change from the inversion in Fig. 5.4 is that we increased the prior standard deviation of the lithospheric thickness parameter to 50 km. The resulting viscosity profile is shown in Fig. 5.12 (labeled $\hat{\mathbf{X}}_{\mathrm{PO}}(+\mathrm{DSL})$) and the posterior estimate for L is (130 ± 50) km. The inverted profile in Fig. 5.12 shows the same trends as the original $\hat{\mathbf{X}}_{\mathrm{PO}}$; however, in comparison to this earlier inversion, the lithospheric thickness is significantly larger.

The posterior predictions based on $\hat{\mathbf{X}}_{\mathrm{PO}}(+\mathrm{DSL})$ are shown in Fig. 5.2 (orange triangles). The inverted model fits all data sets with the exception of the Rockingham Beach-Vaucluse DSL highstand pair. This result reveals an inconsistency that can be illustrated by considering the Serventy Island-Port Lincoln and the Rockingham Beach-Vaucluse pairs and their dominant sensitivity to variations in the lithospheric thickness. The predictions for these two pairs based on the starting model (black circles in Fig. 5.2) under-predict the observational data. Their associated Fréchet kernels (red and yellow circles in Fig. 5.3, respectively) indicate that an increase in L will produce changes in the predictions for each DSL highstand pair of opposing sign. Thus, perturbation in the starting value of the lithospheric thickness cannot yield a simultaneous fit to both DSL pairs. This inconsistency may reflect lateral variations in lithospheric thickness or mantle viscosity, or an underestimation of the observational uncertainties.

5.5 SUMMARY

Inferring the radial profile of mantle viscosity from the analysis of data sets related to glacial isostatic adjustment is a problem in geophysical research that extends back nearly a century, to the pioneering work of Daly (1925) and Haskell (1935). However, despite some consensus that GIA data sets are compatible with—and indeed prefer— a 1-D viscosity profile that increases by several orders of magnitude with depth from the base of the lithosphere to CMB (McConnell, 1968; Nakada & Lambeck, 1989; Mitrovica, 1996; Lambeck et al., 1998; Mitrovica & Forte, 2004), two recent viscosity profiles inferred in the literature (Argus et al., 2014; Lambeck et al., 2014; Nakada et al., 2015a) appear to be irreconcilable. In particular, whereas Lambeck et al. (2014) and Nakada et al. (2015a) advocate for a viscosity profile that increases from $1–2 \times 10^{20}$ Pa s in the upper mantle to $\sim 7 \times 10^{22}$ Pa s in the lower mantle, the VM5a model of Argus et al. (2014) is characterized by a significantly more muted increase, from 5×10^{20} Pa s at the LAB to 3×10^{21} Pa s above the CMB. Both models place their viscosity jump (or at least the bulk of this increase) at 670 km depth.

We have revisited the 1-D viscosity problem, and addressed this recent debate, by analyzing GIA data using a combination of forward predictions and inversions based on nonlinear Bayesian inference. Inferences of mantle viscosity based on observations related to GIA are complicated by uncertainties in the space-time history of ice cover since the Last Glacial Maximum, and to avoid (or at least minimize) this issue we have focused our analysis on parameterizations of these data sets that reduce the sensitivity to ice history. These data sets include site-specific, post-glacial decay times inferred from relative sea-level records in Hudson Bay and Sweden (e.g., Walcott, 1972; Mitrovica et al., 2000; Fang & Hager, 2002; Nordman et al., 2015), the Fennoscandian relaxation spectrum (e.g., Sauramo, 1958; McConnell, 1968; Wieczerkowski et al., 1999), differential sea-level highstands from the Australian region (e.g., Nakada & Lambeck, 1989; Kaufmann & Lambeck, 2002) and the rate of change of the degree two zonal harmonic of the Earth's geopotential, or $\dot{J}_2$ (e.g., Cheng et al., 2013).

Subsets of these data have been used in a number of previous viscosity inferences based on forward analyses and formal inversions (Mitrovica & Peltier, 1993a; Mitrovica, 1996; Kaufmann & Lambeck, 2002; Mitrovica & Forte, 2004; Peltier, 2004), but no study has simultaneously included all these data sets in a joint inversion for the mantle viscosity profile. Our overarching goal has been to address the robustness of these recent, seemingly incompatible inferences of the 1-D mantle viscosity profile by analyzing these data sets within a rigorous inverse formalism.

On the basis of our inversions, we conclude that mantle viscosity increases by at least two orders of magnitude with depth from the LAB to CMB. This inference (Fig. 5.4) is driven by a sequence of correlated constraints. In particular: the FRS constrains the mean upper mantle viscosity to a value of $\sim 3 \times 10^{20}$ Pa s; the Fennoscandian and Hudson Bay post-glacial decay times constrain the mean value of viscosity from the mid-upper mantle to mid-lower mantle to be $\sim 10^{21}$ Pa s, a requirement that encompasses the classic Haskell constraint on mantle viscosity (Haskell, 1935; Mitrovica, 1996); and, finally, the $\dot{J}_2$ datum constrains the mean viscosity in the bottom half of the lower mantle to be $\sim 10^{22}$ Pa s. Taken together, these constraints yield a viscosity in the lower mantle that peaks at $\sim\ 4 \times 10^{22}$ Pa s (with a mean value in excess of 5×10^{21} Pa s). We have demonstrated that this overall trend in mantle viscosity with depth is robust relative to the choice of starting and prior models adopted in the inversions.

Our inference is consistent with previous estimates of mantle viscosity based on GIA data sets (Nakada & Lambeck, 1989; Mitrovica, 1996; Lambeck et al., 1998; Kaufmann & Lambeck, 2002; Lambeck et al., 2014; Nakada et al., 2015a), but we emphasize three important issues. First, our constraint on mantle viscosity in the bottom half of the mantle is dominated by the pre-1990 trend in the $\dot{J}_2$ datum, an observable that has been corrected for the signal due to contemporaneous melting from glaciers (Vaughan et al., 2013). If this correction is robust, the $\dot{J}_2$ datum rules out a broad suite of studies that have inferred a deep mantle viscosity only moderately higher than 10^{21} Pa s (Peltier, 2004; Argus et al., 2014; Peltier et al., 2015). A similar conclusion was reached by Nakada et al. (2015a) and Mitrovica et al. (2015) using forward predictions of the $\dot{J}_2$ datum. Second, our inversions indicate that the GIA data sets we have considered can be reconciled by a mantle viscosity profile without a viscosity jump at 670 km depth. The GIA data do not have the resolving power to infer such a sharp increase, and previous inferences for a jump in viscosity at this depth are generally biased by coarse discretizations in which the upper and lower mantle are treated as isoviscous. A related issue was raised by Mitrovica (1996), who showed that two-layer (upper and lower mantle) parameterizations, combined with an incorrect assumption that the Haskell (1935) constraint on mantle viscosity resolved mean upper mantle structure, biased many previous inferences toward isoviscous mantle models. Finally, although the high deep mantle viscosity inferred in this study is dependent on the veracity of the $\dot{J}_2$ constraint, we note that the trend toward values of $\sim 10^{23}$ Pa s in Fig. 5.4 is consistent with results from joint inversions of GIA (not including the $\dot{J}_2$ datum) and mantle convection data sets (Forte & Mitrovica, 1996; Mitrovica & Forte, 1997, 2004). In these studies the latter data set provides the necessary deep mantle resolving power.

As we have discussed, a series of studies have suggested the possibility of a significant jump in viscosity in the shallow lower mantle (Forte, 1987; Forte et al., 1991; Mitrovica & Forte, 1997; Marquardt & Miyagi, 2015; Ballmer et al., 2015; Rudolph et al., 2015). As with the 670 km discontinuity, we cannot robustly argue for the existence of such a jump. However, we have explored this issue by presenting a large suite of forward calculations that varied the depth of such a boundary, as well as the viscosity above and below the boundary, and comparing the results to the FRS, decay time and $\dot{J}_2$ data. We conclude that these data are able to accommodate a viscosity jump of ~ 2 orders of magnitude at depths between 1000–1700 km.

Finally, our inversions of the GIA data sets described above have adopted Earth models in which mantle viscosity varies with depth alone. Although we have found that most of the data sets described in Section 5.3 can be reconciled with a 1-D mantle viscosity structure, our inability to simultaneously fit all DSL highstand data suggests that the possibility that lateral variations in mantle viscosity may be playing a role in one, or indeed all, of the GIA data sets we have considered here. In a future study we will extend the present analysis to investigate the potential bias in inferences of a 1-D mantle viscosity profile introduced by the presence of 3-D viscosity structure. The analysis will include, as an important subset, the GIA data considered here, but it will also consider an extensive global database of relative sea-level histories adopted in previous GIA-based inferences of the radial profile of mantle viscosity.

6

Conclusions and Future Work

To stand on this step
you must be in your own right
a member of the city of ideas.
–C.P. Cavafy

The motivation behind this thesis was to better understand the large-scale dynamics of the mantle, and this requires accurate knowledge of two parameters: the density and viscosity fields. Chapters 2–4 were dedicated to developing and applying a new technique to shed light on the long-wavelength density structure of the deep mantle. Chapter 5 focused on nonlinear Bayesian inversions of sea-level records and long-wavelength gravity data associated with GIA in order to constrain radial viscosity structure of the mantle in a manner consistent with the resolving power of each datum. The following sections summarize the key findings of this thesis and outline future steps to further our understanding of mantle dynamics.

6.1 TIDAL TOMOGRAPHY

A major component of this thesis involved the development and application of a new technique called "tidal tomography" whereby we imaged deep mantle density structure by inverting Earth's body tide deformation as measured by a global GPS network. In Chapter 2 we updated the established body tide theory developed by Wahr (1981b) to allow for asphericity in the form of rotation and lateral heterogeneity using normal mode perturbation theory (Lau et al., 2015) and we revised the theoretical treatment of anelasticity as derived by Wahr & Bergen (1986). In Chapter 4 we applied GPS-based measurements of crustal displacement associated with the so-called M2 body tide to invert for deep mantle buoyancy structure. In order to isolate the signal in the GPS observations

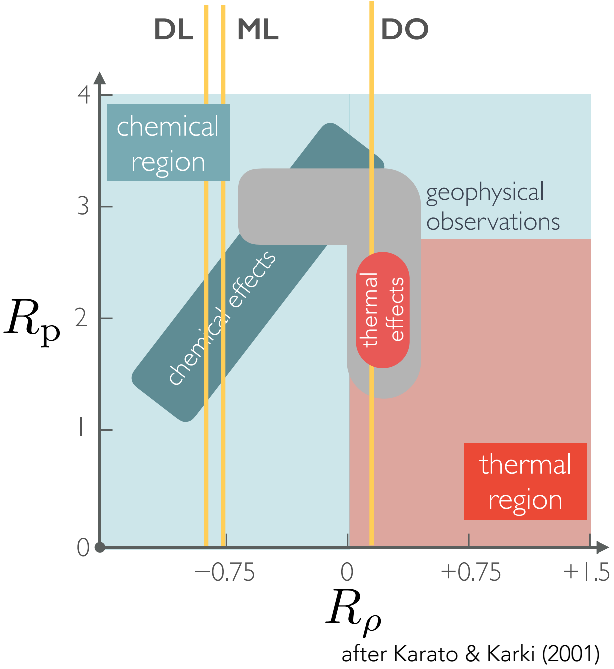
DL
ML
DO
chemical region
geophysical observations
chemical effects
thermal effects
thermal region
R_{p}
0
1
2
3
4
−0.75
0
+0.75
+1.5
R_ρ
after Karato & Karki (2001)

FIGURE 6.1: A schematic figure of $R_{\text{p}} - R_\rho$ space after Karato & Karki (2001). The gray region spans values of $R_{\text{p}} - R_\rho$ from geophysical observations in the deep mantle. The regions labeled "thermal" and "chemical effects" span values of $R_{\text{p}} - R_\rho$ from thermal and chemical effects, respectively, estimated by mineral physics experiments. The regions labeled "thermal region" and "chemical region" span values of $R_{\text{p}} - R_\rho$ theoretically inferred.

produced by laterally heterogeneous mantle structure, the GPS data were corrected for crustal and core-mantle boundary topography and ocean tidal loading. We concluded that the three regions considered in the analysis (the deep and mid LLSVP, and deep surrounding regions) are characterized by excess densities of $(0.61–0.74)\%$, $(0.44–0.64)\%$, and $(-0.04–-0.02)\%$, respectively (listed as interquartile ranges).

The excess density values within the LLSVPs can be unambiguously attributed to the existence of a compositionally-dense component relative to the surrounding mantle. This is best visualized by Fig. 6.1 which schematically shows where several observations lie in $R_\mathrm{p} - R_\rho$ space, where R_p is the scaling value between the P-wave speed, v_p, and v_s (or $R_\mathrm{p} = \delta v_\mathrm{p}/\delta v_\mathrm{s}$). All values are associated with the deep mantle region. Within this space, one can deduce whether the combined scaling values R_p and R_ρ are due to thermal or compositional effects. As can be seen, all possible values of R_p for the regions within the LLSVPs (marked “DL” and “ML” to denote the deep and mid layers of the LLSVPs in Fig. 6.1) require a compositional source to explain their large negative values of R_ρ. In contrast, the surrounding region (marked “DO” in Fig. 6.1) can be explained by both thermal or compositional effects, depending on the region’s R_p value.

This non-uniqueness motivates the next steps of this study. To obtain a bound on the R_p value of DO requires the introduction of data types with sensitivity to variations in P-wave speed and this would be best served by implementing a joint inversion with seismic data. Furthermore, to fine tune the 3-D spatial distribution of these density anomalies, a joint inversion of body tide and seismic normal mode data would provide complementary sensitivities to the deep mantle region.

6.2 THE FREQUENCY DEPENDENCE OF VISCOSITY

In Chapter 3 we focused on the theoretical treatment of the effects of anelasticity on the body tides. In Chapter 2 we showed that assuming that anelasticity would only perturb existing elastic normal modes—an assumption made in the traditional theory—was invalid, and that a rigorous treatment of the effect requires the inclusion of a new set of modes, which we term “relaxation modes”. This ammendment to the theory has implications for both the prediction and interpretation of body tides on an anelastic Earth. In Chapter 3 we explored these implications by imposing an idealistic Q-structure that adopts a simple frequency dependence. We showed that predictions of the phase lag of the body tide are subject to significant inaccuracy when using the traditional theory; but moreover, implicit in the traditional theory is the assumption that the planetary-scale observed phase lag is directly related to the intrinsic Q of the material. When effects of inertia, self-gravity, and energy are taken into consideration we demonstrated that this assumption can lead to biases in estimates of intrinsic Q and will invalidate estimates of the frequency dependence of intrinsic Q.

The parameter Q is a measure of dissipation and as such it has connection to the viscosity of the Earth. It is therefore important to note that these results will also have implications for the discussion of viscosity in Section 6.3. An important extension to this theoretical exploration would be to explore observational values of Q with this updated approach across a wide frequency band. A selection of processes could include the seismic normal modes ${}_0\mathcal{S}_3$ and ${}_0\mathcal{S}_2$ (with eigenfrequencies of $\sim$ 30 minutes^{-1} and $\sim$ 1 hour^{-1}, respectively), the M2 semi-diurnal body tide, the fortnightly body tide, the Chandler Wobble (with period of 430 days), and the 18.6 year body tide.

6.3 Laterally Heterogeneous Viscosity

In Chapter 5 we applied a nonlinear Bayesian inversion to data associated with GIA in order to constrain the radial viscosity profile of the mantle. We found that viscosity increases significantly with depth, with a deep mantle value constrained by the $\dot{J}_2$ datum after correction for modern melting. The GIA data can accommodate a viscosity jump in the lower mantle (across a depth range of 1000–1700 km) of 1–2 orders of magnitude. We were unable to find a radial viscosity model that simultaneously reconciles all differential sea-level highstand data (located across the Australian continent). This result motivates future directions for research related to mantle viscosity.

The GIA data available are geographically sparse and it is likely that the volumes within the Earth's interior that the data sample do not represent 'average' mantle. Rather, the radial profile we have inferred contains geographical bias. The geographical locations of our data, e.g., Hudson Bay, Scandinavia and Australia, lie in old, cratonic regions of the Earth and because of this will be sampling higher than average shallow viscosity regions and/or thicker than average lithosphere. Moreover, since lateral variations in viscosity likely reach many orders of magnitude (e.g., Latychev et al., 2005), this bias will be significant.

As a future study we will consider a simple exercise: using a finite volume code that solves the sea-level equation (Mitrovica & Milne, 2003) on an Earth model able to incorporate lateral variations in viscosity of several orders of magnitude (Latychev et al., 2005), we will reproduce the identical, though synthetic, data set used in Chapter 5 on an Earth with laterally varying viscosity structure (guided by seismic tomography models). Using this synthetic data, we will repeat the inversions in Chapter 5 but with the full knowledge of the true radial mantle viscosity. This exercise will explore the extent to which geographical bias affects estimates of radial viscosity profiles inferred from GIA data sets.

Furthermore, any forward calculation of GIA associated predictions on 3-D Earth models are computationally intensive given the large lateral variations in viscosity. The prospect of performing an inversion for 3-D viscosity structure becomes daunting as the calculation of $\mathbf{F}$ (see Chapter 5) is computationally expensive, scaling with the number of parameters to be solved for. The difficulties are further exacerbated by the nonlinear nature of the problem as $\mathbf{F}$ itself is a function of the viscosity profile. Efforts are currently being made, in colloration with colleagues at the University of Cambridge, to implement the adjoint method to the GIA problem. Using this method reduces the calculation of $\mathbf{F}$ to solving the forward problem and the so-called "adjoint" problem once, independent of the number of parameters of interest. This massive reduction in computational expense will allow for the calculation of 3-D sensitivity kernels so that the information content of the GIA data sets can be explored on an Earth model with more realistic rheological complexity. Such insight remains an important target and goal for global geophysics.

A

Mode Excitation by a Tidal Potential

The tidal potential, $\Psi(\mathbf{r};t)$, exerted at a site $\mathbf{r} = [r, \theta, \psi]$ by some celestial body of mass M_i located at $\mathbf{r}_i = [r_i(t), \theta_i(t), \psi_i(t)]$ is given by

$$\begin{aligned} \Psi(\mathbf{r};t) &= -\frac{GM_i}{\|\mathbf{r} - \mathbf{r}_i(t)\|} \\ &= -\frac{GM_i}{d_i} \sum_{\ell=0}^{\infty} \left(\frac{r}{d_i}\right)^{\ell} P_\ell(\cos\xi_i) \ , \end{aligned} \tag{A.1}$$

where $d_i = \|\mathbf{r} - \mathbf{r}_i(t)\|$ and the azimuth, ξ_i, between $\mathbf{r}$ and $\mathbf{r}_i$ is

$$\hat{\mathbf{r}} \cdot \hat{\mathbf{r}}_i = \cos\xi_i = \cos\theta\cos\theta_i + \sin\theta\sin\theta_i\cos(\psi - \psi_i) \ . \tag{A.2}$$

$P_\ell(x)$ is the Legendre polynomial of degree ℓ (or the associated Legendre function of order 0). We may express Ψ as

$$\Psi(\mathbf{r};t) = H_i(t) \sum_{\ell=0}^{\infty} \left(\frac{r}{d_i}\right)^{\ell} P_\ell(\cos\xi_i) \ , \tag{A.3}$$

where $H_i = -GM_i/d_i(t)$. Ψ may also be expressed this as in eq. (3.27), where

$$c_{\ell m} = H_i \left(\frac{4\pi}{2\ell+1}\right) Y_{\ell m}{}^{*}(\theta_i, \psi_i) \ . \tag{A.4}$$

To arrive at eq. (3.30) from eq. (3.29), we begin by substituting expressions for $\mathbf{s}_k$ (eq. 3.28) and Ψ (eq. 3.27) into the following expression

$$\mathcal{J} = \sum_{n}^{\infty}\sum_{\ell}^{\infty}\sum_{m}^{\infty} {}_n\mathbf{s}_{\ell m}(\mathbf{r}) \int \rho(r')\,{}_n\mathbf{s}_{\ell m}{}^{*}(\mathbf{r}') \cdot \nabla\Psi_{\ell m}(\mathbf{r};t)\,\mathrm{d}V' \ , \tag{A.5}$$

which yields

$$\begin{aligned} {}_n\mathcal{J}_{\ell m} = \left({}_nU_\ell\, Y_{\ell m}\hat{\mathbf{r}} + \frac{{}_nV_\ell}{\sqrt{\ell(\ell+1)}}\nabla_1 Y_{\ell m}\right) \cdot \int \rho(\mathbf{r}') \left[{}_nU_\ell\, Y_{\ell m}{}^{*}\hat{\mathbf{r}} + \frac{{}_nV_\ell}{\sqrt{\ell(\ell+1)}}\nabla_1 Y_{\ell m}{}^{*}\right] \cdot \\ H_i \left(\frac{4\pi}{2\ell+1}\right) Y_{\ell m}{}^{*}(\theta_i,\psi_i) \exp[i\omega_T t]\, \frac{r^{\ell-1}}{a^{\ell}} \left[\ell\, Y_{\ell m}\hat{\mathbf{r}} + \sqrt{\ell(\ell+1)}\nabla_1 Y_{\ell m}\right] \mathrm{d}V' \ . \end{aligned} \tag{A.6}$$

We have dropped the eigenfunction dependence on m due to the spherical symmetry of the Earth model. Using the following relations

$$\int_A Y_{\ell m}\hat{\mathbf{r}} \cdot Y_{\ell' m'}{}^{*}\,\hat{\mathbf{r}}\,\mathrm{d}A = \delta_{\ell\ell'}\delta_{mm'} \ , \tag{A.7}$$

and

$$\int_A \frac{(\nabla_1 Y_{\ell m}) \cdot (\nabla_1 Y_{\ell' m'}{}^*)}{\sqrt{\ell(\ell+1)}\sqrt{\ell'(\ell'+1)}}\, \mathrm{d}A = \delta_{\ell\ell'}\delta_{mm'} \ , \tag{A.8}$$

where A represents the unit area of a sphere, eq. (A.6) simplifies to

$$\begin{aligned} {}_n\mathcal{J}_{\ell m} = &\left({}_nU_\ell\, Y_{\ell m}\hat{\mathbf{r}} + \frac{{}_nV_\ell}{\sqrt{\ell(\ell+1)}} \nabla_1 Y_{\ell m} \right) \times \\ &H_i \left(\frac{4\pi}{2\ell+1} \right) Y_{\ell m}{}^*(\theta_i, \psi_i) \exp(i\omega_T t) \int \rho(r) \frac{r^{\ell-1}}{a^\ell} \left[\ell_n U_\ell + \sqrt{\ell(\ell+1)}_n V_\ell \right] \mathrm{d}r \ . \end{aligned} \tag{A.9}$$

To compute the amplitude of the tidal response, we evaluate $Y_{\ell m}$ at $[\theta_i, \psi_i]$. Using the identity

$$P_\ell(\cos\theta_i) = \left(\frac{4\pi}{2\ell+1} \right) \sum_{m=-\ell}^{\ell} Y_{\ell m}(\theta_i, \psi_i) Y_{\ell m}{}^*(\theta_i, \psi_i) \ , \tag{A.10}$$

yields

$$\begin{aligned} {}_n\mathcal{J}_\ell = H_i &\left({}_nU_\ell\, P_\ell(\cos\theta_i)\hat{\mathbf{r}} + \frac{{}_nV_\ell\, \nabla_1 P_\ell(\cos\theta_i)}{\sqrt{\ell(\ell+1)}} \right) \times \\ &\int \rho(r) \frac{r^{\ell-1}}{a^\ell} \left[\ell_n U_\ell + \sqrt{\ell(\ell+1)}_n V_\ell \right] \mathrm{d}r \ \exp[i\omega_T t] \ . \end{aligned} \tag{A.11}$$

Finally, applying the expression for the tidal potential given by eq. (A.3) results in

$$\begin{aligned}\mathcal{J}_\ell = \sum_n \Bigg\{ & {}_nU_\ell(r) \int \rho(r) \frac{r^{\ell+1}}{a^\ell} \left[\ell\, {}_nU_\ell(r) + \sqrt{\ell(\ell+1)}\, {}_nV_\ell(r)\right] \mathrm{d}r \; \Psi_\ell(\mathbf{r})\, \hat{\mathbf{r}} \\ & \frac{{}_nV_\ell(r)}{\sqrt{\ell(\ell+1)}} \int \rho(r) \frac{r^{\ell+1}}{a^\ell} \left[\ell\, {}_nU_\ell(r) + \sqrt{\ell(\ell+1)}\, {}_nV_\ell(r)\right] \mathrm{d}r \; \nabla_1 \Psi_\ell(\mathbf{r}) \Bigg\} \exp[i\omega_T t] \ . \end{aligned} \tag{A.12}$$

B

Extracting Q^{-1} From $h(\omega)$

To arrive at eq. (3.56) recall the definition of $\check{Q}^{-1}$ given by eq. (3.51). To extract the real and imaginary parts of $h(\omega)$ we begin by rationalizing the denominator of eq. (3.56) where

$$(\bar{\omega}_n{}^2 + \varepsilon_n{}^2)(\bar{\omega}_n{}^2 + \varepsilon_n{}^2)^* = (\bar{\omega}_n{}^2 + \mathrm{Re}\{\varepsilon_n{}^2\})^2 + \mathrm{Im}\{\varepsilon_n{}^2\}^2 \ . \tag{B.1}$$

Ignoring second-order terms involving $\mathrm{Re}\{\varepsilon_n{}^2\}$ (where $\mathrm{Re}\{\varepsilon_n{}^2\} \ll \bar{\omega}_n{}^2$) we find that

$$(\bar{\omega}_n{}^2 + \varepsilon_n{}^2)(\bar{\omega}_n{}^2 + \varepsilon_n{}^2)^* \approx \bar{\omega}_n{}^4 + \mathrm{Im}\{\varepsilon_n{}^2\}^2 \tag{B.2}$$

Thus,

$$h_k(\omega) = \frac{1}{g}\chi_k \left[\bar{\omega}_k{}^2 + \mathrm{Re}\{\varepsilon_k{}^2\} + i\mathrm{Im}\{\varepsilon_k{}^2\}\right] \ , \tag{B.3}$$

where

$$\chi_k = \frac{1}{\bar{\omega}_k{}^4 + \mathrm{Im}\{\varepsilon_k{}^2\}^2} \int_0^a \rho(r) \frac{r^{\ell+1}}{a^\ell} \left[\ell_n \bar{U}_\ell(r) + \sqrt{\ell(\ell+1)}_n \bar{V}_\ell(r) \right] \, \mathrm{d}r. \tag{B.4}$$

From the definition of ε^2 (eq. 3.38) and using eq. (3.11) (ignoring gravity-related terms), we see that

$$\mathrm{Re}\{\langle \bar{\mathbf{s}}_k, \delta\mathcal{H}(\omega_T)\bar{\mathbf{s}}_k \rangle\} = \int_V \nabla \mathbf{s}_k{}^* : \mathrm{Re}\{\delta\mathbf{\Lambda}(\omega_T)\} : \nabla \mathbf{s}_k \, \mathrm{d}V \ , \tag{B.5}$$

$$\mathrm{Im}\{\langle \bar{\mathbf{s}}_k, \delta\mathcal{H}(\omega_T)\bar{\mathbf{s}}_k \rangle\} = \int_V \nabla \mathbf{s}_k{}^* : \mathrm{Im}\{\delta\mathbf{\Lambda}(\omega_T)\} : \nabla \mathbf{s}_k \, \mathrm{d}V \ , \tag{B.6}$$

where $\mathrm{Im}\{\delta\mathbf{\Lambda}(\omega)\} = \mathrm{Im}\{\mathbf{\Lambda}(\omega)\}$.

References

Agnew, D. (2007). *Treatise on Geophysics*. Elsevier.

Agnew, D. C. (1997). NLOADF: A program for computing ocean-tide loading. *Journal of Geophysical Research: Solid Earth*, 102(B3), 5109–5110.

Al-Attar, D. (2007). A solution of the elastodynamic equation in an anelastic earth model. *Geophysical Journal International*, 171(2), 755–760.

Al-Attar, D., Woodhouse, J. H., & Deuss, A. (2012). Calculation of normal mode spectra in laterally heterogeneous earth models using an iterative direct solution method. *Geophysical Journal International*, 189(2), 1038–1046.

Allègre, C. J., Hofmann, A., & O'Nions, K. (1996). The Argon Constraints on Mantle Structure. *Geophysical Research Letters*, 23(24), 3555–3557.

Alterman, Z., Jarosch, H., & Pekeris, C. L. (1959). Oscillations of the Earth. *Proceedings of the Royal Society A: Mathematical, Physical and Engineering Sciences*, 252(1268), 80–95.

Ammann, M. W., Brodholt, J. P., Wookey, J., & Dobson, D. P. (2010). First-principles constraints on diffusion in lower-mantle minerals and a weak D" layer. *Nature*, 465(7297), 462–5.

Anderson, D. L. & Minster, J. B. (1979). The Frequency Dependence of Q in the Earth and Implications for Mantle Rheology and Chandler Wobble. *Geophysical Journal International*, 58(2), 431–440.

Argus, D. F., Peltier, W. R., Drummond, R., & Moore, A. W. (2014). The Antarctica component of postglacial rebound model ICE-6G_C (VM5a) based on GPS positioning, exposure age dating of ice thicknesses, and relative sea level histories. *Geophysical Journal International*, 198(1), 537–563.

Backus, G. E. (1988). Bayesian inference in geomagnetism. *Geophysical Journal International*, 92(1), 125–142.

Ballmer, M. D., Schmerr, N. C., Nakagawa, T., & Ritsema, J. (2015). Compositional mantle layering revealed by slab stagnation at ∼1000-km depth. *Science Advances*, 1(11), e1500815–e1500815.

Barnhoorn, A., Jackson, I., Fitz Gerald, J. D., & Aizawa, Y. (2007). Suppression of elastically accommodated grain-boundary sliding in high-purity MgO. *Journal of the European Ceramic Society*, 27(16), 4697–4703.

Bellis, C. & Holtzman, B. (2014). Sensitivity of seismic measurements to frequency-dependent attenuation and upper mantle structure: An initial approach. *Journal of Geophysical Research: Solid Earth*, 119(7), 5497–5517.

Belperio, A., Harvey, N., & Bourman, R. (2002). Spatial and temporal variability in the Holocene sea-level record of the South Australian coastline. *Sedimentary Geology*, 150(1-2), 153–169.

Benjamin, D., Wahr, J., Ray, R. D., Egbert, G. D., & Desai, S. D. (2006). Constraints on Mantle Anelasticity from Geodetic Observations, and Implications for the J_2 Anomaly. *Geophysical Journal International*, 165(1), 3–16.

Bolton, H. (1996). *Long Period Travel Times and the Structure of the Mantle*. PhD thesis, U. C. San Diego.

Brandenburg, J., Hauri, E. H., van Keken, P. E., & Ballentine, C. J. (2008). A multiple-system study of the geochemical evolution of the mantle with force-balanced plates and thermochemical effects. *Earth and Planetary Science Letters*, 276(1-2), 1–13.

Brodholt, J. P., Helffrich, G., & Trampert, J. (2007). Chemical versus thermal heterogeneity in the lower mantle: The most likely role of anelasticity. *Earth and Planetary Science Letters*, 262(3-4), 429–437.

Burke, K. (2011). Plate Tectonics, the Wilson Cycle, and Mantle Plumes: Geodynamics from the Top. *Annual Review of Earth and Planetary Sciences*, 39(1), 1–29.

Cartwright, D. E. & Edden, A. C. (1973). Corrected Tables of Tidal Harmonics. *Geophysical Journal International*, 33(3), 253–264.

Cartwright, D. E. & Petit, J.-M. (2004). IERS Conventions (2003). *International Earth Rotation and Reference Systems Service*.

Cathles, L. M. (1975). *Viscosity of the Earth's Mantle*, volume 9. Princeton University Press.

Cheng, M., Tapley, B. D., & Ries, J. C. (2013). Deceleration in the Earth's oblateness. *Journal of Geophysical Research: Solid Earth*, 118(2), 740–747.

Cheng, Y. & Andersen, O. B. (2010). *Improvement in global ocean tide model in shallow water regions* [Poster] (pp. 1–68).

Christensen, U. R. & Hofmann, A. W. (1994). Segregation of subducted oceanic crust in the convecting mantle. *Journal of Geophysical Research*, 99(B10), 19867.

Clark, P. U., Dyke, A. S., Shakun, J. D., Carlson, A. E., Clark, J., Wohlfarth, B., Mitrovica, J. X., Hostetler, S. W., & McCabe, A. M. (2009). The Last Glacial Maximum. *Science*, 325(5941), 710–714.

Cogley, J. G. (2009). Geodetic and direct mass-balance measurements: comparison and joint analysis. *Annals of Glaciology*, 50(50), 96–100.

Collins, L. B., Zhao, J.-X., & Freeman, H. (2006). A high-precision record of mid-late Holocene sea-level events from emergent coral pavements in the Houtman Abrolhos Islands, southwest Australia. *Quaternary International*, 145-146, 78–85.

Dahlen, F. A. (1968). The Normal-Modes of a Rotating, Elliptical Earth. *Geophysical Journal International*, 16(4), 329–367.

Dahlen, F. A. (1972). Elastic velocity anisotropy in the presence of an anisotropic initial stress. *Bulletin of the Seismological Society of America*, 62(5), 1183–1193.

Dahlen, F. A. & Tromp, J. (1998). *Theoretical Global Seismology*. Princeton University Press.

Daly, R. A. (1925). Pleistocene changes of level. *American Journal of Science*, s5-10(58), 281–313.

Davaille, A. (1999). Simultaneous Generation of Hotspots and Superswells by Convection in a Heterogeneous Planetary Mantle. *Nature*, 402(6763), 756–760.

Davies, D. R., Goes, S., Davies, J., Schuberth, B., Bunge, H.-P., & Ritsema, J. (2012). Reconciling dynamic and seismic models of Earth's lower mantle: The dominant role of thermal heterogeneity. *Earth and Planetary Science Letters*, 353-354, 253–269.

Day, W. A. (1971a). Restrictions on Relaxation Functions in Linear Viscoelasticity. *The Quarterly Journal of Mechanics and Applied Mathematics*, 24(4), 487–497.

Day, W. A. (1971b). Time-reversal and the symmetry of the relaxation function of a linear viscoelastic material. *Archive for Rational Mechanics and Analysis*, 40(3), 155–159.

Dehant, V. (1987). Tidal Parameters for an Inelastic Earth. *Physics of the Earth and Planetary Interiors*, 49(1-2), 97–116.

Dehant, V., Defraigne, P., & Wahr, J. M. (1999). Tides for a Convective Earth. *Journal of Geophysical Research*, 104(B1), 1035.

Deuss, A. & Woodhouse, J. (2004). Iteration method to determine the eigenvalues and eigenvectors of a target multiplet including full mode coupling. *Geophysical Journal International*, 159(1), 326–332.

Deuss, A. & Woodhouse, J. H. (2001). Theoretical Free-Oscillation Spectra: The Importance of Wide Band-Coupling. *Geophysical Journal International*, 146(3), 833–842.

Donner, J. (1980). *The determination and dating of synchronous Late Quaternary shorelines in Fennoscandia*. John Wiley & Sons.

Durek, J. J. & Ekstrom, G. (1996). A radial model of anelasticity consistent with long-period surface-wave attenuation. *Bulletin of the Seismological Society of America*, 86(1A), 144–158.

Dziewonski, A. M. & Anderson, D. L. (1981). Preliminary Reference Earth Model. *Physics of the Earth and Planetary Interiors*, 25(4), 297–356.

Edmonds, A. R. (1960). *Angular Momentum in Quantum Mechanics*. Princeton University Press.

Efroimsky, M. (2012). Tidal dissipation compared to seismic dissipation: In small bodies, earths, and super-earths. *The Astrophysical Journal*, 746(2), 150.

Efroimsky, M. (2013). Erratum: "Tidal Dissipation Compared to Seismic Dissipation: In Samll Bodies, Earths, and Super-Earths" (2012, ApJ, 746, 150) *The Astrophysical Journal*, 763(2), 150.

Egbert, G. D., Erofeeva, S. Y., Egbert, G. D., & Erofeeva, S. Y. (2002). Efficient Inverse Modeling of Barotropic Ocean Tides. *Journal of Atmospheric and Oceanic Technology*, 19(2), 183–204.

Fang, M. & Hager, B. H. (2002). On the apparent exponential relaxation curves at the central regions of the last pleistocene ice sheets. *Ice Sheets, Sea Level and the Dynamic Earth*, (pp. 201–218).

Farrell, W. E. (1972). Deformation of the Earth by Surface Loads. *Reviews of Geophysics*, 10(3), 761.

Faul, U. & Jackson, I. (2015). Transient Creep and Strain Energy Dissipation: An Experimental Perspective. *Annual Review of Earth and Planetary Sciences*, 43(1), 541–569.

Fleming, K. & Lambeck, K. (2004). Constraints on the Greenland Ice Sheet since the Last Glacial Maximum from sea-level observations and glacial-rebound models. *Quaternary Science Reviews*, 23(9), 1053–1077.

Forte, A. (1987). Plate tectonics and a spherical structure: The importance of poloidal-toroidal coupling. *Journal of Geophysical Research*, 92, 3645–3679.

Forte, A. M. & Mitrovica, J. X. (1996). New inferences of mantle viscosity from joint inversion of long-wavelength mantle convection and post-glacial rebound data. *Geophysical Research Letters*, 23(10), 1147–1150.

Forte, A. M. & Mitrovica, J. X. (2001). Deep-Mantle High-Viscosity Flow and Thermochemical Structure Inferred from Seismic and Geodynamic Data. *Nature*, 410(6832), 1049–56.

Forte, A. M., Peltier, W. R., & Dziewonski, A. M. (1991). Inferences of mantle viscosity from tectonic plate velocities. *Geophysical Research Letters*, 18(9), 1747–1750.

Ganino, C. & Arndt, N. T. (2009). Climate changes caused by degassing of sediments during the emplacement of large igneous provinces. *Geology*, 37(4), 323–326.

Gilbert, F. (1970). Excitation of the Normal Modes of the Earth by Earthquake Sources. *Geophysical Journal International*, 22(2), 223–226.

Gilbert, F. (1971). Excitation of the Normal Modes of the Earth by Earthquake Sources. *Geophysical Journal International*, 22(2), 223–226.

Gilbert, F. & Dziewonski, A. M. (1975). An Application of Normal Mode Theory to the Retrieval of Structural Parameters and Source Mechanisms from Seismic Spectra. *Philosophical Transactions of the Royal Society A: Mathematical, Physical and Engineering Sciences*, 278(1280), 187–269.

Gribb, T. T. & Cooper, R. F. (1998). Low-frequency shear attenuation in polycrystalline olivine: Grain boundary diffusion and the physical significance of the Andrade model for viscoelastic rheology. *Journal of Geophysical Research: Solid Earth*, 103(B11), 27267–27279.

Gurnis, M., Mitrovica, J. X., Ritsema, J., & van Heijst, H.-J. (2000). Constraining Mmantle Density Structure using Geological Evidence of Surface Uplift Rates: The Case of the African Superplume. *Geochemistry, Geophysics, Geosystems*, 1(7), n/a–n/a.

Hager, B. H., Clayton, R. W., Richards, M. A., Comer, R. P., & Dziewonski, A. M. (1985). Lower Mantle Heterogeneity, Dynamic Topography and the Geoid. *Nature*, 313, 541–545.

Hager, B. H. & Richards, M. A. (1989). Long-Wavelength Variations in Earth's Geoid: Physical Models and Dynamical Implications. *Philosophical Transactions of the Royal Society A: Mathematical, Physical and Engineering Sciences*, 328(1599), 309–327.

Hara, T., Tsuboi, S., & Geller, R. J. (1993). Inversion for laterally heterogeneous upper mantle S-wave velocity structure using iterative waveform inversion. *Geophysical Journal International*, 115(3), 667–698.

Hardy, L. (1976). *Contribution à l'étude géomorphologique de la portion québécoise des basses terres de la baie de James*. PhD thesis, McGill University, Montreal.

Haskell, N. A. (1935). The Motion of a Viscous Fluid Under a Surface Load. *Physics*, 6(8), 265.

Herring, T. A. & Dong, D. (1994). Measurement of Diurnal and Semi-Diurnal Rotational Variations and Tidal Parameters of Earth. *Journal of Geophysical Research*, 99(B9), 18051.

Hofmann, A. W. (1997). Mantle Geochemistry: the Message from Oceanic Volcanism. *Nature*, 385(6613), 219–229.

Houser, C., Masters, G., Shearer, P., & Laske, G. (2008). Shear and compressional velocity models of the mantle from cluster analysis of long-period waveforms. *Geophysical Journal International*, 174(1), 195–212.

Ishii, M. & Tromp, J. (1999). Normal-Mode and Free-Air Gravity Constraints on Lateral Variations in Velocity and Density of Earth's Mantle. *Science*, 285(5431), 1231–1236.

Ito, T. & Simons, M. (2011). Probing Asthenospheric Density, Temperature, and Elastic Moduli Below the Western United States. *Science (New York, N.Y.)*, 332(6032), 947–51.

Ivins, E. R., Sammis, C. G., & Yoder, C. F. (1993). Deep mantle viscous structure with prior estimate and satellite constraint. *Journal of Geophysical Research*, 98(B3), 4579.

Jackson, I. (1993). Progress in the Experimental Study of Seismic Wave Attenuation. *Annual Review of Earth and Planetary Sciences*, 21(1), 375–406.

Jackson, I. & Faul, U. H. (2010). Grainsize-sensitive viscoelastic relaxation in olivine: Towards a robust laboratory-based model for seismological application. *Physics of the Earth and Planetary Interiors*, 183(1-2), 151–163.

Jackson, I., Fitzgerald, J. D., Faul, U. H., & Tan, B. H. (2002). Grain-Size-Sensitive Seismic Wave Attenuation in Polycrystalline Olivine. *Journal of Geophysical Research*, 107(B12), 2360.

Kanamori, H. & Anderson, D. L. (1977). Importance of Physical Dispersion in Surface Wave and Free Oscillation Problems: Review. *Reviews of Geophysics*, 15(1), 105.

Karato, S. (1993). Importance of anelasticity in the interpretation of seismic tomography. *Geophysical Research Letters*, 20(15), 1623.

Karato, S.-i. & Karki, B. B. (2001). Origin of Lateral Variation of Seismic Wave Velocities and Density in the Deep Mantle. *Journal of Geophysical Research*, 106(B10), 21771.

Kaufmann, G. & Lambeck, K. (2002). Glacial isostatic adjustment and the radial viscosity profile from inverse modeling. *Journal of Geophysical Research*, 107(B11), 2280.

Kawakatsu, H. & Niu, F. (1994). Seismic evidence for a 920-km discontinuity in the mantle. *Nature*, 371(6495), 301–305.

Kellogg, L. H., Hager, B. H., & van der Hilst, R. (1999). Compositional Stratification in the Deep Mantle. *Science*, 283(5409), 1881–1884.

Kendall, R. & Mitrovica, J. (2007). Radial resolving power of far-field differential sea-level highstands in the inference of mantle viscosity. *Geophysical Journal International*, 171, 881–889.

Kendall, R. A., Mitrovica, J. X., & Milne, G. A. (2005). On post-glacial sea level - II. Numerical formulation and comparative results on spherically symmetric models. *Geophysical Journal International*, 161(3), 679–706.

Kim, T.-H. & Shibuya, K. (2013). Verification of the ellipsoidal earth model with an inelastic and convective mantle using tidal gravity variations revisited. *Geophysical Journal International*, 194(1), 230–248.

King, S. D. & Masters, G. (1992). An inversion for radial viscosity structure using seismic tomography. *Geophysical Research Letters*, 19(15), 1551–1554.

Kirschvink, J. L., Ripperdan, R. L., & Evans, D. A. (1997). Evidence for a Large-Scale Reorganization of Early Cambrian Continental Masses by Inertial Interchange True Polar Wander. *Science*, 277(5325), 541–545.

Kjeldsen, K., Korsgaard, N., Bjø rk, A., Khan, S., Box, J., Funder, S., Larsen, N., Bamber, J., Colgan, W., van den Broeke, M., Siggaard-Andersen, M.-L., Nuth, C., Schomacker, A., Andresen, C., Willerslev, E., & Kjæ r, K. (2015). Spatial and temporal distribution of mass loss from the Greenland Ice Sheet since AD 1900. *Nature*, 528(7582), 396–400.

Koelemeijer, P. J., Deuss, A., & Trampert, J. (2012). Normal mode sensitivity to Earth's D" layer and topography on the core-mantle boundary: what we can and cannot see. *Geophysical Journal International*, 190(1), 553–568.

Krásná, H., Böhm, J., & Schuh, H. (2013). Tidal Love and Shida numbers estimated by geodetic VLBI. *Journal of Geodynamics*, 70, 21–27.

Kump, L. R., Kasting, J. F., & Barley, M. E. (2001). Rise of atmospheric oxygen and the "upside-down" Archean mantle. *Geochemistry, Geophysics, Geosystems*, 2(1).

Kuo, C. & Romanowicz, B. (2002). On the resolution of density anomalies in the Earth's mantle using spectral fitting of normal-mode data. *Geophysical Journal International*, 150(1), 162–179.

Kustowski, B., Ekström, G., & Dziewoński, A. M. (2008). Anisotropic shear-wave velocity structure of the Earth's mantle: A global model. *Journal of Geophysical Research*, 113(B6), B06306.

Lambeck, K. & Chappell, J. (2001). Sea Level Change Through the Last Glacial Cycle. *Science*, 292(5517), 679–686.

Lambeck, K., Purcell, A., & Dutton, A. (2012). The anatomy of interglacial sea levels: The relationship between sea levels and ice volumes during the Last Interglacial. *Earth and Planetary Science Letters*, 315-316, 4–11.

Lambeck, K., Rouby, H., Purcell, A., Sun, Y., & Sambridge, M. (2014). Sea level and global ice volumes from the Last Glacial Maximum to the Holocene. *Proceedings of the National Academy of Sciences of the United States of America*, 111(43), 15296–303.

Lambeck, K., Smither, C., & Johnston, P. (1998). Sea-level change, glacial rebound and mantle viscosity fornorthern Europe. *Geophysical Journal International*, 134(1), 102–144.

Laske, G., Masters, G., Ma, Z., & Pasyanos, M. (2013). Update on CRUST1.0 -A 1-degree Global Model of Earth's Crust. In *Geophysical Research Abstracts EGU General Assembly*, volume 15 (pp. 2013–2658).

Latychev, K., Mitrovica, J. X., Tromp, J., Tamisiea, M. E., Komatitsch, D., & Christara, C.C. (2005). Glacial isostatic adjustment of 3-D Earth models: a finite-volume formulation. *Geophysical Journal International*, 161(2), 421-444.

Latychev, K., Mitrovica, J. X., Ishii, M., Chan, N.-H., & Davis, J. L. (2009). Body Tides on a 3-D Elastic Earth: Toward a Tidal Tomography. *Earth and Planetary Science Letters*, 277(1-2), 86–90.

Lau, H. C. P., Yang, H.-Y., Tromp, J., Mitrovica, J. X., Latychev, K., & Al-Attar, D. (2015). A normal mode treatment of semi-diurnal body tides on an aspherical, rotating and anelastic Earth. *Geophysical Journal International*, 202(2), 1392–1406.

Leclercq, P. W., Oerlemans, J., & Cogley, J. G. (2011). Estimating the Glacier Contribution to Sea-Level Rise for the Period 1800–2005. *Surveys in Geophysics*, 32(4-5), 519–535.

Lee, L. C., Morris, S. J. S., & Wilkening, J. (2011). Stress concentrations, diffusionally accommodated grain boundary sliding and the viscoelasticity of polycrystals. *Proceedings of the Royal Society A: Mathematical, Physical and Engineering Sciences*, 467(2130), 1624–1644.

Lekić, V., Cottaar, S., Dziewonski, A., & Romanowicz, B. (2012). Cluster analysis of global lower mantle tomography: A new class of structure and implications for chemical heterogeneity. *Earth and Planetary Science Letters*, 357, 68-77.

Lekić, V., Matas, J., Panning, M., & Romanowicz, B. (2009). Measurement and Implications of Frequency Dependence of Attenuation. *Earth and Planetary Science Letters*, 282(1-4), 285–293.

Lewis, S. E., Sloss, C. R., Murray-Wallace, C. V., Woodroffe, C. D., & Smithers, S. G. (2013). Post-glacial sea-level changes around the Australian margin: a review. *Quaternary Science Reviews*, 74, 115–138.

Liu, H.-P., Anderson, D. L., & Kanamori, H. (1976). Velocity dispersion due to anelasticity; implications for seismology and mantle composition. *Geophysical Journal International*, 47(1), 41–58.

Lognonné, P. (1991). Normal Modes and Seismograms in an Anelastic Rotating Earth. *Journal of Geophysical Research*, 96(B12), 20309.

Love, A. E. H. (1911). *Some Problems of Geodynamics*. Cambridge University Press.

Lyard, F., Lefevre, F., Letellier, T., & Francis, O. (2006). Modelling the global ocean tides: modern insights from FES2004. *Ocean Dynamics*, 56(5-6), 394–415.

Marquardt, H. & Miyagi, L. (2015). Slab stagnation in the shallow lower mantle linked to an increase in mantle viscosity. *Nature Geoscience*, 8(4), 311–314.

Marzeion, B., Jarosch, A. H., & Hofer, M. (2012). Past and future sea-level change from the surface mass balance of glaciers. *The Cryosphere*, 6(6), 1295–1322.

Marzeion, B., Leclercq, P. W., Cogley, J. G., & Jarosch, A. H. (2015). Brief Communication: Global reconstructions of glacier mass change during the 20th century are consistent. *The Cryosphere*, 9(6), 2399–2404.

Masters, G., Barmine, M., & Kientz, S. (2007). Mineos User's Manual. *Computational Infrastructure for Geodynamics, Califoria Institute of Technology, Pasadena.*

Masters, G., Laske, G., Bolton, H., & Dziewonski, A. M. (2000). The Relative Behavior of Shear Velocity, Bulk Sound Speed, and Compressional Velocity in the Mantle : Implications for Chemical and Thermal Structure. *Geophysical monograph*, 117, 63–87.

Mathews, P. M., Herring, T. A., & Buffett, B. A. (2002). Modeling of nutation and precession: New nutation series for nonrigid Earth and insights into the Earth's interior. *Journal of Geophysical Research*, 107(B4), 2068.

Matsumoto, K., Takanezawa, T., & Ooe, M. (2000). Ocean Tide Models Developed by Assimilating TOPEX/POSEIDON Altimeter Data into Hydrodynamical Model: A Global Model and a Regional Model around Japan. *Journal of Oceanography*, 56(5), 567–581.

McCarthy, C., Takei, Y., & Hiraga, T. (2011). Experimental study of attenuation and dispersion over a broad frequency range: 2. The universal scaling of polycrystalline materials. *Journal of Geophysical Research*, 116(B9), B09207.

McConnell, R. K. (1968). Viscosity of the mantle from relaxation time spectra of isostatic adjustment. *Journal of Geophysical Research*, 73(22), 7089–7105.

McNamara, A. K. & Zhong, S. (2005). Thermochemical structures beneath Africa and the Pacific Ocean. *Nature*, 437(7062), 1136–9.

Mégnin, C. & Romanowicz, B. (2000). The three-dimensional shear velocity structure of the mantle from the inversion of body, surface and higher-mode waveforms. *Geophysical Journal International*, 143(3), 709–728.

Métivier, L. & Conrad, C. P. (2008). Body Tides of a Convecting, Laterally Heterogeneous, and Aspherical Earth. *Journal of Geophysical Research*, 113(B11), B11405.

Mitrovica, J. & Forte, A. (2004). A new inference of mantle viscosity based upon joint inversion of convection and glacial isostatic adjustment data. *Earth and Planetary Science Letters*, 225(1-2), 177–189.

Mitrovica, J. X., Hay, C., Morrow, E., Kopp, R., Dumberry, M., & Stanley, S. (2015). Reconciling past changes in Earth's rotation with 20th century global sea-level rise: Resolving Munk's enigma. *Science advances*, 1(11), e1500679.

Mitrovica, J. X. (1996). Haskell [1935] revisited. *Journal of Geophysical Research*, 101(B1), 555.

Mitrovica, J. X., Davis, J. L., Mathews, P. M., & Shapiro, I. I. (1994). Determination of Tidal h Love Number Parameters in the Diurnal Band using an Extensive VLBI Dataset. *Geophysical Research Letters*, 21(8), 705–708.

Mitrovica, J. X. & Forte, A. M. (1997). Radial profile of mantle viscosity: Results from the joint inversion of convection and postglacial rebound observables. *Journal of Geophysical Research*, 102(B2), 2751.

Mitrovica, J. X., Forte, A. M., & Simons, M. (2000). A reappraisal of postglacial decay times from Richmond Gulf and James Bay, Canada. *Geophysical Journal International*, 142(3), 783–800.

Mitrovica, J. X. & Milne, G. A. (2003). On post-glacial sea level: I. General theory. *Geophysical Journal International*, 154(2), 253–267.

Mitrovica, J. X. & Peltier, W. R. (1989). Pleistocene deglaciation and the global gravity field. *Journal of Geophysical Research*, 94(B10), 13651.

Mitrovica, J. X. & Peltier, W. R. (1991). On postglacial geoid subsidence over the equatorial oceans. *Journal of Geophysical Research*, 96(B12), 20053.

Mitrovica, J. X. & Peltier, W. R. (1993a). Present-day secular variations in the zonal harmonics of Earth's geopotential. *Journal of Geophysical Research*, 98(B3), 4509.

Mitrovica, J. X. & Peltier, W. R. (1993b). The Inference of Mantle Viscosity From an Inversion of the Fennoscandian Relaxation Spectrum. *Geophysical Journal International*, 114(1), 45–62.

Mitrovica, J. X. & Peltier, W. R. (1995). Constraints on mantle viscosity based upon the inversion of post-glacial uplift data from the Hudson Bay region. *Geophysical Journal International*, 122(2), 353–377.

Mochizuki, E. (1986). The Free Oscillations of an Anisotropic and Heterogeneous Earth. *Geophysical Journal International*, 86(1), 167–176.

Morris, S. & Jackson, I. (2009). Diffusionally assisted grain-boundary sliding and viscoelasticity of polycrystals. *Journal of the Mechanics and Physics of Solids*, 57(4), 744–761.

Morrow, E., Mitrovica, J. X., Sterenborg, M. G., & Harig, C. (2013). A Test of Recent Inferences of Net Polar Ice Mass Balance based on Long-Wavelength Gravity. *Journal of Climate*, 26(17), 6535–6540.

Moulik, P. & Ekström, G. (2016). The relationships between large-scale variations in shear velocity, density, and compressional velocity in the Earth's mantle. *Journal of Geophysical Research: Solid Earth*, 121(4), 2737–2771.

Murakami, M., Hirose, K., Kawamura, K., Sata, N., & Ohishi, Y. (2004). Post-Perovskite Phase Transition in MgSiO3. *Science*, 304(5672), 855–858.

Nakada, M. & Karato, S.-i. (2012). Low viscosity of the bottom of the Earth's mantle inferred from the analysis of Chandler wobble and tidal deformation. *Physics of the Earth and Planetary Interiors*, 192-193, 68–80.

Nakada, M. & Lambeck, K. (1989). Late Pleistocene and Holocene sea-level change in the Australian region and mantle rheology. *Geophysical Journal International*, 96(3), 497–517.

Nakada, M., Okuno, J., Lambeck, K., & Purcell, A. (2015a). Viscosity structure of Earth's mantle inferred from rotational variations due to GIA process and recent melting events. *Geophysical Journal International*, 202(2), 976–992.

Nakada, M., Okuno, J., & Yokoyama, Y. (2015b). Total meltwater volume since the Last Glacial Maximum and viscosity structure of Earth's mantle inferred from relative sea level changes at Barbados and Bonaparte Gulf and GIA-induced $\dot{J}_2$. *Geophysical Journal International*, 204(2), 1237–1253.

Nakagawa, T. & Tackley, P. J. (2004). Effects of thermo-chemical mantle convection on the thermal evolution of the Earth's core. *Earth and Planetary Science Letters*, 220(1-2), 107–119.

Nerem, R. & Wahr, J. (2011). Recent changes in the earth's oblateness driven by greenland and antarctic ice mass loss. *Geophysical Research Letters*, 38.

Ni, S., Tan, E., Gurnis, M., & Helmberger, D. (2002). Sharp Sides to the African Superplume. *Science*, 296(5574), 1850–2.

Nordman, M., Milne, G., & Tarasov, L. (2015). Reappraisal of the Angerman River decay time estimate and its application to determine uncertainty in Earth viscosity structure. *Geophysical Journal International*, 201(2), 811–822.

Nowick, A. & Berry, B. (1972). *Anelastic Relaxation in Crystalline Materials*. New York: Academic.

O'Connell, R. J. (1971). Pleistocene Glaciation and the Viscosity of the Lower Mantle. *Geophysical Journal International*, 23(3), 299–327.

O'Connell, R. J. & Budiansky, B. (1978). Measures of dissipation in viscoelastic media. *Geophysical Research Letters*, 5(1), 5–8.

Park, J. & Gilbert, F. (1986). Coupled Free Oscillations of an Aspherical, Dissipative, Rotating Earth: Galerkin Theory. *Journal of Geophysical Research*, 91(B7), 7241.

Parsons, B. (1972). *Changes in the Earth's shape*. PhD thesis, University of Cambridge.

Peltier, W. (2004). Global glacial isostasy and the surface of the ice-age Earth: The ICE-5G (VM2) model and GRACE. *Annual Review of Earth and Planetary Sciences*, 32(1), 111–149.

Peltier, W. R. (1974). The impulse response of a Maxwell Earth. *Reviews of Geophysics*, 12(4), 649.

Peltier, W. R. (1976). Glacial-Isostatic Adjustment-II. The Inverse Problem. *Geophysical Journal of the Royal Astronomical Society*, 46(3), 669–705.

Peltier, W. R. (1985). The LAGEOS constraint on deep mantle viscosity: Results from a new normal mode method for the inversion of viscoelastic relaxation spectra. *Journal of Geophysical Research*, 90(B11), 9411.

Peltier, W. R. (1988). Global sea level and Earth rotation. *Science (New York, N.Y.)*, 240(4854), 895–901.

Peltier, W. R. (1998a). The inverse problem for mantle viscosity. *Inverse Problems*, 14(3), 441–478.

Peltier, W. R. (1998b). A space geodetic target for mantle viscosity discrimination: Horizontal motions induced by glacial isostatic adjustment. *Geophysical Research Letters*, 25(4), 543–546.

Peltier, W. R., Argus, D. F., & Drummond, R. (2015). Space geodesy constrains ice age terminal deglaciation: The global ICE-6G_C (VM5a) model. *Journal of Geophysical Research: Solid Earth*, 120(1), 450–487.

Peltier, W. R., Drummond, R. A., & Tushingham, A. M. (1986). Post-glacial rebound and transient lower mantle rheology. *Geophysical Journal International*, 87(1), 79–116.

Pendea, I. F., Costopoulos, A., Nielsen, C., & Chmura, G. L. (2010). A new shoreline displacement model for the last 7 ka from eastern James Bay, Canada. *Quaternary Research*, 73(3), 474–484.

Petit, G. & Luzum, B. (eds). (2010). *IERS Conventions*. International Earth Rotation and Reference Service (IERS) Technical Note No. 36.

Qin, C., Zhong, S., & Wahr, J. (2014). A Perturbation Method and its Application: Elastic Tidal Response of a Laterally Heterogeneous Planet. *Geophysical Journal International*, 199(2), 631–647.

Raj, R. (1975). Transient behavior of diffusion-induced creep and creep rupture. *Metallurgical Transactions A*, 6(8), 1499–1509.

Raj, R. & Ashby, M. F. (1971). On grain boundary sliding and diffusional creep. *Metallurgical Transactions*, 2(4), 1113–1127.

Ray, R. D., Eanes, R. J., & Lemoine, F. G. (2001). Constraints on energy dissipation in the Earth's body tide from satellite tracking and altimetry. *Geophysical Journal International*, 144(2), 471–480.

Resovsky, J., Trampert, J., & Van der Hilst, R. (2005). Error bars for the global seismic Q profile. *Earth and Planetary Science Letters*, 230(3-4), 413–423.

Resovsky, J. S. & Ritzwoller, M. H. (1995). Constraining Odd-Degree Earth Structure with Coupled Free-Oscillations. *Geophysical Research Letters*, 22(16), 2301–2304.

Ricard, Y., Fleitout, L., & Froidevaux, C. (1984). Geoid heights and lithospheric stresses for a dynamic earth. *Annales Geophysicae (ISSN 0755-0685)*, 2, 267–285.

Richards, M. A. & Hager, B. H. (1984). Geoid anomalies in a dynamic Earth. *Journal of Geophysical Research*, 89(B7), 5987.

Ritsema, J., Deuss, A., van Heijst, H. J., & Woodhouse, J. H. (2011). S40RTS: A Degree-40 Shear-Velocity Model for the Mantle from new Rayleigh Wave Dispersion, Teleseismic Traveltime and Normal-Mode Splitting Function Measurements. *Geophysical Journal International*, 184(3), 1223–1236.

Ritsema, J., van Heijst, H. J., & Woodhouse, J. H. (1999). Complex Shear Wave Velocity Structure Imaged Beneath Africa and Iceland. *Science*, 286(5446), 1925–1928.

Rivière, A. (2001). 3.5 High Temperature Damping. *Materials Science Forum*, 366-368, 268–275.

Roy, K. & Peltier, W. (2011). Grace era secular trends in earth rotation parameters: A global scale impact of the global warming process? *Geophysical Research Letters*, 38.

Rubincam, D. P. (1984). Postglacial rebound observed by lageos and the effective viscosity of the lower mantle. *Journal of Geophysical Research*, 89(B2), 1077.

Rudolph, M. L., Lekić, V., & Lithgow-Bertelloni, C. (2015). Viscosity jump in Earth's mid-mantle. *Science (New York, N.Y.)*, 350(6266), 1349–52.

Sabadini, R., Yuen, D. A., & Gasperini, P. (1985). The effects of transient rheology on the interpretation of lower mantle viscosity. *Geophysical Research Letters*, 12(6), 361–364.

Sabadini, R., Yuen, D. A., & Gasperini, P. (1988). Mantle rheology and satellite signatures from present-day glacial forcings. *Journal of Geophysical Research*, 93(B1), 437.

Sailor, R. V. & Dziewonski, A. M. (1978). Measurements and Interpretation of Normal-Mode Attenuation. *Geophysical Journal International*, 53(3), 559–581.

Sauramo, M. (1958). *Die geschichte der Ostsee*. Helsinki: Acta Geogr.

Savcenko, R. & Bosch, W. (2012). *EOT11a -empirical ocean tide model from multi-mission satellite altimetry*. Technical report, DGFI.

Shida, T. (1912). *On the Elasticity of the Earth and the Earth's Crust*. Kyoto Imperial University.

Shito, A., Karato, S.-i., & Park, J. (2004). Frequency dependence of Q in Earth's upper mantle inferred from continuous spectra of body waves. *Geophysical Research Letters*, 31(12), n/a–n/a.

Simmons, N. A., Forte, A. M., Boschi, L., & Grand, S. P. (2010). GyPSuM: A joint tomographic model of mantle density and seismic wave speeds. *Journal of Geophysical Research*, 115(B12), B12310.

Sipkin, S. A. & Jordan, T. H. (1979). Frequency Dependence of Q_{ScS}. *Bulletin of the Seismological Society of America*, 69(4), 1055–1079.

Sloss, C. R., Murray-Wallace, C. V., & Jones, B. G. (2007). Holocene sea-level change on the south-east coast of Australia: a review. *The Holocene*, 17(7), 999–1014.

Smith, M. L. & Dahlen, F. A. (1981). The Period and Q of the Chandler Wobble. *Geophysical Journal International*, 64(1), 223–281.

Su, W. & Dziewonski, A. M. (1997). Simultaneous Inversion for 3-D Variations in Shear and Bulk Velocity in the Mantle. *Physics of the Earth and Planetary Interiors*, 100(1-4), 135–156.

Sun, D., Tan, E., Helmberger, D., & Gurnis, M. (2007). Seismological support for the metastable superplume model, sharp features, and phase changes within the lower mantle. *Proceedings of the National Academy of Sciences of the United States of America*, 104(22), 9151–5.

Tackley, P. J. (1998). Three-dimensional simulations of mantle convection with a thermo-chemical basal boundary layer: D"? In B. B. M. Gurnis, M.E. Wysession, E. Knittle (Ed.), *The Core-Mantle Boundary Region* (pp. 231–253). Washington, D.C.: American Geophysical Union.

Tackley, P. J. (2002). Strong Heterogeneity caused by Deep Mantle Layering. *Geochemistry Geophysics Geosystems*, 3(4), 1024.

Taguchi, E., D. S. & Zahel, W. (2010). Estimation of deep ocean tidal energy dissipation based on the high-resolution data-assimilative HAMTIDE model. *Journal of Geophysical Research*.

Takei, Y. & Holtzman, B. K. (2009). Viscous constitutive relations of solid-liquid composites in terms of grain boundary contiguity: 2. Compositional model for small melt fractions. *Journal of Geophysical Research*, 114(B6), B06206.

Takeuchi, H. (1950). On the Earth tide of the compressible Earth of variable density and elasticity. *Transactions, American Geophysical Union*, 31(5), 651.

Tarantola, A. & Valette, B. (1982). Generalized nonlinear inverse problems solved using the least squares criterion. *Reviews of Geophysics*, 20(2), 219.

Thomson, W. (1863). On the Rigidity of the Earth. *Philosophical Transactions of the Royal Society of London*, 153, 573–582.

Torsvik, T. H., Smethurst, M. A., Burke, K., & Steinberger, B. (2006). Large igneous provinces generated from the margins of the large low-velocity provinces in the deep mantle. *Geophysical Journal International*, 167(3), 1447–1460.

Trampert, J., Deschamps, F., Resovsky, J., & Yuen, D. (2004). Probabilistic Tomography Maps Chemical Heterogeneities Throughout the Lower Mantle. *Science (New York, N.Y.)*, 306(5697), 853–6.

Tromp, J. & Dahlen, F. A. (1990). Summation of the Born Series for the Normal Modes of the Earth. *Geophysical Journal International*, 100(3), 527–533.

Tromp, J. & Mitrovica, J. X. (1999). Surface loading of a viscoelastic earth–I. General theory. *Geophysical Journal International*, 137(3), 847–855.

Tushingham, A. M. & Peltier, W. R. (1992). Validation of the ICE-3G Model of Würm-Wisconsin Deglaciation using a global data base of relative sea level histories. *Journal of Geophysical Research*, 97(B3), 3285.

van der Hilst, R., Engdahl, R., Spakman, W., & Nolet, G. (1991). Tomographic Imaging of Subducted Lithosphere below Northwest Pacific Island Arcs. *Nature*, 353(6339), 37–43.

Vaughan, D., Comiso, J., Allison, I., Carrasco, J., Kaser, G., Kwok, R., Mote, P., Murray, T., Paul, F., Ren, J., Rignot, E., Solomina, O., Steffen, K., & Zhang, T. (2013). Observations: Cryosphere. In T. Stocker, D. Qin, G.-K. Plattner, M. Tignor, S. Allen, J. Boschung, A. Nauels, Y. Xia, V. Bex, & P. Midgley (Eds.), *Climate Change 2013: The Physical Science Basis. Contribution of Working Group I to the Fifth Assessment Report of the Intergovernmental Panel on Climate Change* book section 4, (pp. 317–382). Cambridge, United Kingdom and New York, NY, USA: Cambridge University Press.

Vermeersen, L. L. A., Sabadini, R., Devoti, R., Luceri, V., Rutigliano, P., Sciarretta, C., & Bianco, G. (1998). Mantle viscosity inferences from joint inversions of pleistocene deglaciatio-induced changes in geopotential with a new SLR analysis and polar wander. *Geophysical Research Letters*, 25(23), 4261–4264.

Wahr, J. & Bergen, Z. (1986). The Effects of Mantle Anelasticity on Nutations, Earth Tides, and Tidal Variations in Rotation Rate. *Geophysical Journal International*, 87(2), 633–668.

Wahr, J. M. (1981a). A Normal Mode Expansion for the Forced Response of a Rotating Earth. *Geophysical Journal of the Royal Astronomical Society*, 64(3), 651–675.

Wahr, J. M. (1981b). Body Tides on an Elliptical, Rotating, Elastic and Oceanless Earth. *Geophysical Journal of the Royal Astronomical Society*, 64(3), 677–703.

Walcott, R. (1972). Late quaternary vertical movements in eastern north america: Quantitative evidence of glacio-isostatic rebound. *Reviews of Geophysics*, 10, 849–884.

Wang, R. (1994). Effect of Rotation and Ellipticity On Earth Tides. *Geophysical Journal International*, 117(2), 562–565.

Wieczerkowski, K., Mitrovica, J. X., & Wolf, D. (1999). A revised relaxation-time spectrum for Fennoscandia. *Geophysical Journal International*, 139(1), 69–86.

Woodhouse, J. (1988). The calculation of eigenfrequencies and eigenfunctions of the free oscillations of the earth and the sun. *Seismological Algorithms*, (pp. 321–370).

Woodhouse, J. H. (1980). The Coupling and Attenuation of Nearly Resonant Multiplets in the Earth's Free Oscillation Spectrum. *Geophysical Journal International*, 61(2), 261–283.

Woodhouse, J. H. & Dahlen, F. A. (1978). The Effect of a General Aspherical Perturbation on the Free Oscillations of the Earth. *Geophysical Journal International*, 53(2), 335–354.

Wookey, J., Stackhouse, S., Kendall, J.-M., Brodholt, J., & Price, G. D. (2005). Efficacy of the post-perovskite phase as an explanation for lowermost-mantle seismic properties. *Nature*, 438(7070), 1004–7.

Wu, P. (1978). The response of a maxwell earth to applied surface mass loads: Glacial isostatic adjustment. Master's thesis, University of Toronto.

Wu, P. & Peltier, W. (1983). Glacial isostatic adjustment and the free air gravity anomaly as a constraint on deep mantle viscosity. *Geophysical Journal of the Royal Astronomical Society*, 74, 377–449.

Wu, P. & Peltier, W. R. (1984). Pleistocene deglaciation and the Earth's rotation: a new analysis. *Geophysical Journal International*, 76(3), 753–791.

Yang, H.-Y. & Tromp, J. (2015). Synthetic free-oscillation spectra: an appraisal of various mode-coupling methods. *Geophysical Journal International*, 203(2), 1179–1192.

Yoder, C. F., Williams, J. G., Dickey, J. O., Schutz, B. E., Eanes, R. J., & Tapley, B. D. (1983). Secular variation of Earth's gravitational harmonic J2 coefficient from Lageos and nontidal acceleration of Earth rotation. *Nature*, 303(5920), 757–762.

Yuan, L. & Chao, B. F. (2012). Analysis of Tidal Signals in Surface Displacement Measured by a Dense Continuous GPS Array. *Earth and Planetary Science Letters*, 355-356, 255–261.

Yuan, L., Chao, B. F., Ding, X., & Zhong, P. (2013). The Tidal Displacement Field at Earth's Surface Determined using Global GPS Observations. *Journal of Geophysical Research: Solid Earth*, 118(5), 2618–2632.

Yuen, D. A. & Peltier, W. R. (1982). Normal modes of the viscoelastic earth. *Geophysical Journal International*, 69(2), 495–526.

Yuen, D. A. & Sabadini, R. (1985). Viscosity stratification of the lower mantle as inferred by the J2 observation. *Annales geophysicae*, 3(5), 647–654.

Zener, C. (1948). *Elasticity and Anelasticity of Metals*. University of Chicago Press.

Zhao, D. (2004). Global Tomographic Images of Mantle Plumes and Subducting Slabs: Insight into Deep Earth Dynamics. *Physics of the Earth and Planetary Interiors*, 146(1-2), 3–34.

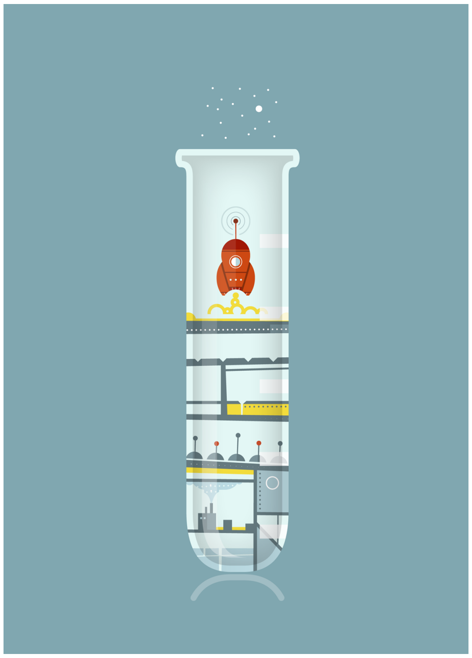

THIS THESIS WAS TYPESET using LaTeX, originally developed by Leslie Lamport and based on Donald Knuth's TeX. The body text is set in 11 point Egenolff-Berner Garamond, a revival of Claude Garamont's humanist typeface. The above illustration, *Science Experiment 02*, was created by Ben Schlitter and released under CC BY-NC-ND 3.0. A template that can be used to format a PhD dissertation with this look & feel has been released under the permissive AGPL license, and can be found online at github.com/suchow/Dissertate or from its lead author, Jordan Suchow, at suchow@post.harvard.edu.